THEORETICAL INVESTIGATIONS ON NANOPOROUS MATERIALS AND

IONIC LIQUIDS FOR ENERGY STORAGE

A Dissertation

by

MOUSUMI MANI BISWAS

Submitted to the Office of Graduate Studies of
Texas A&M University
in partial fulfillment of the requirements for the degree of

DOCTOR OF PHILOSOPHY

December 2011

Major Subject: Materials Science and Engineering

THEORETICAL INVESTIGATIONS ON NANOPOROUS MATERIALS AND

IONIC LIQUIDS FOR ENERGY STORAGE

A Dissertation

by

MOUSUMI MANI BISWAS

Submitted to the Office of Graduate Studies of
Texas A&M University
in partial fulfillment of the requirements for the degree of

DOCTOR OF PHILOSOPHY

Approved by:

Chair of Committee,	Tahir Cagin
Committee Members,	Mahboobul Mannan
	Miladin Radovic
	Hong-Cai Zhou
Intercollegiate Faculty Chair,	Ibrahim Karaman

December 2011

Major Subject: Materials Science and Engineering

ABSTRACT

Theoretical Investigations on Nanoporpus Materials and Ionic Liquids for Energy Storage.

(December 2011)

Mousumi Mani Biswas, B.Tech., Indian Institute of Technology;

M.S., University of Windsor

Chair of Advisory Committee: Dr. Tahir Cagin

In the current context of rapidly depleting petroleum resources and growing environmental concerns, it is important to develop materials to harvest and store energy from renewable and sustainable sources. Hydrogen has the potential to be an alternative energy source, since it has higher energy content than petroleum. However, since hydrogen has very low volumetric energy density, hence it is important to design nano porous materials which can efficiently store large volumes of hydrogen gas by adsorption. In this regard carbon nanotube and Metal Organic Framework (MOFs) based materials are worth studying.

Ionic liquids (IL) are potential electrolytes that can improve energy storage capacity and safety in Li ion batteries. Therefore it is important to understand IL's thermodynamic and transport properties, especially when it is in contact with electrode surface and mixed with Li salt, as happens in the battery application.

This dissertation presents computation and simulation based studies on:

1. Hydrogen storage in carbon nanotube scaffold.

2. Mechanical property and stability of various nanoporous Metal Organic Frameworks.

3. Thermodynamic and transport properties of [BMIM][BF4] ionic liquid in bulk , in Li Salt mixture, on graphite surface and under nanoconfinement.

In the first study, we report the effects of carbon nanotube diameter, tube chirality, tube spacer distance, tube functionalization and presence of Li on hydrogen sorption capacity and thermodynamics at different temperature and pressure. In the second one, we observe high pressure induced structural transformation of 6 isoreticular MOFs: IRMOF-1. IRMOF-3, IRMOF-6, IRMOF-8, IRMOF-10 and IRMOF-14, explore the deformation mechanism and effect of Hydrogen inside crystal lattice. In the third study, we observe the equilibrium thermodynamic and transport properties of [BMIM][BF4] ionic liquid. The temperature dependence of ion diffusion, conductivity, dielectric constant, dipole relaxation time and viscosity have been observed and found similar behavior to those of supercooled liquid. The ion diffusion on graphite surfaces and under nanoconfinement was found to be higher compared to those in bulk.

ACKNOWLEDGEMENTS

TABLE OF CONTENTS

LIST OF FIGURES

FIGURE   Page

LIST OF TABLES

CHAPTER I

INTRODUCTION

1.1   Motivation

Energy and environment is of great concern in today's world. In the current context of dwindling petroleum resources and growing environmental concern, our society is trying to move towards more sustainable and renewable energy sources like solar, wind, etc.[1] However, we are still greatly dependent on petroleum as our energy source, especially in the transportation sector, which is the biggest consumer of petroleum. It is difficult to replace petroleum with an alternative fuel that can provide similar ease and efficiency as petroleum.

Innovating mechanisms to generate energy from renewable sources is important, but storage and distribution of this generated energy to locations where it will be consumed, is another great challenge.[2,3] Supply of solar and wind energy depends on favorable natural conditions and geographic locations. On the other hand we need constant energy supply at any location of our choice. Therefore, we need a medium to store and distribute energy. We have this problem because, today, we do not have efficient technologies to achieve this. Thus in order to reduce our dependency on petroleum, we need to solve this problem.

Hydrogen is considered as a possible alternative of petroleum, especially for the transportation sector. This is because it has higher gravimetric energy content, which is almost 3 times that of petroleum and other fossil fuels (142 MJ/kg for H_2 vs. 47 MJ/kg for petroleum).[4,5] Hydrogen can

_____

This dissertation follows the style of *Journal of Physical Chemistry B.*

be generated by water electrolysis using electricity obtained from other renewable resources like solar, wind etc. Once generated this gas can be then stored and transported to the locations where energy is needed. Hydrogen can be either combusted or used in fuel cells instead of fossil fuels, to generate electricity. Water, the only byproduct from these oxidation processes, can be safely released to the environment as water vapor or even recycled back to generate hydrogen gas. Thus, when used in this manner, hydrogen has the potential to replace petroleum with least environmental impact. But the currently available hydrogen storage technologies and materials are not equipped to provide similar energy output as petroleum in a sustainable way. We need to develop new materials and technologies to exploit hydrogen as an effective source of energy. In this regard nanotechnology is expected to play a significant role in developing new materials and technologies for sustainable energy generation and storage.

For transportation applications in new generation electric vehicles, the other kind of energy storage solution is Lithium ion batteries. In this scheme, electricity is distributed through the electric transmission grid to charge Li-ion batteries in electric cars. Once fully charged, these batteries store enough energy to run the vehicle for a few hundred miles or less before the next charge cycle. However the limited energy storage capacity restricts the range of vehicle compared to what a tank full of gas can provide. So a lot of research is being undertaken to improve the battery chemistries to increase battery energy storage capacity, decrease charging time, increase peak current delivery rate, battery longevity, safety and environmental friendliness. Here nanotechnology can also play a major role to develop new materials for superior battery chemistries and performance.

1.2   The hydrogen storage problem and hydrogen storage materials

The major challenge in using hydrogen is its low volumetric energy content. To obtain similar energy output as petroleum we need to have around 1300 times the volume of petroleum.[4,5] Therefore, to achieve similar volumetric energy content as petroleum, hydrogen has to be liquefied or compressed for its transportation, storage and. The major hurdle in this process is the energy consuming compression and liquefaction steps where around 30 % of the stored energy is consumed and thus lost. Thus even if renewable electricity is used for water electrolysis and generation of hydrogen, the overall output will be less in hydrogen powered vehicle compared to electric vehicle.[6]

A more energy efficient hydrogen storage alternative is to use suitable hydrogen adsorbing porous materials which can reversibly adsorb hydrogen gas and release under suitable conditions. Various materials like metal hydrides, carbon nanotube, graphene, porous metal organic frameworks, zeolites, coordination polymers, etc. are being explored as potential storage materials. These materials, having large surface areas, readily adsorb hydrogen under lower pressure and thus do not need much energy unlike that required in the hydrogen compression and liquefaction steps. Hydrogen storage by metal hydrides can achieve high volumetric density but it poses problems, like slower kinetics, high temperature, low gravimetric capacity, thermal management, etc. On the other hand, adsorption based by carbon nanotube, graphitic materials, metal organic frameworks, covalent organic frameworks, aerogels are promising hydrogen gas storage materials for several reasons: 1) large storage potential due to large surface area; 2) fast adsorption and desorption kinetics due to low binding energy; 3) low temperature operation and thus require simpler thermal management techniques; and 4) light weight. Out of all these, carbon nano structured materials (mainly carbon nanotube, fullerene, graphene) and metal

organic frameworks are gaining lot of attentions recently as these nanoporous materials have demonstrated high storage potential approaching Department of Energy (DOE) target. DOE requires that by 2015, the storage material should be able to store hydrogen gas which is 9% of its weight.[5]

1.3   Approaches to increase adsorption capacity of carbon nanotubes

Carbon nano structures such as single and multiwall carbon nanotubes (SWNT, MWNT), fullerene, graphene, etc. are promising hydrogen storage materials.[7-14] Carbon nanotubes (CNT) are particularly attractive because, in addition to the structural properties such as porosity and large surface area which results in high adsorption capacity, the curved surface and capillary effect further increase the H_2 storage capacity.[15] However, the adsorption on "plain" carbon nanotubes does not reach the necessary storage capacity as targeted by US DOE.[5] Fortunately, there are several avenues which may be investigated to improve the adsorption capacity of CNT structures.

A key approach to improve the adsorption capacity of CNTs is to increase their effective adsorption surface area. After production, carbon nanotubes usually remain in the form of bundles or ropes made up of several individual nanotubes which are attached to each other by cohesive force.[16-19] As a result, most of the nanotube surfaces remain inaccessible for H_2 molecules. This in turn results lower H_2 adsorption capacity. If the outer surface areas of all the tubes in the bundles could be exposed to H_2 molecules, then that alone would have improved the adsorption capacity of carbon nanotubes. Various researchers have pointed out this problem and suggested that the inter-tube distance (or the van der Waals gap), should be increased to enhance accessible surface.[18-21]

One way to expose the outer surface areas of carbon nanotubes (CNT) is to insert spacers between the individual tubes, so that the tubes, instead of forming cohesive bundles, forms scaffolding structures as suggested in Fig. 1.1. Covalent functionalization using different cross-linking agents[17, 21, 22] may be used as spacers to develop such carbon nano tube scaffolds. These scaffolding structures with their exposed outer tube surface can have higher H_2 adsorption capacity. In fact, Prof. J. Tour's group of Rice University[17] found that the H_2 sorption capacity of a crosslinked single walled carbon nanotube scaffold is almost twice of that of other carbon materials like activated carbon, etc. This is a new approach and not many systematic studies are available to indicate how the sorption capacity depends on the choice of tube diameter, crosslinker (spacer) frequency and covalent functionalization of tube surface.

In addition, the carbon nanotubes produced by most production techniques are capped at both ends by fullerene like structures. Removal of these end caps by special treatment will further increase adsorption surface area.[19, 23]
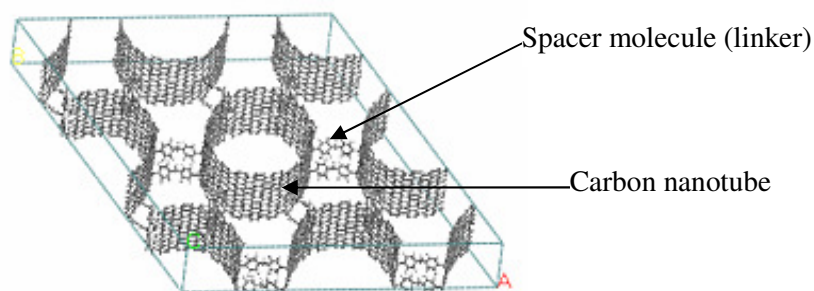
Fig. 1.1 Carbon nanotube scaffold

Several studies have shown that incorporation of certain metals like Li, K, and Ti in the tube walls improved the adsoprtion capacity of plain carbon nanotubes.[24-26] Thus, we expect that a similar approach might also improve the adsorption capacities of the scaffolded CNT structures.

However, we need to confirm the impact of these possible approaches. Therefore we propose to investigate the efficacies of all these above mentioned approaches in improving adsorption capacity.

1.4   MOF as alternative adsorption materials

Metal organic frameworks (MOF) are also considered as alternative hydrogen storage materials. These are highly porous crystalline materials made up of metal oxide clusters positioned at the vertices and connected by organic linkers (Fig. 1.2). MOFs have very low density and large surface area and thus have potential application in gas storage, gas separation, catalysis, molecular recognition, drug delivery, etc.[27-31]
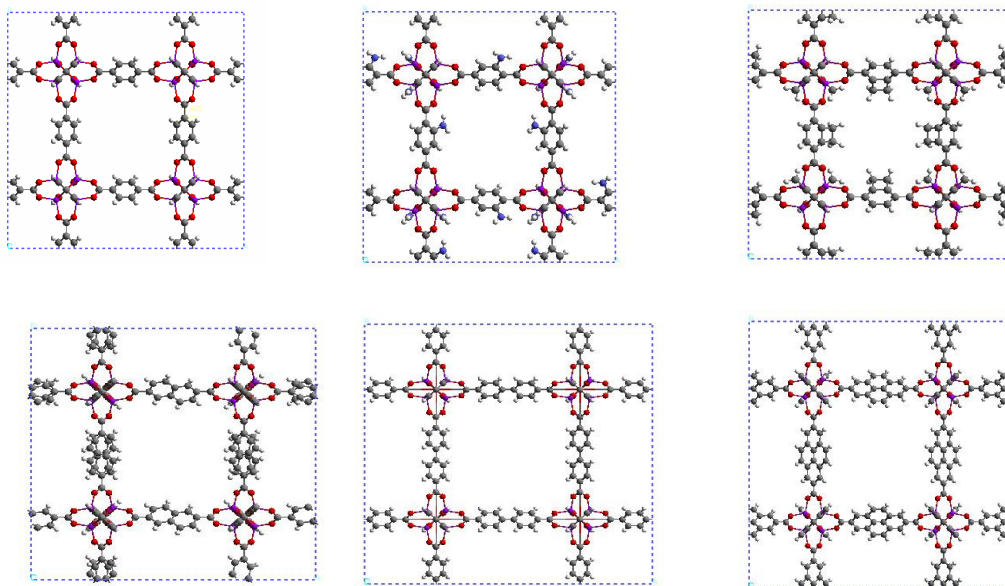
Fig. 1.2 Crystal structures of IRMOF- 1, 3, 6, 8, 10 and 14

In gas storage applications, the storage material may be subjected to high pressure. Therefore it is important that the MOF used should have suitable mechanical properties and stability. In this

regard, an important behavior of the MOFs is their structural flexibility. In the presence of external stimuli like temperature, pressure or adsorbed (guest) molecules, some MOFs can undergo large and mostly reversible change in crystal lattice structure, which involves atomic displacements in the order of several angstroms.[31] This 'single-crystal-to-single-crystal transformations' may be caused by: exchange of guest molecules ('breathing effect'); hydration; or by change of temperature.[32-34] Pressure is another important external stimulus that can cause such crystal deformation. Effect of pressure on MOFs is especially interesting because in some applications such as gas storage and separation, MOFs may encounter high pressures. Here high pressure may lead to change in porosity of the MOF based membrane; it's mechanical stability and thus changes in selectivity, permeation of the guest molecule.[35, 36] Therefore, we need to understand the mechanical stability and structural behavior of MOFs under high pressure.

A lot of studies have been conducted on the effect of pressure and temperature on gas adsorption in porous crystalline structures of MOF, but only a few studies[37-41] are available on the mechanical property and structural stability of MOF-5 structure. The only two studies on structural behavior under high pressure, which we could identify, are on a Cu based MOF and a Zinc imidazole framework.[35, 36] High pressure experiments on the Cu based MOF indicated that the Cu-MOF crystal collapses suddenly to a different crystal structure, after a threshold pressure. Similar study on a Zinc imidazole framework revealed the pressure induced structural transformation by cooperative bond rearrangements. Though, there are numerous studies on pressure induced transformations in the other industrially important porous structures, zeolites,[42] but there is dearth of knowledge on the mechanical behavior of MOF-5 and other MOFs, under high external pressure. This is probably due to the difficulty in conducting experimental studies under high pressure. In this situation, a simulation based theoretical study can be very useful to

gain some insight on MOF's mechanical behavior under high pressure. In this dissertation, we present results of our theoretical investigations on the mechanical properties of some of the designed MOFs, so that these may aid their application as hydrogen storage materials.

1.5   Potentials of ionic liquids in Li-ion rechargeable batteries

Amongst other the energy storage devices, Lithium–ion rechargeable battery is a major success.[3] A Li ion battery consists of a lithium–ion intercalation negative electrode (usually graphite), a lithium–ion intercalation positive electrode (usually lithium metal oxide) and an organic electrolyte (usually $LiPF_6$ salt in ethylene and dielthylene carbonate). However the current Li ion battery technology has reached the limit of its performance in terms of energy storage density (i.e. energy storage per unit physical volume), peak current discharge rate, charging time, battery longevity, etc. New generation of rechargeable lithium batteries with improved performance are needed for hybrid electric vehicles, clean energy storage and in consumer electronics. To come up with such batteries, further breakthrough in battery materials and electrolytes are required. In this regard, 'Ionic liquids' are considered as promising battery electrolytes.

Ionic Liquids (IL) are entirely composed of ions and are liquid below 100 ^{0}C. They have negligible vapor pressure, high electrochemical window, good electrical conductivity and they are non flammable. These are considered as a new class of 'designer' solvents with many interesting properties such as: 1) nonvolatility; 2) good solvation and coordination property; 3) immiscibility with water and low hydroscopicity; 4) nonflamability, etc.[43] Therefore, they are finding application in catalysis, batteries, fuel cells and solar photo-voltaics, in addition to being considered as Li-ion battery electrolytes.

In Li-ion batteries, ionic liquid electrolytes may have another major role to play. When used, they seem to prevent solvent co-intercalation thereby preventing graphite exfoliation.[43] Conventional organic electrolytes that are being used today in Li-ion batteries are quite volatile. In presence of graphite exfoliation and heat release during normal battery operational cycles, the flammable vapors released by these carbon based organic electrolytes can cause fire hazards. On the other hand, the non-flamability property of ionic liquids make them suitable candidates for use in such conditions as an alternative to existing electrolytes. Ionic liquid electrolytes are also found to be stable with very high capacity electrodes and have shown dramatic increase in battery energy density. In addition, these are also environmental friendly 'green' materials. Therefore, ionic liquids are good contenders for future Li-ion battery.[43]

However, research on ionic liquids is a nascent area and there are several unanswered questions like:

- How ionic liquid behave on electrode surface and under nano-confinement ?
- What are their transport and thermodynamic properties in bulk and also in the presence of a surface ?
- How these properties and behavior change in presence of Li salt ?

To answer some these questions, this dissertation presents studies on [BMIM][BF4] ionic liquid (molecular structure is presented in Fig. 1.3).
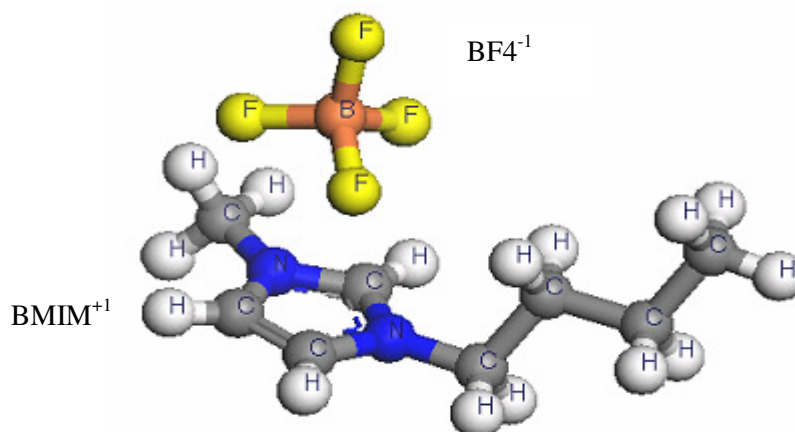
Fig. 1.3 Molecular structure of BMIM^{+1} and BF4^{-1}

As graphite is used as a negative electrode in Li ion battery, so we study the effects of graphite surface and nanoconfinement on this ionic liquid. Li ion batteries often use Li salts like LiBF4, LiPF6 in the electrolyte in order to get improved battery performance, improved electrochemical stability, current collector passivation, Solid-Electrolyte-Interface (SEI) stabilization, low temperature operation, etc. Therefore we also study how this ionic liquid behaves when mixed with Li salt.

1.6   Research objectives

Experimental methods may not always be adequate to study materials behavior in the nanoscale and in those situations, theoretical investigations using various theories and computational tools may give us valuable insights about materials property. Thus this dissertation studies properties of selected materials for application in energy industry, using theoretical calculations and atomistic simulations. The objectives of the research presented in this dissertation are as follows:

1) To study hydrogen storage behavior in nanoporous carbon naotube scaffold.

    a.   Characterize the effects of tube diameter, cross linking frequency, tube chirality, and surface functionality and presence of Li on hydrogen sorption behavior.

    b.   Study the thermodynamics of the process.

2) To investigate behavior of few metal organic frameworks (IRMOF-1, IRMOF-3, IRMOF-6, IRMOF-8, IRMOF-10 and IRMOF-14) under high pressure, such as:

    a.   Reversibility of the process, effect of different linkers.

    b.   Effect of presence of hydrogen in side the pore deformation process.

3) To investigate behavior of imidazole based ionic liquid ([BMIM][BF4]) in pure bulk condition, specifically study the:

    a.   Thermodynamic, and transport property.

    b.   Behavior on graphite surface and interface.

    c.   Properties of [BMIM][BF4] ionic liquid in LiBF4 salt mixture.

1.7   Dissertation organization

The dissertation is organized as follows:

Chapter II analyses the existing state of art in hydrogen storage materials and ionic liquid behavior and the relevant theories. Chapter III discusses the theoretical methods used to investigate the materials property in this dissertation. Chapter IV presents the results from hydrogen storage study on carbon nanotube scaffold and Chapter V contains results from high pressure study on metal organic framework materials. Chapter VI describes the results of the studies on Ionic liquid. Finally, Chapter VII concludes this dissertation by identifying the contributions of this work and future directions.

CHAPTER II

CURRENT STATE OF RESEARCH

This chapter presents current state of research on nanoporous materials for hydrogen storage, ionic liquid for Li ion battery application and other relevant theories. The characteristics and properties of the carbon nano-structures, metal organic frameworks that have been used in the study are also described here. This is followed by a discussion on the theories on adsorption process and identification of factors that affect hydrogen adsorption in these nano porous materials. Next the structure and behavior of the ionic liquid are described. Finally, the theories and computational techniques that are relevant for the simulation based studies are described.

2.1   Nanoporous materials

Nanoporous or microporous materials like metal organic frameworks (MOF) and carbon nano structures have pore width below ~20 Å. These materials can have very orderly and well defined pores like in zeolites, MOFs, SWNT, or have disordered pores as in activated carbons.[44] Structural features of nanoporous carbon materials and metal organic frameworks are briefly described below.

2.1.1   Carbon nano structures

Activated carbon had been used for a long time as an effective adsorbent. Other nano structures caught attention after Buchministerfullerene (C60) was introduced in 1985[45] and carbon nanotube in 1991.[46] Fig. 2.1[47] shows the general structure of Buchministerfullerene (C60) and single walled carbon nano tube (SWNT). Because of several possible hybridizations of 2s and 2p

orbitals of carbon, different dimensionalities can be obtained, such as, fullerene (0D), carbon nano tubes (1D), graphene (2D), diamond (3D). In recent years nano structured carbon materials like single and multi wall carbon nanotubes (SWNT, MWNT)[7-11], carbon nanohorns[12] fullerene[13], graphene[14,48], etc. have gained lot of interests after hydrogen storage potential of SWNT was demonstrated.[7] In addition to the porous nature, effect of curvature, large surface area, and capillary effect result in high adsorption capacity in these materials.
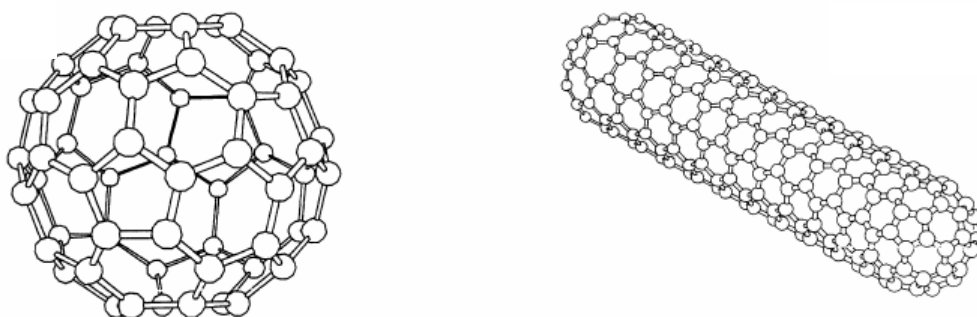
Fig. 2.1 Carbon nano structures fullerene and carbon nanotube[47]
(Reproduced with permission from ref. 47, copyright (1992) American Physical Society)

2.1.2   Metal Organic Framework (MOF)

Metal organic frameworks (MOFs), first introduced in 1999[27], are promising materials. MOFs are porous hybrid crystalline materials made up of metal oxide clusters connected by organic linkers.[27-29] In the simplest structure, Iso-Reticular MOF-1 (IRMOF-1), the cubic crystal is formed by positioning Zn_4O clusters at the vertices and connected by benzene-dicarboxylate (BDC) linkers, leaving most of the crystal volume free as empty space (Fig. 2.2[28,49]). Due to such structures, they have high porosity and large surface area.
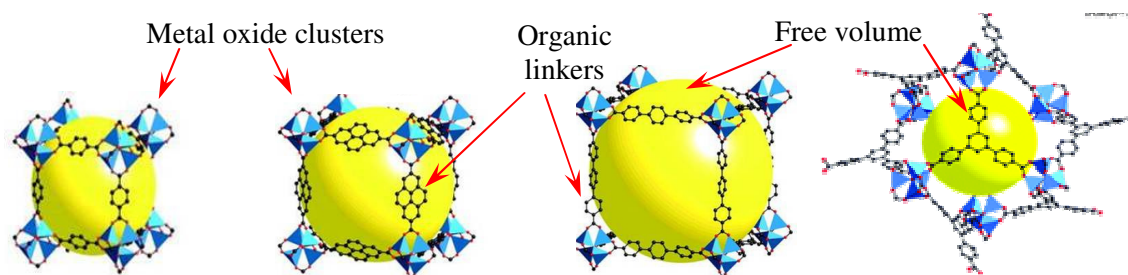
Fig. 2.2 Various Zn based metal organic frameworks[28,49]
(Reproduced with permission from ref. 28, copyright (2002)AAAS and from ref. 49,
copyright(2004) American Chemical Society)

These materials are interesting because of their flexibility in designing new structures, ease of preparation and structural stability. The design flexibility is achieved by choice of different combinations of metal clusters and organic linkers. One variant of MOF called covalent organic frameworks (COF), are made up of C, H, B, O, and thus have strong C-C, B-O and B-C covalent bonds.[50] These have the lowest density of any crystalline material, 0.17 gm/cc for COF-108. These are also promising materials for hydrogen storage.

2.2   Adsorption

Hydrogen storage may be achieved by adsorption process. In this process, when a hydrogen molecule comes in contact with a solid surface it tends to bind to the surface depending on the nature of interaction it experiences with the surface molecules.[51] Thus, adsorption depends on available surface area. This is different from absorption when molecules penetrate into the mass of the material. Both these terms are called 'sorption'.

Adsorption is the consequence of the forcefield present at the material (adsorbent) surface which attracts the gaseous molecules (adsorbate). Depending on this forcefield, adsorption can be two

types, physical - physisorption (by weak van der Waals attraction by weak dipole) or chemical-chemisorption (strong covalent, ionic bonding, transfer of electrons).

2.2.1   Chemisorption

In chemisorption, molecular hydrogen dissociates in two atoms and makes strong bonds with the adsorbent thus making metal hydrides or chemical hydrides. The adsorption enthalpy may exceed 100 kcal/mole and the process may be either endothermic or exothermic. Chemisorption and subsequent desorption rate depends on some finite activation energy (~20 kcal/mole), and thus this process is temperature dependent.[51]

A large number of metals and alloys can store hydrogen at relatively low temperature and pressure by chemisoroption, forming metal hydrides.[5] However, chemisorption on the hydrides suffers from problems like high temperature operation, slow kinetics, and low gravimetric contents.

2.2.2   Physisorption

Physisorption, on the other hand, is based on week van der Waals interaction between the adsorbate and hydrogen molecules having enthalpy change in the order of 2-6 kcal/mole. The rate of physisorption is fast and the process is easily reversible. The rate of adsorption also depends on how fast the molecules are transported to the surface (diffusion) rather than adsorption. The activation energy for physisorption is less than 1 kilocalorie and for subsequent desorption, it is seldom greater than a few kilocalorie. In physisorption, the amount of gas adsorbed decreases monotonically as the temperature increases, and a very insignificant amount is adsorbed at temperature exceeding normal boiling point of the gas.[51] Porous materials like

metal organic framework and carbon nano structure are the candidates for this type of adsorptive gas storage, as they have large surface area.

The amount of material adsorbed on the surface at different pressure and at a given temperature is called adsorption isotherms. These can be of various types.[51] However, adsorption phenomena on Metal Organic Frameworks (MOF) and carbon nano structures can be treated by using Type 1 adsorption isotherm or Langmuir isotherm. In this case, the amount adsorbed gradually increases and then reaches to a plateau. This represents formation of a monolayer. Hydrogen is stored in these materials between 77 K and 298 K (room temperature). Since these temperatures are considerably higher than the critical temperature of hydrogen (33 K) only monolayer adsorption or Type–I isotherms are obtained. Desorption should trace back adsorption path if there is no hysteresis.

The amount of gas adsorbed per gm of solid at equilibrium depends on the pressure (P), temperature (T), nature of the gas and the solid and is given by:

$$n = \frac{KPn_m}{1+KP} \tag{2.1}$$

where n = number of molecules actually adsorbed,

$\quad K$ = equilibrium rate constant,

$\quad P$ = pressure,

$\quad n_m$ = monolayer adsorption capacity.

The equilibrium rate constant $K = e^{(-\Delta G/RT)} = e^{(-\Delta H/RT)} e^{(\Delta S/R)}$

Thus high surface area materials are promising in this case. For hydrogen, the change in entropy, $\Delta S = -8R$ for a variety of adsorbents.[52] R is the universal gas constant. This equation may be used

to find out desired temperature for a particular loading and unloading gas pressure. For example, by taking reasonable pressure for adsorption at 30 bar and delivery at 1.5 bar, ΔH optimum becomes -15.1 kJ/mol at room temperature. But the heat of adsorption on carbon materials is around - 5.8 kJ/mol, thus it necessitates a storage temperature of 115 K (-115 ^{0}C).

2.2.3   Combined chemisorption and physisorption

Physisorption and chemisorption are the two extreme cases of hydrogen interaction. Researchers are striving to combine these two mechanisms to design storage materials that will effectiveness. For example, electrostatic interaction between hydrogen and charged molecules is stronger than van der Waals interaction. Doped molecules like Li, may transfer charge to a system and increase the interaction. Light alkali and alkaline earth metal (Li, Na, Be, Mg, Al) can make strong complex with hydrogen with energy 4 to 100 kJ/mole. Sigma (σ) donation is common in transition metal chemistry, where H-H electron is forward donated to a low lying metal vacant d orbital and subsequently back-donated from metal to antibonding σ^* hydrogen orbital. This is called Kubas complex. This complex can achieve high binding energy $\sim$ 20 to 160 kJ/mole, midway between dispersive interaction and hydride formation.[53] All these interaction can be achieved in the porous material by judicious selection of the structural components while designing these materials to increase hydrogen storage capacity.

2.3   Adsorption measurement techniques

2.3.1   Experimental methods

Hydrogen adsorption is measured by either gravimetric or volumetric method. When a highly dispersed solid is exposed to a gas in a confined space, gas is adsorbed on the surface. In this process, the bulk gas pressure decreases and the solid weight increases. The amount of gas

adsorbed can be calculated from the decrease in gas pressure or increase in the weight of the solid. For gravimetric method, change in weight and in volumetric method, change is pressure is noted as an indication of adsorption. Heat of adsorption can be obtained by using Clausius–Clapeyron equation to the adsorption data at two different temperatures.[54] For carbon nanotube, electrochemical method[55] is also used to measure adsorption capacity along with the two methods mentioned above.

To get better insight into adsorption process several other methods are also used. For example, inelastic (and quasielastic) neutron scattering is performed to understand hydrogen localization within a structure.

2.3.2   *Theoretical and computational methods*

The physical property of the hydrogen gas in a confined nanopore may be different from normal gaseous behavior in relatively unconstrained space.[56] The available experimental methods and measurement techniques may not accurately predict adsorption behavior of hydrogen gas in this case. Theoretical calculation using Grand Canonical Monte-Carlo simulations (GCMC) with accurate forcefield (FF) and host-guest interaction potential can be useful to predict adsorption behavior.[56] Theoretical investigations are also performed by ab initio density functional theory (DFT) to calculate hydrogen binding energy and binding sites on the host molecule. Molecular dynamic simulation (MD) can be performed to study hydrogen diffusion behavior in the porous structure.

2.4   Hydrogen sorption capacity of MOF and SWNT

As mentioned before, for individual MOFs, the adsorption isotherm looks like Type-I isotherm.

Fig. 2.3[57, 58] shows some examples of individual adsorption isotherms for various MOFs.
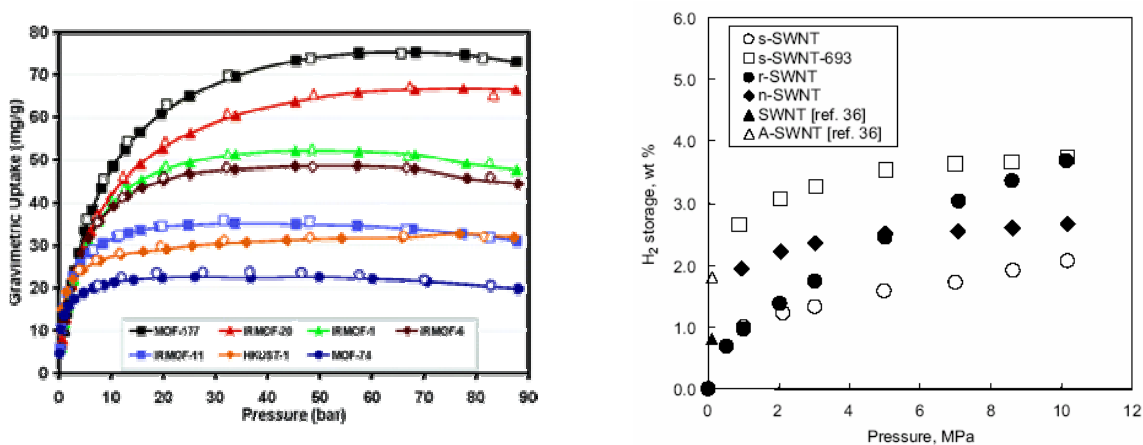
Fig. 2.3 Adsorption isotherms for different MOFs and SWNT at 77 K[57, 58]
(Reproduced with permission from ref. 57, copyright (2006) American Chemical Society and
from ref. 58 copyright (2007) Elsevier)

According to Fig. 2.3, MOF-177 shows 7.6 wt% hydrogen uptake at 77 K and 70 bar and it is

one of the highest adsorbing MOF. It has high surface area, ~4500 m^2/gm, which correlates with

its high sorption capacity. The adsorption in single walled carbon nano tube also obeys Type-1

isotherm.[58] Oxidized SWNT at 693 K (designated in the   as s-SWNT-693) has high storage

capacity ~3% at 77 K and 2 MPa pressure compared to other SWNTs or other carbon materials.

2.5   Factors affecting physisorption in MOFs and carbon nano structures

In case of MOFs three different adsorption regimes exists[59]:

1) At low gas loading (low pressure), adsorbed amount correlates well with the heat of

    adsorption;

2) In the intermediate loading, adsorption correlates with the surface area; and

3) At high gas pressure adsorbed amount correlates with the available pore volume.

Hydrogen sorption capacity on nanoporous materials depends on various physical aspects and chemical nature of the structure. Factors like available surface area, pore volume and geometry are the physical aspects, whereas heats of adsorption, surface chemistry are the chemical aspects. These are discussed in the following subsections.

2.5.1 Physical factors

2.5.1.1 Surface area and pore volume

Surface area and pore volume are the two main features of a porous material. Hydrogen physisorption is a surface behavior, thus in general, higher surface area leads to higher adsorption capacity. A comparison between hydrogen sorption capacities of various materials are given in Fig. 2.4.[60]
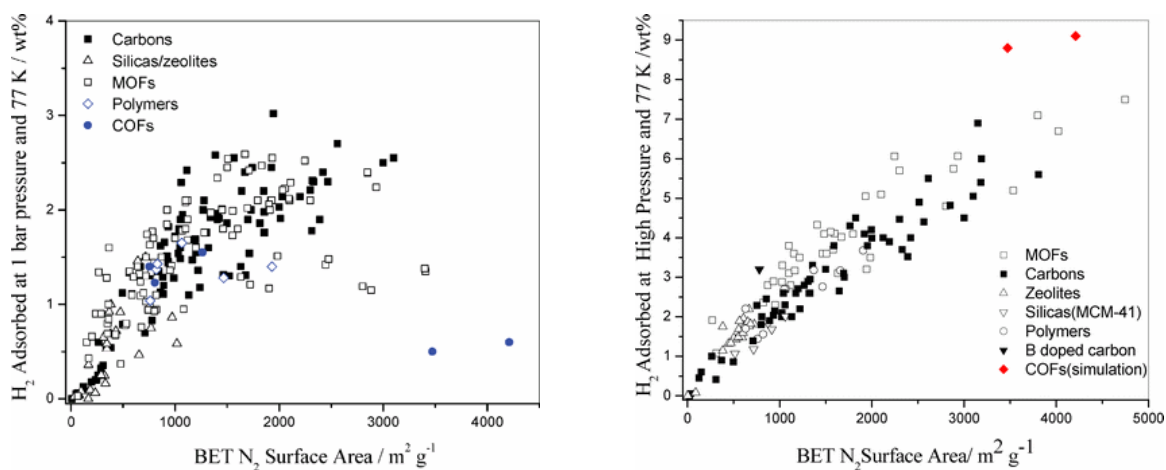
Fig. 2.4 Hydrogen adsorption by nanoporous materials at 77K at different pressure[60]
(Reproduced with permission from ref. 60, copyright (2005) Royal Society of Chemistry)

In general, carbon materials and MOFs have similar capacities at low pressure, but they have slightly different capacity at high pressure. At low pressure, the values for COF (covalent organic frameworks) are less because they have very high pore size which is ineffective in hydrogen storage at low pressure. However, the scenario is different at high pressure, when these COFs have the highest capacity (since they have the highest volume). Most widely used carbon material, activated carbon has a specific surface area of ~3000 m^2/gm and for a single graphene sheet it is around 1315 m^2/gm. Some researcher[8] predicted that to meet 2010 DOE target a surface are on carbon material of more than 4000 m^2/gm is required, which is not yet achieved.

The ideal pore size for monolayer hydrogen adsorption is the van der Waals diameter of hydrogen which is 2.89 Å.[61] Considering a confined pore where hydrogen is adsorbed on both the walls, an effective pore diameter should be 6 to 7 Å at low pressure and ~ 9 Å at high pressure.[54] Most MOFs have much larger non optimum pore size (e.g. IRMOF-1 having ~11.9 Å), which is far too large for hydrogen adsorption and leads to unused volume at the center. Different strategies have been used to achieve higher surface area. Some of these are mentioned below.

When linkers have functional groups like bromo, amino, fused benzene, etc., that penetrate inside the pore, they selectively improve the surface area and hydrogen adsorption property.[61] The interlayer distance in graphite is around 3.35 Å, which is low for hydrogen intercalation. Thus introducing alkali metal, metal halide, fullerene, or by mechanical ball milling may increase specific surface area.[8]

Surface area can be also increased by catenation[54, 61-63] of two similar frameworks as depicted below in Fig. 2.5[61]. Catenation decrease pore size. Catenation can increase surface area by upto

41%, by overlapping the potential field.[62] It is effective for a low pressure adsorption but is not good for high pressure. For example, catenated structure PCN-6 shows significant improvement in hydrogen storage capacity compared to the single structure PCN-6' (6.7% at 77 K 50 bar vs. 4% at same condition).[62] Catenated structure IRMOF-13 exhibited high storage capacity due to increased surface area.[63]
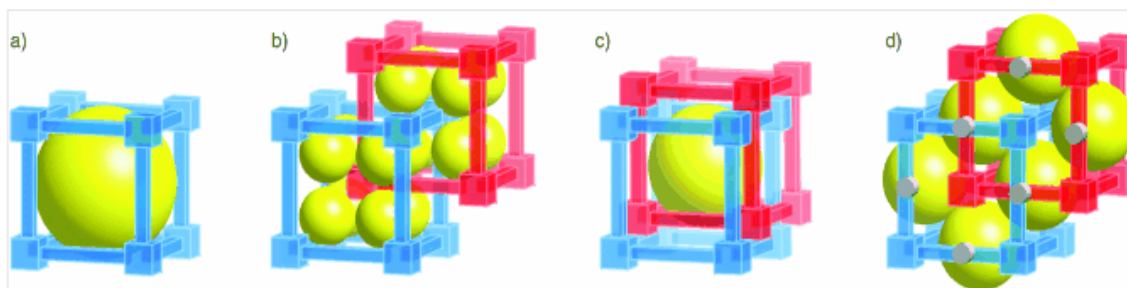
Fig. 2.5 Catenation of framework for improving surface area in MOF[61]
(Reproduced with permission from ref. 61, copyright (2005) Wiley-VCH, Verlag)

2.5.1.2 *Geometry and pore size*

A curved surface or a confined pore is more effective to bind more hydrogen rather than a flat surface due to overlap of potential field from surrounding walls.[64,65] It was estimated that curvature can enhance interaction by a factor of 1.134.[65] This observation has been made for both, MOFs and carbon nano structures. One of the MOFs, MIL-101 has pores with two sizes. The smaller pore fills first because is has high interaction potential, and the larger pore empties first because of low interaction.[54] For carbon nanotubes a tube diameter of ~2 nm was found to be optimum for maximum adsorption.[7] All these evidences indicate that an optimum pore size is required for efficient adsorption.

2.5.1.3 Pressure and temperature effect

Adsorption capacity decreases sharply with increase in temperature and decrease in pressure. Since the critical temperature of hydrogen is very low (33 K), at room temperature (298 K), very small amount of gas is adsorbed, unless the metal to gas interaction is enhanced by some mechanism. This observation is same for both MOFs and carbon nano structures. To give an example, H_2 uptake on MOF-177 at room temperature is only 0.62 wt% at 100 atm[57] compared to 7.6% at 77 K.

2.5.2   Chemical factors

In order to improve hydrogen storage capacity of a material, the first objective should be to have as many binding sites as possible to maximize hydrogen adsorption. The second objective should be to optimally design the binding sites so that the hydrogen bonding is neither too strong to make the process irreversible, nor too weak to make the gas to surface bonding unstable.

MOF crystal can have multiple hydrogen binding sites. For example, in IRMOF-1 (as shown in Fig. 2.6a[66]), the primary binding site is on the Zn_4O cluster and the other major site is with the benzene dicarboxylate (BDC) linker. However, with increasing hydrogen loading the hydrogen molecules start binding more to the BDC but not with Zn cluster. Four different types of binding location have been found on the BDC linker itself.[66] For carbon nanotube bundles, the major binding sites are the exohedral sites (channels in between the nanotubes), followed by grooves, pores and surfaces (Fig. 2.6b[67]).
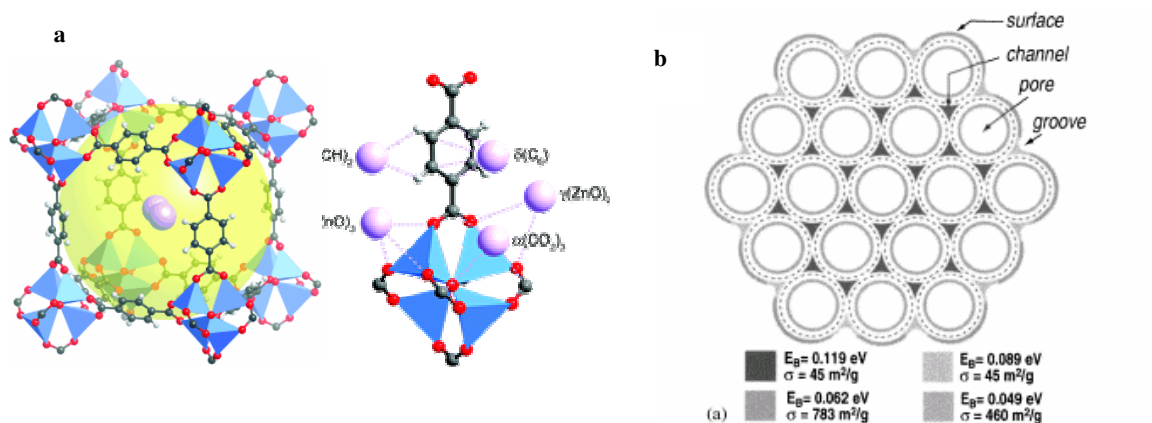
Fig. 2.6 Primary binding sites on (a) MOFs and (b) CNT bundles[66, 67]
(Reproduced with permission from ref. 66, copyright (2005) AAAS and from ref. 67, copyright (2002) Elsevier)

The optimum binding energy for hydrogen adsorption at room temperature is about 15 to 20 kJ per mole of hydrogen.[61] But the adsorption energy reported for various materials[60] are (i) carbons: 1.4–12.5 kJ mol^{-1}, (ii) zeolites: 5.9–18.2 kJ mol^{-1}, (iii) silicas: 5.4–10.4 kJ mol^{-1}, (iv) MOFs: 5.1–13.5 kJ mol^{-1}, (v) COFs: 2.7–8.8 kJ mol^{-1} (GCMC simulation studies). Higher binding energy can be reached in MOFs by 1) enhanced physisorption by modification of the linker chemistry, 2) introducing open metal sites, 3) metal doping to obtain Kubas complex, 4) hydrogen spillover, etc. These strategies are discussed below.

2.5.2.1 Linker chemistry

Linker chemistry plays a major role in adsorption process. The structure and presence of certain functional groups in the linker molecules can improve the quality of the active sites and overall sorption behavior. Interaction of hydrogen with various aromatic linker molecules have been studied theoretically by various groups.[68-72] By attaching right kind of functional groups in the benzene ring, one can increase the quality of adsorption sites. Higher electron densities in linker

molecules enable stronger hydrogen binding. Therefore presence of electron donating functional groups like amino, methyl, hydroxyl, etc., in benzene linker favors hydrogen sorption.

Oxygen and fluorine have higher electro negativity and lower capability to donate electrons to the benzene ring and thus reduces the affinity for hydrogen. Binding energies of naphthalene and anthracene are slightly higher than benzene probably due to their higher electron densities.[68, 71] Linker functionalization with Li alkoxide obtained enhanced hydrogen adsorption of 10 wt% at 77 K, 100 bar and 4.5 wt% at room temperature.[70] Negatively charged sulfonate group (SO_3^-) along with Li seem to significantly increase the hydrogen interaction by three times.[72] Carbon nano structures have been covalently functionalized and were predicted to have higher storage capacity. [17, 21]

All these imply that one can facilitate more hydrogen binding by: (1) carefully choosing linkers; (2) increasing the number of linkers; and (3) choosing the right functional groups in the linkers.

2.5.2.2 *Unsaturated metal site*

Coordinatively unsaturated metal sites can increase hydrogen binding capacity by orbital interaction. In some MOF, water or some solvent molecules attached to some metal may be removed by heating, while keeping the framework intact. The examples are HKUST-1 with Cu^{2+} open site[73], MOF-74 with Zn^{2+} site[63] and PCN -9 with Co site.[74] Neutron power diffraction showed strong interaction with these sites. Exposed Mn^{2+} sites and free Mn^{2+} in channel increases hydrogen uptake substantially.[75] The adsorption was 6.9 wt% at 77 K and 90 bar, with heat of adsorption being 10.1 KJ/mole. MOF-74 containing Zn^{2+} open site shows highest binding enthalpy ~ 8.8 KJ/mole and hydrogen storage capacity higher than MOF-177. Binding energy can be increased by 10-25 KJ/mole by introducing transition metal by making Kubas type

bonding.[76,77] However not all transition metal hydrogen interaction is Kubas type. For example, a theoretical study on Mn $^{2+}$ MOF which shows increased hydrogen binding does not show characteristics of Kubas complex (enhanced bond length, higher bonding energy). These indicated the role of higher electrostatic interactions at unsaturated metal site in increasing adsoprtion.[78]

Similar strategy of increasing binding energy by forming Kubas complex has been successfully adopted for carbon nano structures.[53] Organo-scandium bucky ball, where each Sc species can bind upto 11 hydrogen atom, resulting in 7-8.77 wt% hydrogen with binding energy 2.8 ev (~ 55 kcal/mole) has been proposed. Fullerenes, decorated with titanium, vanadium, niobium, have been synthesized and are other possible hydrogen storage materials. Carbon nanotube decorated with titanium has demonstrated strong hydrogen binding energy.[26] At high Ti coverage, adsorption capacity can go upto 8 wt%. The authors proposed that transition metals with filled and unfilled *d* orbitals are the right candidate for this type of complex formation. Here complex with Ti makes hybridization between Ti-d, hydrogen σ^* antibonding and SWNT C-p orbitals. However, heavy transition metals like Pt/Pd make classical hydride cluster, but that is not bonded to the tube.

Open metal sites are beneficial to increase surface packing density (SPD).[76] SPD is the mass of hydrogen adsorbed on a unit area. The SPD value obtained for MOF-74 was 3.2×10^{-5} gm/m^2 compared to 2.0×10^{-5} gm/m^2 on activated carbon and 2.8×10^{-5} gm/m^2 for triangular packing in a plane at 77 K. The distance between the metal and hydrogen has been found to be 2.6 Å in Mn -BTT, Cu-BTT (BTT- benzenetristetrazole), HKUST-1 and MOF-74 resulting in high adsorption energy of 10.1, 9.5 and 6.6 and 8.8 KJ/mole respectively. The D_2-D_2 interlayer distance (similar to H_2-H_2 distance) of 3.4 Å was smaller than that found in solid D_2 (3.6 Å).This close distance

between hydrogen molecules have resulted in high SPD, which is beneficial for enhanced sorption capacity.

2.5.2.3 Chemical doping

Presence of light metals (Li^+, Na^+, Mg^+, Al^{3+}) in the MOF framework can increase number of binding sites and improve hydrogen storage capacity.[71,79] The light metals are capable of clustering several hydrogen molecule bound by electrostatic charges or orbital interaction rather than purely dissipative (van der Waals) interaction. A MOF decorated with Li, showed a large hydrogen binding energy of 12 kJ /mole which is higher than that in case of only BDC (5 KJ/mol). This MOF achieved a hydrogen adsorption of 2% by weight at room temperature (300 K) and 5.4% at 77 K. But these systems are difficult to materialize in reality. A hexagonal MOF named IRMOF-2-96-Li, having similar topology as in MOF-177 having Li doped bigger linkers have been proposed.[80] This MOF has large surface area of 5175 m^2/gm. The calculated hydrogen storage capacity is 6.5 wt% at 243 K (-30 ^{0}C) at 100 bar, that meets 2010 DOE target.

Lithium or potassium doped SWNT demonstrated adsorption of ~20 wt% and ~14 wt% respectively, at moderate temperature and ambient pressure.[10] These hydrogen molecules first bind to Li and then spill over to CNT making hydrogenated CNT. Some researchers optimized the number of Li that can bind to CNT[81] (Fig. 2.7b). A configuration of 8 Li bound on the hollow side of the tube lead to higher sorption capacity. These tubes can release hydrogen at high temperature. They postulated that the best dopants are those atoms whose bands overlap strongly with H_2 and nanotube similarly and thus result in ionizing all carbon atoms. The calculated binding energy was -0.17 ev/H_2, which is close to DOE target of 0.2 ev/H_2. Enhanced

hydrogen storage (6.2 wt %) has also been predicted theoretically in case of Ca coated fullerene[82] (Fig. 2.7a) and Pt dispersed multi wall CNT (3.1 wt % at 298 K).[83]

$R_{H2} = 0.757$
$R_{Ca-H2} = 2.621$
$E^b_{H2} = 0.11 eV/H_2$
Weight%= 6.2%

$C_{60}Ca_{32}H_{60}^- \cdot 32H_2$

a. Ca coated fullerene [82]　　　　　**b.** Li decorated SWNT [81]
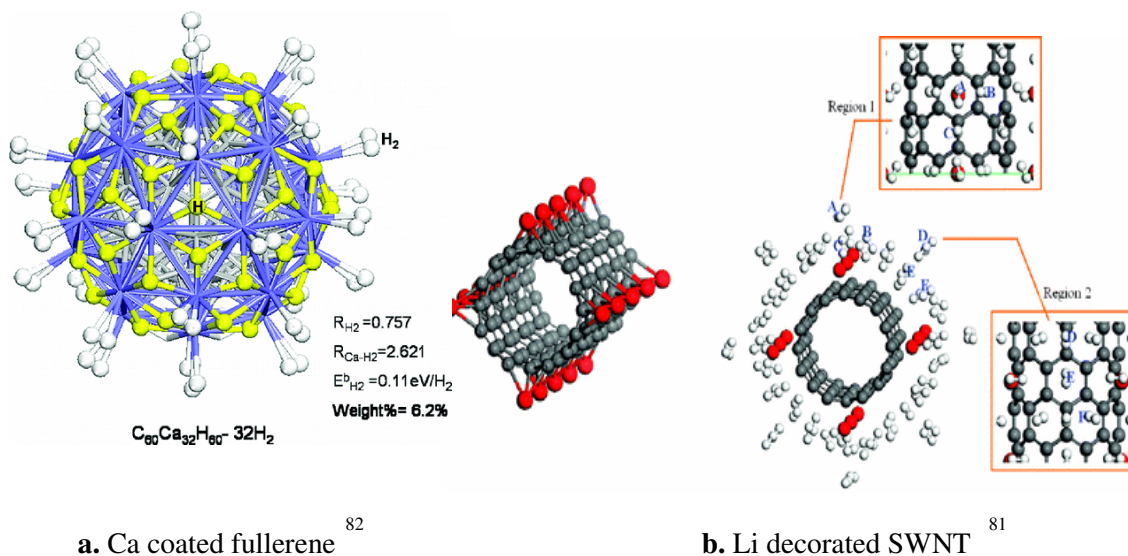
Fig. 2.7 Metal doped carbon nano structures
(Reproduced with permission from ref. 81 & 82 copyrights (2009) American Chemical Society)

Metal clustering and subsequent degradation of the cluster is a problem is case of transition metal doped carbon nano structures. Boron doping can control the ionic state of these metals by acting as acceptor sites and thus preventing metal clustering. Boron doped graphene was found to be effective in Ca dispersion and subsequent high adsorption capacity.[84]

2.5.2.4 *Spill over mechanism*

Spillover mechanism can improve hydrogen adsorption.[85-87] In this process, hydrogen is rapidly adsorbed on the metal site and dissociates into atoms. These atoms then move to the receptors. Use of bridging molecules can enhance this transfer. In IRMOF-1 and IRMOF-8, hydrogen storage by spillover was increased by a factor of 3 when Pt was used as metal site and this

resulted in 1.8 wt% adsorption at room temperature.[85] The results were further improved by using a glucose precursor which acts as a bridge for hydrogen transfer to the receptor, i.e. MOF. The storage capacity in MOF-177 at 298 K and 10 MPa increased by 0.8 wt% by mixing MOF-177 with Pt/AC catalyst.[86] Similar observation was made for CNT.[87] MWNT synthesized by metal oxide catalyst (NiMgO) adsorbs higher hydrogen. In this case, the researchers found that residual catalyst used in MWNT synthesis takes part in hydrogen spillover and thus increases adsorption.

2.5.3   Other factors

2.5.3.1 Surface defects

Presence of defect like hydrogenated site with C-H bond, or oxidized sites tend to effect hydrogen sorption in the carbon nanotube. Hydrogenated sites tend to reduce adsorption whereas oxygenated sites improve it[88] by opening a large specific surface. Promisingly high value of surface adsorption capacity is not only due to pure adsorption but may be due to the presence of impurity, amorphous carbon, altered surface chemistry.

2.5.3.2 Diffusion

Hydrogen adsorption kinetics in MOF and SWNT depends on hydrogen diffusion inside the pores. High diffusion means gas molecules are rapidly transported to the active sites and hence gets adsorbed quickly. Self diffusivity of hydrogen in SWNT is 3 to 4 times higher compared to another porous material, zeolites, and diffusivity increases with decrease in tube diameter. Tube chirality does not affect the diffusivity.[89, 90] Higher curvature result in smooth potential energy surface and thus increase diffusivity. Diffusion in MOF is also 2 to 3 times higher than zeolite

having similar pore size.[91] Higher diffusivity in MOF is attributed to the high pore size and chemical environment in the pores and thus diffusivity varies depending on these factors.

2.5.3.3 Composite structures

Strategies like shearing along the face or body diagonal; impregnation with non volatile guest molecule such as fullerene; etc.[61], have been suggested to improve the hydrogen storage in MOF. Covalently cross linked SWNT shows improved hydrogen storage.[17] New exotic structures like fullerene intercalated graphite (Fig. 2.8a[13]) showed 9.1wt% storage capacity at 200 K and 3.5 wt% at room temperature, pillared graphene[14] (Fig. 2.8b[14]) connected by (6,6) SWNT showed ~ 6.1 wt% uptake at ambient condition.
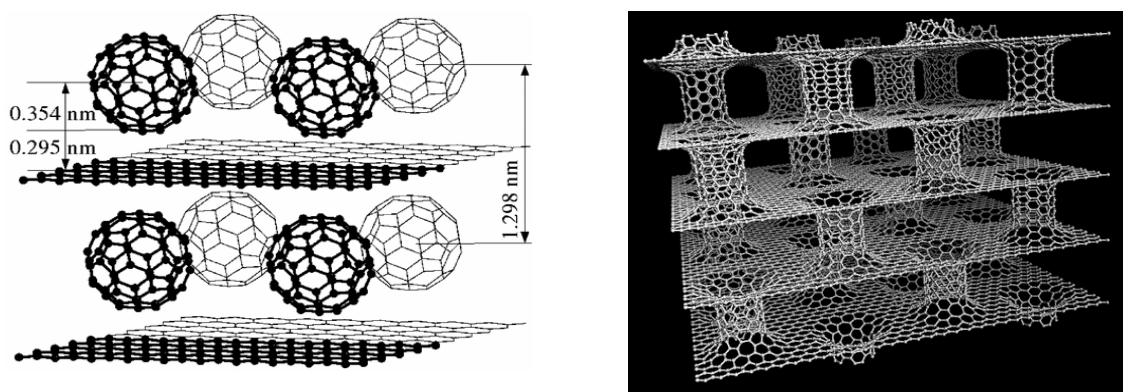
Fig. 2.8 Fullerene intercalated graphene and pillared grapheme[13, 14]
(Reproduced with permission from ref. 13 & 14, copyrights (2007 & 2008) American Chemical Society)

2.5.3.4 Method of preparation

Adsorption capacity also depends on the method of preparation, sample purity, activation method, degassing temperature and time, etc.[92] Smaller sized samples tend to give higher result than larger size, probably because larger sized samples take long time for diffusion and to reach

equilibrium adsorption capacity compared to smaller sized sample. SWNT activated by mild oxidation in CO_2 increases the hydrogen uptake, probably due in increase in tube spacing change in potential field between the tubes.[92] In order to allow hydrogen access inside the tube, tubes must be open at the end. Nanotube characterization has revealed that the tubes tend to be capped by fullerene at the end, but these can be opened by ultrasonic treatment, ball milling or oxidation.[93] Open nanotubes can be synthesized also. Ball milling can destroy crystalline structure at places and thus opens traps for hydrogen storage. Carbon nanoropes and nanofibers, which are two dimensional structures, have higher adsorption capacity than just SWNT, due to large surface area and interstitial spaces. Storage capacity was found to enhance when CNT was annealed at 1700 to $2200^0 C$ temperatures, probably due to opening of pores.[93]

2.6   Physico-chemical property of MOF structures

In order to design a MOF based devices we need to study the physical and chemical properties of that MOF. In this regards, properties such as electronic density of states, mechanical behavior, phonon spectra, negative thermal expansion, and thermal conductivity are relevant. In this section we will discuss these.

2.6.1   Electronic density of states

Electronic density of states can give information about the chemical bonding environment present in a framework structure.[38,39,94,95] The band structure of MOF is rather flat and featureless. The highest occupied valence band comes from carbon p orbitals. The electronic property of MOF is marked by the presence of Zn_4O cluster, which makes the framework a semiconductor with band gap 2.5 to 3.5 ev. However the presence of benzene dicarboxylate linker tries to make the structure semimetallic. The electronic delocalization effect introduced by

benzene dicarboxylate (BDC) linker breaks of due to presence of Zn_4O and create band gap in the porous structure.

Partial density of states, as shown in Fig. 2.9[94], indicates that the top of the valence band (VB) is due to the hybridization of Zn *3d* states and *2p* states of O and C. Whereas the bottom of the conduction band is due to unoccupied *s* and *p* orbital of C, O, and Zn. Both oxygen *2p* wave functions are energetically close to Zn *d* orbital indicating strong interaction between them. This strong interaction leads to a stable MOF-5 structure. The *p* states of C1 and C2 carbon atoms, as shown in Fig. 2.9[94], are very close in the energy range indicating strong covalent bond.[94]
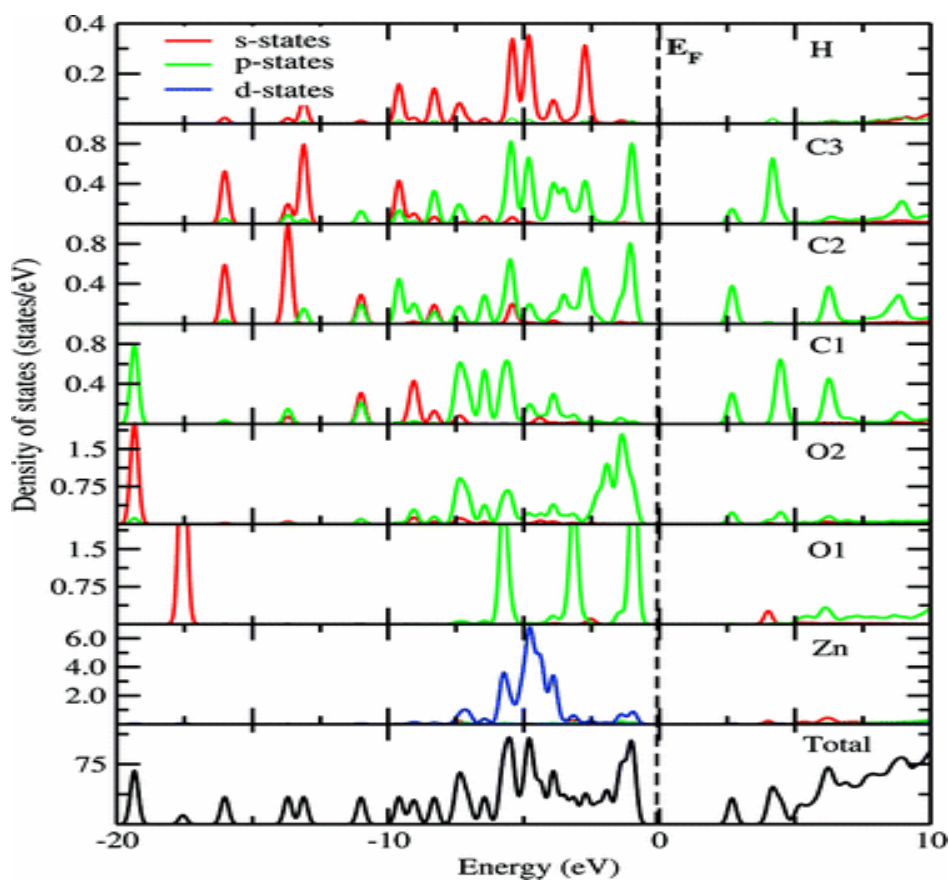
Fig. 2.9 Electronic density of states of MOF-5[94]
(Reproduced with permission from ref. 94, copyright (2010) American Chemical Society)

Bond localization function plot between C1 and C2 are higher than between other C atoms. Zn d state is well localized and the s electrons are transferred to neighboring atoms which creates ionic bond between Zn and O. However the charge transfer from Zn is not isotropic. The anisotropic charge transfer from Zn to the O sites indicates the presence of iono-covalent bonding between Zn and O. But the ionic bonding interaction dominates over the covalent interaction between Zn and O.

2.6.1.1 Phonon spectra

Phonon density of states can give us information about stability and dynamics of MOF-5 lattice. First-principles calculations using DFT-LDA and Neutron Inelastic scattering (NIS) are used to calculate phonon spectra.[40] The primitive cell of MOF contains two formula units of Zn_4O_{13} $(C_8H_4)_3$ which gives rise to total 318 phonon branches.[40] The crystal symmetry implies 105 Raman and 72 IR active modes. The NIS spectra is dominated by one phonon processes and two phonon processes are not significant.

The phonon spectra show that some of the modes have high dispersion such as those below 25 and 30 meV. This dispersion comes from the weak point where two rigid units (ZnO_4 and BDC) are linked. The lowest energy mode - $\Gamma A2g$, at 2.59 meV, is due to all C_6H_4 linkers twisting around the crystal axis. The second lowest energy mode is $\Gamma T1g$, at 3.12 meV and is due to two of three C_6H_4 linkers twisting around the crystal axis. These two softest twisting modes imply that the bond between the metal cluster and the benzene linkers are the weakest region of the crystal. Their interaction with the acoustic modes results in small shear modulus constant, C44, for these crystals.

The rotational energy barrier for benzene ring is quite large ~537 meV, but twisting by only a few degrees requires low energy, in order of meV.[40] These soft modes create twisting, stretching, breathing, bending, and wagging motions of the benzene rings which can be observed from MD simulations also and results in some interesting phenomena like the structural flexibility, negative thermal expansion of open frameworks.

2.6.1.2 Negative thermal expansion

Negative thermal expansion (NTE) is a peculiar material property that may have many technological applications in engineering of optical and electronic devices.[96,97] Experiment shows that MOF-5 has a large negative thermal expansion coefficient -16 x10^{-6} K^{-1} and theoretical calculations explains this NTE behavior. The soft phonon modes results in this NTE behavior. Usually there are four different reasons[97] for NTE: 1) shortening of bond length and phase change result in change in lattice parameter. 2) bridging atoms and rigid-unit vibrational modes (RUMs); 3) magnetostriction in case of ferromagnetic materials to change in lattice shape in presence of a magnetic field; and 4) electronic effects. Such NTE behavior is present in open nanoporous framework materials like zeolite, ZrW2O8. MOF-5 has a large group of soft phonons which leads to NTE.

In insulators like MOF, thermal expansion arises from anharmonic lattice vibration. Most of the low frequency phonon modes soften (value becomes lower) with increase in temperature leading to negative Grüneisen parameters and thus lattice contraction.[98] Many other MOFs also have NTE. The NTE gets more pronounced with increasing linker size.[99]

2.6.1.3 Flexible structural transition

Some MOF structures exhibits remarkable phase transition. The phase transition, called 'breathing effect', occurs due to external stimuli like pressure, temperature, light, guest molecule, electric, and magnetic field.[31,94,100,101,102,103,104] It involves atomic movement of 2 to 4 Å or even larger, even though the framework topology is maintained. Breathing effect may be by two ways[31] : 1) weak interaction between host and guest molecule by hydrogen bonds, van der Waals interaction, π-π interaction; 2) presence of weak point in the crystal structure. Too much breathing will limit use as molecular sieve, but then it can accommodate the difference in thermal expansion between the support and the framework.[105] Breathing property in MIL-88 class of solid increased the volume by 230%.[106] Temperature dependent breathing effect was observed in an aluminium variety of MIL-53. Dispersive interaction was considered to be responsible for this behavior which causes the *np* (narrow pore) structure to stabilize at low temperature, whereas, entropy drives the structural transition to *lp* (large pore) state. The driving force for this transition is due to low energy phonon modes and the dispersion interaction from π-π staking of the phenyl ligands.[102] Guest (water) dependent breathing effect was observed in MIL-53, Cr based MOF.[102] From theoretical calculation it was observed that there is a large energy difference (30 kJ/mole) between the large and narrow pore. The narrow pore with water molecule in it is a more stable structure (Fig. 2.10).[102]
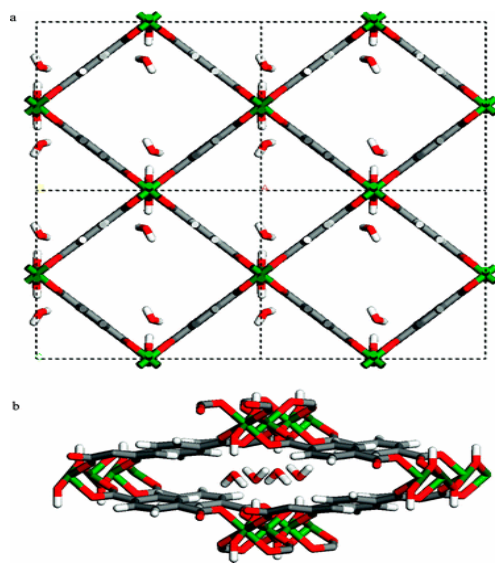
Fig. 2.10 Sorption induced breathing in (a) CrMIL-53 lp and (b) CrMIL-53 np[102]
(Reproduced with permission from ref. 102, copyright (2009) American Chemical Society)

2.6.2   *Mechanical property*

Mechanical properties of MOF have been studied mostly by theoretical methods[37-41] and also by a few experimental works.[35,36] It is important to understand mechanical properties of MOF to be able to rationally design MOF with optimal property for a particular application.[41] We have to know the mechanical behavior of MOF at high pressure environment as encountered in sorption application. We need this understanding to ensure that the open frameworks can exhibit good stiffness, rigidity and robustness to retain its structural integrity at high pressures. Also the interface strength of MOF layer and a substrate depends on the elastic and thermal expansion mismatch between the MOF and substrate. Moreover, lattice dynamics is important prerequisite to understand the quantum dynamics of adsorbed material. In general, various studies have described MOF-5 as soft ductile materials with highly anisotropic behavior. Major mechanical properties of MOFs are described below.

2.6.2.1 Elastic constant

Elastic constants, C_{ij} represents the stiffness of a material. Elastic constant can be calculated from a range of energies as a function of strain or lattice constant. Then this energy vs. strain is fitted to Birch –Murnagham equation to obtain Bulk modulus and other elastic constant. In case of MOF-5, this method may not be appropriate as total energy as a function of strain is not smooth.[39] To eliminate these issues, energy can be calculated by applying small strain (0.5%) in certain direction of the crystal and determining the corresponding variation in energy.[38,39] They found that MOF-5 is a soft and ductile material, with Young's modulus comparable to that of oak wood. The low bulk modulus in order of 16 to 18 GPa[37-41] indicates that the structure is easily compressible. C11-C44>0 indicates a significant deviation from a central intermolecular potential. Small C44 constant in order of 1.4 GPa[38] indicates that the structure is close to being structurally unstable and will collapse in to potentially useful structure under shear stress. Calculated bulk modulus for HKUST-1 (25 GPa) indicates that the material is stiffer than MOF-5.[107] MOFs with wider linker have lower C44 constant and MOF with longer linker has higher C44 constant.[108]

Fig. 2.11[109] represents the elastic modulus of various materials. Compared to other porous materials ZIF, MOF-5 has low elastic constant and thus the material is less stiff than ZIF and other materials.
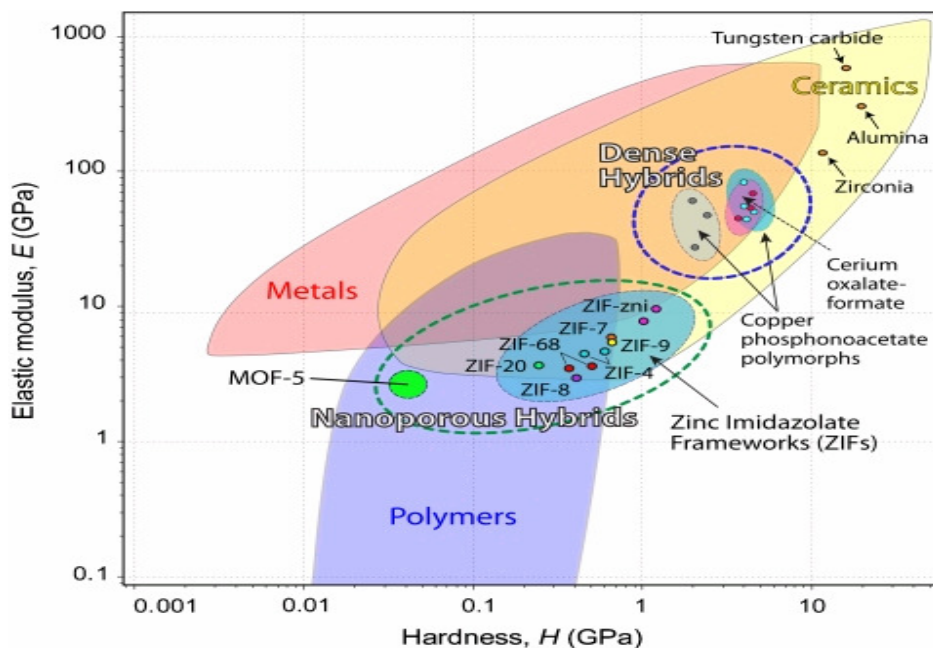
Fig. 2.11 Elastic modulus versus hardness property map for various materials[109]
(Reproduced with permission from ref. 109, copyright (2010) Proc. Nat. Acad. Sc.)

The elastic anisotropy is an important engineering factor that gives probability to induce microcracks. The anisotropy factor for MOF-5 is 1.39 indicating presence of anisotropy and indicates that the MOF-5 system will form microcracks in time. Poission's ratio also indicates the bonding force. For system with central ionic or van der Waals crystals this ratio is 0.25. For MOF this value is 0.36 indicating that the inter-atomic forces are non central. Theoretical value of Poisson ratio is ~0.15 at 10 K for some common MOFs. This is much smaller than the Poisson ratio of normal metals (0.3), ceramics (0.2–0.4), or polymers (0.4–0.5). The Debye temperature (D) and sound velocity gives an idea of the rigidity of the framework. The first principle calculation shows MOF-5 has low D value indicating it is a flexible system.[38]

2.6.3   Behavior under pressure

It has been suggested that because of the soft nature of the structure, MOF-5 may undergo phase transformation at high external pressure.[40] 'Density Functional Theory' with 'Local Density Approximation' (DFT-LDA) calculation by optimizing lattice position at pressure range from -0.5 to +0.5 GPa did not reveal any structural instability. Experimental studies[35,36] showed high pressure deformation for Cu-MOF (KHUST-1) at a pressure range of 0.8 to 2.2 GPa (depending on the pressure transmitting fluid) and 0.543 to 0.847 GPa for a Zinc Imidazole Framework. Using molecular dynamics simulations, we have shown that IRMOF-1, IRMOF-3, IRMOF-6, IRMOF-8 IRMOF-10 and IRMOF-14, undergo structural deformation and subsequent large scale volume compression at high pressures (~150-300 MPa) depending on the MOF structure.[108] MOFs with fused rings seem to be softer than single benzene ring which was evident from the low C44 constant and low deformation pressure. These high pressure induced deformation is reversible for some MOFs (with no gas inside the pores) with functionalized linker. Reversibility also depends on the presence of hydrogen inside the pore for some other MOFs. Although a recent experimental study[110] on MOF-5 crystal reveled that the structure is amorphized under a very low pressure around 3.5 MPa, which is 100 times lower than the pressure required for amorphization of other compounds. The compressed structure has a surface area of 6 m^2/gm compared to uncompressed structure 2816 m^2/gm. Difference between measured and theoretical behavior under high pressure may be due to the facts that 1) air exposure during measurement may make MOF5 crystal unstable,[111] 2) Real crystal may contain defects, grain boundary whereas the theoretical simulation deals with ideal, defect free crystal and thus require higher pressure for deformation.

2.6.4   Thermal conductivity

Phonon thermal conductivity of MOF-5 was calculated by using molecular dynamic simulation and Green–Kubo method.[112] The predicted thermal conductivity is low for a crystal having value of 0.31 W/m K at 300 K, and the temperature dependence is very weak. The phonon decomposition indicated that short range acoustic phonons and the optical phonons dominate energy transport. The long range acoustic phonons have little contribution and thus the structure behaves like amorphous at higher temperature. The porous structure of MOF leads to a low atomic mass density and the long flexible bridge and the heavy cluster results a low phonon group velocity. The cage bridge structure in the MOFs suppresses the long range correlation and reduces phonon mean free path and reduce conductivity.

2.7   Theoretical approaches to understand adsorbate-gas interactions

To design hydrogen storage materials with optimum hydrogen adsorption capacity, we need to exploit the combined effect of van der Waals force, electrostatic and orbital interactions. Therefore we need theories that can help us accurately model and predict various aspects of these interactions. Once developed these interaction models can be further used to predict structural properties of these hydrogen storage materials, thereby saving time and avoiding expensive synthesis process.[113] Various computational tools and simulation methods play an important role in accurately predicting and modeling of different phenomena related to hydrogen sorption in these nanoporous materials. These also enable evaluation of suitable adsorbates.

Various theories are available that can be used to model structure and behavior of materials at different scales, starting from electronic level and then subsequently covering atomic, molecular and crystal structure level. These enable us to calculate and predict hydrogen sorption properties

in MOF and carbon nano structures, related structural changes, transport properties and thermodynamics. These theories provide us with insights about: charges on the atoms, equilibrium bond angles and distance, lattice parameter, binding energy, binding location, hydrogen mass distribution in the framework and hydrogen diffusion which are important parameters for material design.

Fig. 2.12 summarizes how different theories and calculations at various levels are used to model behaviors at different scales. The results from finer scale (e.g. electronic scale) models are used as inputs to model behavior at the next level/scale of simulation. The final outcomes may be used to model the behaviors of MOF and carbon nano structures based H_2 storage materials. In Fig. 2.12, the grey boxes represent electronic calculation based theories. The pink boxes indicate parameters involving atomistic simulation and green boxes represent calculations and simulation outcomes (results) that may be used for designing H_2 storage device. The grey bars represent points in the computational flow where different inputs are used together to generate different results.
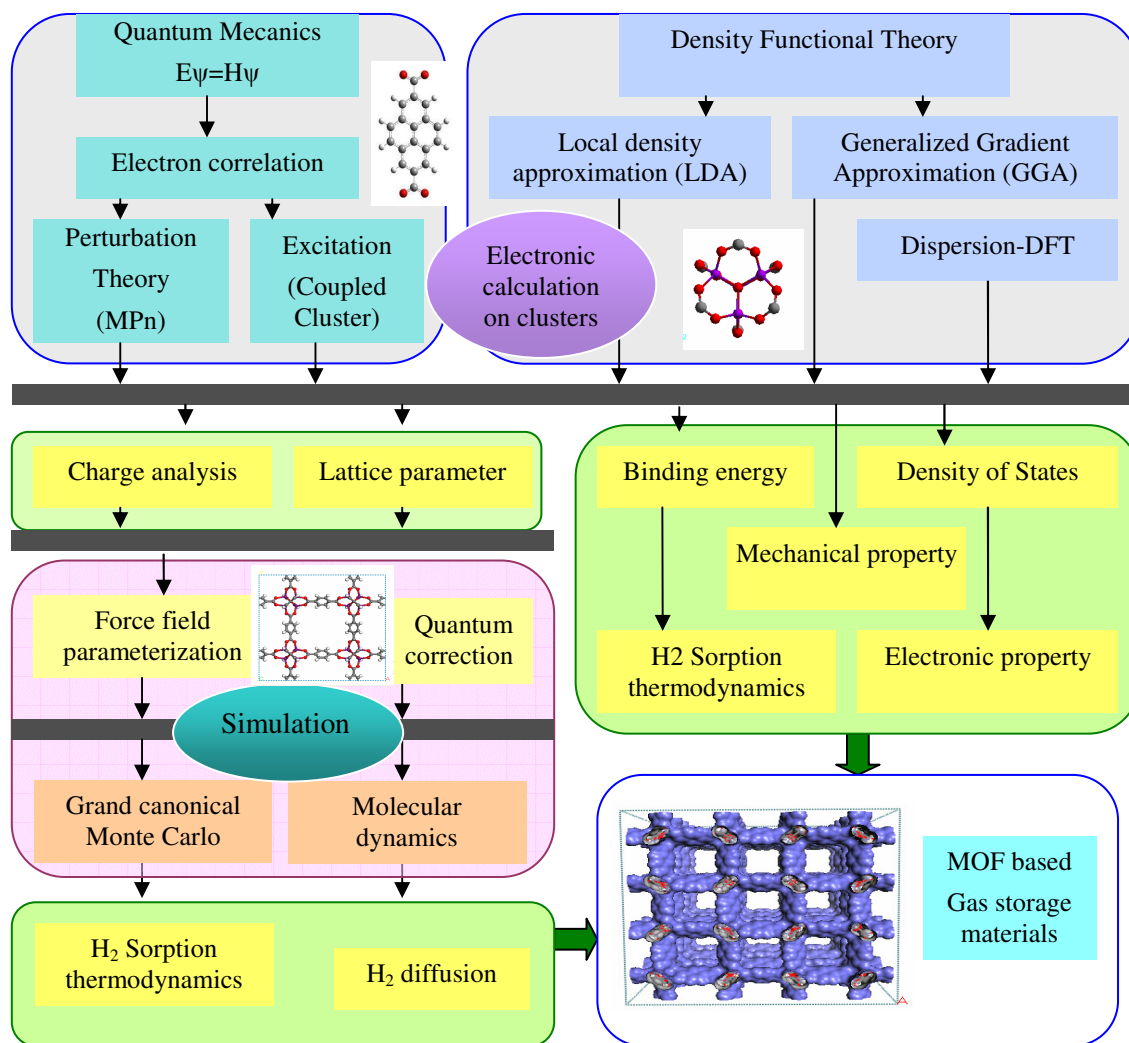
Fig. 2.12 Various level of theory used to study hydrogen sorption in MOF

Electronic scale modeling and calculations such as ab initio quantum mechanical calculation and density functional theory calculation can produce results about charges on the atoms, equilibrium bond angles and distance, lattice parameter, binding energy, binding location. These results may be further used to model the forcefield. Quantum correction may be introduced to improve accuracy of the result. The ab initio parameterized forcefield may be use to conduct molecular dynamics and Monte Carlo simulation to model sorption capacity, adsorbate mass distribution,

diffusion behaviors, mechanical stability. Finally all these may be used to model MOF and carbon nano structures based hydrogen storage device. Next we discuss some of these theories that are relevant for studying hydrogen storage in MOF and carbon nano structures along with examples of relevant results obtained from these theories.

2.7.1 *Quantum mechanics study on MOF and carbon nano structures*

The electronic calculations or Quantum mechanics (QM) study involves solving multibody Schrödinger's wave equation and then obtaining different observables by using appropriate quantum mechanical operators.[114] These ab initio QM methods are of different types, having different levels of accuracy and computational complexity. In an adsorbate system, QM study may be used to calculate atomic point charges, interaction energy and preferred binding sites in the framework, preferred orientation, etc., which may be used further for forcefield parameterization.

Quantum calculation is performed on clusters or isolated segments such as linkers or metal clusters, because performing calculation on the whole framework is computationally prohibitive. To accurately predict hydrogen interaction with adsorbate system, accounting for electron correlation is very important. Thus quantum calculation should be at least at the level of MP2 (Moller–Plesset perturbation theory with second order correction in energy).[114] It has a second order energy correction term due to electron correlation and dispersion to the Hartree-Fock energy.[114] MP2 calculation is considered to give better representation of the hydrogen-adsorbate interaction energy. MP2 calculation can be done fairly rapidly and scaling behavior is in order of N^5, where N is the number of basis set.[114] A basis set is a mathematical function that represents a molecular orbital. MP2 method may be further modified as in MP2-R12 method.[114] Here the

wave function is not for a single electron orbital but for all electrons and therefore includes all the relevant interelectronic distances (r_{ij}). MP2-R12 method requires very large basis set.

Another method of accounting electron correlation is by coupled-cluster (CC) theory.[114] It includes various level of electron excitation from the reference state. For example, CCSD means coupled cluster with single and double excitation. The scaling behavior of CCSD is in order of N^6. CCSD(T) methods includes a connected triples excitation arising from single/doubles coupling term. Triple excitation has very important contribution in the dispersion energy calculation and thus CCSD(T) method is considered to be more effective to calculate van der Waals interactions present in H_2 sorption in adsorbate. However, this higher level CCSD(T) theory produces accurate result in the cost of increased computation time.

When large, localized basis set with diffuse functions are applied, superposition errors (BSSE)[114], are unavoidable. Thus counterpoise correction (CP)[114] need to be evaluated, preferably with extrapolation to the complete basis set (CBS) limit. If this is not done, adsorption energy may vary by an order of 3 kJ/mole.[115]

Here we give an example of a QM calculation of hydrogen adsorption in adsorbate. In order to accurately determine the interaction energy Hubner et al[116] used a higher excitation and basis set extension. Higher excitation was used by coupled cluster (CCSD) method including all single and double excitation as well as non iterative perturbative estimate of the triple excitations [CCSD(T)]. Basis set extension was studied by computing MP2 interaction in basis set larger than TZVPP. It was found that the individual contribution due to larger basis set, inclusion of terms that are linear with electronic distance and inclusion of higher excitation all have similar

binding energy for different aromatic system like benzene, substituted benzene. Including higher excitation beyond MP2 level decrease interaction energy by 0.85 kJ/mole.[117]

The QZVPP basis set (quadruple ζ valence basis with polarization function) does not require augmentation and provide excellent result.[118] The QZVPP provides more flexibility and improved accuracy compared to the Dunning cc-pVQZ basis set. Because of large size and efficiency of QZVPP basis, reliable results may be obtained without BSSE correction.[118] The table below provides various ab initio calculations and the main findings from them. Table 2.1 below summarizes some of the example studies which used ab initio calculations.

Table 2.1   Examples of Ab initio calculations

Method	System	Findings
RI-MP2/cc-pVTZ, In Q-chem	BDC-X—H_2 (X= H, F, CH3, NH2, OH) NC^-, CN^-, CO, NO^+, Cp^-, F^- and SO^{2-}_4 Li^+, Na^+, Mg^{2+}, Al^{3+}	Uncomplexed ligands (F^- and SO^{2-}_4) bind H_2 with strong affinity. Enhanced binding for unsaturated or partially charged lightweight metal centers.[119]
RI-MP2 with TZVPP/with polarization function of cc-pVTZ basis set	C_6H_5X (X=H, F, OH, NH_2, CH_3, CN) $C_{10}H_8$, $C_{14}H_{10}$, $C_{24}H_{12}$, p-$C_6H_4(COOH)_2$, p-$C_6H_4(COOLi)_2$	Enlarged aromatic system increases interaction energy, extending basis set increase interaction energy, whereas including higher excitation decrease interaction energy.[116]
MP2 with Dunning correlation consistent basis set	H_2 binding on benzene	Binding energy is 4.77 kJ/mole very close to experimental value (4.99 kJ/mole), binding energy on Li decorated linker is higher.[120]
MP2 with QZVPP basis set, RI-MP2, MP2-CCSD(T)	IRMOF-1, IRMOF-3, IRMOF-6, IRMOF-8, IRMOF-12, IRMOF-14, IRMOF-18, IRMOF-993	Larger, wider linker is better and presence of NH_2, CH_3 increases binding energy.[118]
MP2 and coupled cluster with non iterative triple excitation, CCSD(T)	H_2 on benzene system	H_2 rotational spectra conforms to experimental INS result.[121]
RI-MP2 with QZVPP basis set	$Zn_4O(HCO_2)_6$, $Mg_4O(HCO_2)_6$, $Be_4O(HCO_2)_6$	Mg cluster has strongest interaction energy compared to Zn and Be.[122]

2.7.2   Density Functional Theory and calculations

Electronic structure calculation is mostly performed using Density Functional Theory (DFT). The main premises of DFT calculation is that the ground state energy of a non interacting system is a unique functional of the electron density. DFT calculation is a powerful tool to gain fundamental theoretical insight, and it provides sufficient accuracy in values while being several orders of magnitude more efficient and less CPU consuming compared to other techniques. It scales no more than N^3, where N is the number of basis function to represent KS (Kohn-Sham) orbital. [114]

DFT calculation may be performed in two methods, Local density Approximation (LDA) and Generalized Gradient Approximation (GGA). Comparison between these two methods may be necessary in order to eliminate any fundamental error margin between two levels of theory. Sometimes, the mean between LDA and GGA gives the most reliable results. Experimental lattice constants and bulk moduli often falls between the LDA and GGA values.[41] Experiments indicate interaction energy of H_2 on graphite 35 mev/mole while LDA gives 20 mev/mole and GGA gives 5 mev/mole.[39]

DFT calculation gives binding energy and binding sites on adsorbates. But DFT calculation does not consider electron excitation, and does not provide long range interaction. Thus calculating weak van der Waals interaction present in H_2^- adsorbate system is a challenge in DFT. LDA cannot give accurate values of weak dispersive interaction between two electron clouds which do not overlap. However compared to other pure density functional such as PW91 and PBE that involves similar computational cost, LDA gives better result.[39] As the adsorption energy gets larger due to charge transfer and polar interaction in addition to weak dispersive interaction, the relative accuracy of LDA increases. LDA tends to overestimate dispersive interaction. The

result of GGA depends on which exchange correlation is used. Functional such as PW91 and PBE are the best to model the weak interaction, of these PBE usually gives better result.[69] Table 2.2 present DFT calculations performed by various methods and the salient outcome from these.

Table 2.2   Examples of DFT calculations

Method	System	Findings
BLYP/6-311G(d) In Gaussian	Exposed Ni^{+2}, Mg^{2+} coordinated site	Ni^{2+} sites has higher binding energy. Energy depends on the geometrical arrangement (cis, trans) of the ligand.[123]
VASP –PBE exchange correlation	Exposed Mn^{+2} site also exposed Sc, Ti, V, Cr	Binding energy can be tuned between 10-50 kJ/mole by using different transition metal. Mn based MOF performs better.[124]
Qchem, with BP86 exchange correlation	Exposed Cr^{+2} site also exposed Mg, V, Mn, Mo coordinated complex	$Cr(Co)_3$ gives strongest binding energy 20-40 kJ/mole.[125]
PWscf package USPP-PBE exchange correlation	Mn^4Cl- MOF(open Mn^{2+})	Binding not Kubas type, Orientation has large effect on binding.[77]
Turbomole	Li- alkoxide linker with IRMOF-8, and 14	Li enhances adsorption at room (4.5 wt%) temperature Interaction energy 9.05 Kcal/mole.[70]
VASP, PAW-GGA	MIL-53 (Cr)	H_2 interaction mainly due to C and H atoms rather than Cr, because of its inaccessibility.[100]
VASP, Gaussian USPP, PAW	HKUST-1	Charge –quadrupole interaction has substantial impact on equilibrium and transport properties of H_2.[126]
VASP-GGA, PBE	Fe-IRMOF-16	4 H_2 binds per Fe, with binding energy 29 kJ/mol.[127]
ANINIT, Siesta VdW-DFT, TM pseudopotential	Various MOFs with Ni, Cu, Mn, Zn	Induced dipole depends on the binding site. H_2 IR shift depend on surrounding environment.[77]
PWscf (Quantum Expreso), USPP	HKUST-1	Coulomb interaction is dominant and unscreened in MOF with open metal site. H_2 orientation has large effect on H_2 binding potential.[106]
DMOL, DFT-PBE	$Cu_3(btc)_2$	Derived Cu-H_2 potential parameters for unsaturated Cu site, improved prediction in sorption.[128]
VASP-PAW	MOF-5-Li	Li increase interaction energy 12-18 kJ/mole. [79]

Table 2.2 Continued

Method	System	Findings
VASP(LDA, GGA) PW-91, PBE	Zn MOF, Cd-MOF5	LDA gives 4-8 times higher value than GGA. Cd MOF has higher binding energy.[129]
VASP-PAW potential	MOF-5	Adsorption of hydrogen on the pore walls creates attractive potential at the center of the pore.[69]
DMOL in Materials Studio, PW-91, PBE	MOF-5	Pairing effect observed, that allows more H_2 to bind.[130]
VASP, LDA with USPP	IRMOF-1 –M(Be, Mg, Ca, Zn, Cd)	Band gap can be tuned by varying the metal, and doping Al, Li. Al doping can create MOF with metallic property.[131]
DFT-PBE exchange corelation function in Turbomole	IRMOF-14-SO_3Li	Average binding energy 1.6 kcal/mole and 6 H_2 molecule on each linker.[72]
DFT in SIESTA code. Troullier-Martins pseudopotentials	MOF-5	Calculated density of states and mechanical property. MOF is a soft and ductile material.[38]
DFT-LDA with PAW method in VASP code.	MOF-5	Calculated density of states, band gap 2.7 ev. Metal site gives stronger interaction than linker.[39]
DFT-LDA with ultrasoft pseudopotentials, in VASP	MOF-5	Calculated elastic moduli and shear moduli. MOF-5 is close to structural instability and will give to new phase under high pressure.[40]
LDA and GGA in VASP code	MOF-5	Calculated bulk modulus and elastic constants compared with nanoindentation experiment.[41]

DFT calculation can be performed on fully periodic structure and it can predict mechanical property, thermal conductivity, etc. Interaction energy resulting from DFT is calculated at absolute zero temperature, so temperature correction may be required.

2.7.2.1 Pseudopotentials for DFT calculations

DFT calculations are carried out using pseudopotential model (interaction energy potential model) instead of actual potential models to simplify calculations and to reduce computations. A

pseudopotential approach replaces the electron density function for a chosen set of core electrons with a smoothed density function chosen to match various important physical and mathematical parameters. Pseudopotentials have been introduced to avoid the need to explicitly consider the core electrons which are strongly bound to the nucleus and therefore chemically inert.[132] This is called frozen core approximation. The pseudopotential approach requires energy cut off that should be used in calculation involving that particular atom. Depending on the cut off energy the pseudopotential may be hard or soft. The pseudopotentials that require high cut off energy are called hard and those requiring low cut off are soft and these are computationally more efficient. Pseudopotenials may be norm conserving where the node-less pseudo wave function ensures that not only the logarithmic derivative of the exact and pseudo wave functions but also their derivative w.r.t energy agree at the chosen reference energy and cut off radius. Whereas norm conserving criteria is used for ultrasoft pseudo potential, but the logarithmic derivatives are matched at two or more reference energies.[132] The most widely used pseudopotentials are Vanderbuild type and these require very low energy cut off and are called ultrasoft pseudopotentials (USPP). But this requires lots of empirical parameters to be specified. The quality of a pseudopotential depends on how well it represents the results of an all electron model. There are certain drawbacks of a pseudopotential, due to the non linearity of the exchange interaction between the valence and core electrons. Elaborate non linear core corrections are required where the overlap between valence and core electrons is not negligible. In order to overcome this deficiency, another frozen core approach, projector augmented wave method (PAW) is developed. In materials with strong magnetic moment, or with atoms that have large difference in electronegativity, the PAW approach gives more reliable result than USPP. In DFT calculations involving adsorbate, we can use of different pseudopotentials, like Vanderbuild USSP, Troullier-Martin pseudopotential, PAW pseudopotential.

2.7.2.2 Dispersion DFT

As mentioned before, calculating van der Waals interaction in DFT is a challenge. Some works have been done to include dispersive interaction with the DFT calculation, but these are not well established yet. A detailed study of the metal-dihydrogen interaction using dispersion corrected method or wave function based methods can provide insight about the nature of interactions, whether it is dominated by electrostatic interaction or dominated by induced polarization, or actual orbital contribution is important.[128] Dispersive interaction may be accounted in two ways[101] : 1) using an efficient non local functional, called vdW-DF, where dispersion is calculated self consistently and it depends on the unique electron density on each atoms. 2) Dispersive interaction may be accounted as empirical function having C_6R^{-6} term in DFT-D method. Some researchers[127] have added an ad hoc potential energy of 4.8 kJ/mole to account for vdW dispersion effect.

2.7.3   Forcefield based simulation

Output from QM and DFT calculation may be used to develop forcefield. In order to calculate material property in the molecular level forcefield based simulation is performed. A forcefield is a mathematical expression that represents the type and nature of different bonding present in a molecular system based on the atomic coordinates. Sometimes generic forcefield like UFF, DREIDING, OPLS-AA, CVFF are used, and sometimes FF are developed based on first principle calculations. A correct forcefield requires correct charges on the atoms and proper representation of bonds, angles, dihedral, and nonbonded interaction which are obtained from quantum mechanical calculation.

2.7.3.1 Charge calculation

The charge on the framework atoms have significant effect in calculating proper binding energy, binding site and adsorption capacity. Moreover, charge quadrupole interaction has a significant effect on hydrogen sorption.[126] Molecular polarity is usually calculated by charge build up or depletion in individual atoms. Atomic interaction is based on atom centered charge-charge interaction, so assigning partial charge on the atoms is very important. There is no best method for assigning partial charges, as partial atomic charges are used in different ways in different calculations in chemistry. Various schemes are available like: Milliken, Bader, electrostatic potential (ESP) fit by Merz-Kollman sampling scheme, etc. The most widely used algorithm for charge calculation in Gaussian is ChelpG. Charge in adsorbate is calculated by cluster method to find a full periodic charge. It was found that charge from Bader charge calculation is inconsistent with charge from ChelpG method.[126] These Bader charges give adsorption isotherms which are not consistent with experimental findings. Thus discrepancy in charge calculation is an artifact of Bader method.

A method to calculate framework charges by connectivity based atom contribution method (CBAC) had been developed.[133] This method assumes that the atoms with same bonding connectivity have identical charges in different adsorbates. This is an approximate method similar to the well known group contribution method of thermodynamic property estimation in liquid. The results for 43 MOFs including a training set of 30 MOFs and test set of 13 MOFs shows that the CBAC charges are similar to the charges calculated from QM calculation. This method may be used for large scale computer screening of MOFs for several applications.

2.7.3.2 Forcefield development

An accurate forcefield is essential for correct prediction of MOF property and rational design of MOF materials by theoretical approach such as molecular dynamics, Monte Carlo simulation. Development of forcefield is rather slow for MOF due to its complex chemical nature, wide diversity in chemical structure and composition, scarcity of available experimental data to validate the forcefield.[134] The development of forcefield focuses on certain aspect such as: 1) capturing lattice flexibility correctly; 2) assessing the effect of unsaturated metal site on H_2 adsorption.

Conformational flexibility of MOF is one key aspect of these structures and in case of guest molecule adsorption this leads to 'breathing effect', 'gate opening' effect, with strong hysteresis on the adsorption isotherm. Keeping the framework rigid may not be a good strategy at low loading, when host-guest molecule interaction is predominant and that can create some framework deformation. Also keeping the framework flexible is required in case of large molecules to monitor its passage from one pore to another. Flexible forcefields have been developed for MOF-5 and IRMOF series[135] HKUST-1[136,137] and also for MIL-53[102] to describe the breathing effect. Here the shrinking and expansion of the unit cell with guest adsorption and desorption is modeled. Flexibility may be imparted in the energy equation by incorporating various interconnected or cross terms involving coupling between bond-angle, angle –torsion, etc.

2.7.3.3 Accounting for unsaturated metal sites

MOFs with unsaturated metal center require extra care in calculating and modeling interaction potential. Generic forcefield based GCMC predicts the adsorption capacity consistent with the

experimental result but for, MOFs with unsaturated metal center the adsorption capacity is underestimated at low pressure. Inclusion of charge quadrupole interaction (CQI) does not improve the interaction. Thus this requires some extra parameterization to account for unsaturated metal site. Fischer et al[128] derived a new potential parameter based on ab initio calculation of metal dihydrogen system which was applied on Cu based MOF, PCN-12 and HKUST-1 [$Cu_3(BTC)_2$]. In this case Hydrogen was modeled as a single sphere. Lennard-Jones (LJ) potential was used for all fluid-fluid interactions, and fluid-solid interaction.

The interaction between the hydrogen and open metal sites were modeled by the following potential with an extra stiffness parameter:

$$U_{IJ} = D_0 (\exp[\alpha(1 - \frac{r_0}{r_{ij}})] - 2\exp[\frac{\alpha}{2}(1 - \frac{r_0}{r_{ij}})]) \qquad (2.2)$$

The parameters r_0 and D_0 has the same meaning at the LJ potential, but the stiffness parameter α adds additional flexibility, and permits fitting to the abinitio energies. The additional parameter gave excellent prediction for low temperature H_2 sorption in PCN-12 containing unsaturated Cu sites.

2.7.3.4 Charge quadruple interaction

Quadrupole-quadrupole interaction and quadrupole-framework interactions may play a significant role at low temperature hydrogen binding, although it may be negligible at room temperature. Thus an accurate forcefield should include this charge quadrupole interaction (CQI). Charge quadruple interaction in HKUST-1 and hydrogen molecule for equilibrium adsorption properties and self and transport diffusivities has been studied.[126] The interaction

potential of hydrogen molecule with the framework was calculated as a summation of van der Waals and CQI as given below.

$$u_i = \sum_{j=1}^{N} (\phi_{ij} + u_{q_j} \Theta) \qquad (2.3)$$

Charge quadrupole interaction was calculated by two different methods: In the first method a point quadrupole moment on the hydrogen molecule was used. In the second method, CQI used three point charges to represent quadrupole moment of hydrogen. The H-H bond length was set at 0.74 Å and charge of each hydrogen atom as +0.468e and on a charge of -0.936e at the center of mass of hydrogen atoms. CQI has substantial effect at 77 K but both adsorption and diffusion is unaffected by CQI at 298 K.

The most commonly used forcefields like UFF and DREIDING forcefield usually gives similar results.[103] Universal forcefield (UFF) does an underestimation of hydrogen uptake at low pressure the difference being ~1% between simulation and experiment when unsaturated metal site is present.[128] But at high pressure the UFF forcefield matches the experimental value very well and Morse potential overestimates this by 0.4%-0.8%. Hydrogen adsorption at higher temperature (298 K) is similar for UFF and Morse potential. Unmodified UFF gives better agreement with the experimental result at high pressure at different thermal condition, thus it seems to be the best choice at high pressure.

2.7.4   *Theories to model properties of hydrogen*

To appreciate the challenges of hydrogen storage, it is important to discuss the properties of hydrogen. Hydrogen molecule can be found in various phases depending on temperature and

pressure. At low temperature, hydrogen is solid having density 70.6 kg/m^3 at 11 K. It is a gas at high temperature with density 0.089886 kg/m^3 at 273 K. There is a small zone between triple point (21.2 K) and critical point (33 K) where liquid hydrogen exists with density 70.8 kg/m^3 at 20 K.[138] One kg of hydrogen at ambient temperature and pressure occupies a large volume of 11 m^3.

Hydrogen molecules are IR inactive and exist in two isomers with different nuclear spins. Para H2 is characterized by a nuclear singlet state and ortho H$_2$ is a triplet state. The two states have different rotational transitions, thus gives distinguishable IR frequencies. The transition from v=0 to v=1 for para Q(0) and ortho Q(1) states are at 4161 and 4155 cm^{-1}.[128] Hydrogen is very light; the zero-point vibrational energy (hv/2) is significant (272 meV for free H$_2$ molecule).[41] But Raman spectra of free and adsorbed H2 on carbon nanotube showed that the shift in H-H stretch frequency is of the order of 1 cm-1 (0.1 mev), thus this energy may be neglected for adsorption calculation. However the center of mass zero point vibration can give non-negligible contribution of Δh and may lead to a significant part of adsorption energy (Eads).[121] To obtain more accurate result thus zero point energy has to be taken into consideration, although for initial screening purpose this may not be necessary.

2.7.4.1 Hydrogen potentials

Accurate prediction of hydrogen storage capacity depends on employing a correct hydrogen potential. H$_2$-H$_2$ dimmer interaction is attractive but very weak, with experimental isotopic well depth -32 to -35K. So the modeled potential energy surface (PES) must be very accurate.[139] Most of the current potentials are isotropic. Buch potential[140] is easily transferable and is good to predict H$_2$ uptake in weakly interacting material. Hydrogen modeled by classical Buch potential

gave better agreement with experimental result.[141] Silvera Goldman[142] potential is good to predict bulk and condensed phase property but it is too attractive. But these are good for materials where only weakly dispersive force is prevalent.

In order to capture adsorption in heterogeneous materials like MOF and also to learn the behavior at high H_2 density, anisotropic many body effect has to be considered for H_2 potential. Most widely used potential is that of Darkrim and Levesque (DL),[143] which treats hydrogen as a rigid, diatomic molecule, with the H−H distance fixed at 0.74 Å. This potential consists of a LJ core placed at the center of mass of the molecule, having point charges of magnitude $q = 0.468|e|$ at the position of the two protons, and a charge of magnitude $-2q$ at the center of mass. This is too attractive and not suitable for charged system.[136] Anisotropic potentials like Diep and Johnson[139] is focused on neat H_2 and they require parameterization to apply to a chemically different environment. . In heterogeneous environment where electrostatic, dipole, quadrupole interaction is present these potential treats them in a mean field fashion which may lack accuracy of the result.[144]

An ad hoc inter-atomic potential has been developed for hydrogen.[120] The researchers used a repulsive core for H_2-H_2 interaction to avoid hydrogen clumping. They modified the potential with exponential term as:

$$U = D_0 \exp[y(1 - \frac{R}{R_0})]$$ (2.4)

where D_0=1.42 KJ/mole, y =12, Ro=3.10 Å.

H_2 has also been modeled at united atom model where the diatomic molecule is represented as a single sphere.[128] H_2 retains its rotational degrees of freedom when adsorbed in MOF thus use of this united atom model can give acceptable results.

Isotropic many-body hydrogen potential has been derived from first principle calculation.[144] The functional form is suitable for mixing with heterogeneous systems consisting of partial charges, Lennard-Jones sites, and atomic point polarizabilities. The potential can reproduce the properties of bulk hydrogen under different conditions of current interest in materials research such as high pressure, and high bulk density. Electrostatic quadrupolar and many-body polarization interactions are included anisotropically, thus making this model useful for high-density studies where orientation-dependence is of interest.

Although a correct forcefield is available, some correction to the interaction potential may be required depending on low temperature operation, small size of the adsorbate molecule, high loading, etc.

2.7.5   Quantum correction to classical simulations

H_2 is a light molecules, thus quantum diffraction effects can be important which may lead to significant differences in the thermodynamic properties compared with those for corresponding classical fluids.[145] Quantum diffraction is explained as follows. The position and momentum of a particle can be specified precisely by classical mechanics and thus ground state of a solid is a perfectly rigid crystal (motionless particles). But in reality Heisenberg uncertainty principle forbids such perfect rigid crystal. Even at T=0, the zero point motion of the particles creates 'smear out' nature around the lattice point.[146] The delocalization effect increase with reduction in particle mass and thus this effect is more pronounced in case of lighter atoms like hydrogen.

Different schemes have been developed to account for this effect and one of them is Path Integral Monte Carlo (PIMC) and the other is Fennman-Hibbs effective potential. Path Integral Monte Carlo (PIMC) method is an exact method but computationally costly, whereas Feynman−Hibbs effective potential method is much more computationally efficient.

Fennman-Hibbs effective potential has the following form.[128] It adds a temperature dependent term to the potential.

$$U_{FH}(r) = U_0(r) + (\frac{\hbar^2}{24\mu k_B T})\nabla^2 U_0(r)$$
(2.5)

where the Laplacian is :

$$\nabla^2 U_0(r) = U_0^{''}(r) + (\frac{2}{r})U_0^{'}(r)$$
(2.6)

and U_0 is the uncorrected potential, μ is the reduced mass and other parameters have their regular meaning.

FH effective potential using Buch potential for H_2 becomes: [145]

$$\nabla^2 U_0(r) = 4\varepsilon(\frac{132\sigma^{12}}{r^{14}} - \frac{30\sigma^6}{r^8})$$
(2.7)

This works well for cryogenic temperature but over predicts the importance of quantum effect at room temperature, although the overestimation is negligible. Fig. 2.13[145] below compares results of H_2 sorption using quantum correction and without correction.
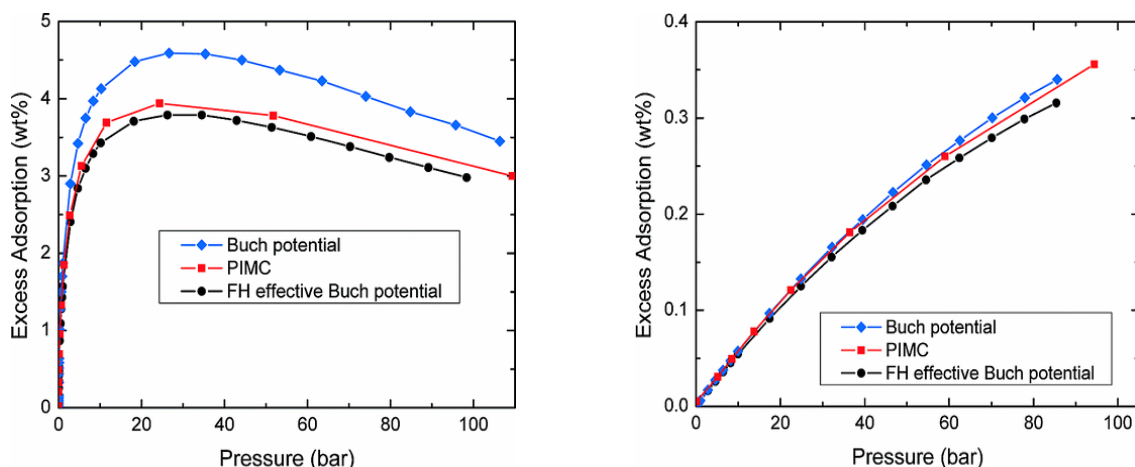
Fig. 2.13 Comparison of simulated H$_2$ adsorption isotherms in CuBTC at 77K and 298K[145]
(Reproduced with permission from ref. 145, copyright (2007) American Chemical Society)

As observed FH and PIMC simulations are in good agreement at both low and high temperature. The FH effective Buch potential appears to overestimate the importance of quantum effects; leading to ~4% reduction in the amount of H$_2$ adsorbed relative to the PIMC simulations. But FH approach was used in calculations to compare with experiments because of the significant computational savings of the FH method over the PIMC method.[145]

FH formalism at high temperature is not recommended because it overestimates quantum effects at these conditions. As observed from the above graph, for H$_2$ adsorption in CuBTC at 298 K, the difference in excess adsorption between the FH and classical Buch potential is ~7% at 85 bar, but the difference between the classical and PIMC results is only ~2% at 85 bar. Thus even at 298 K there is even a 2% difference between classical and quantum isotherms. Thus quantum effects are nonzero at 298 K, because at this temperature, the thermal de Broglie wavelength of a hydrogen molecule is still a sizable fraction of the hard-core diameter. Quantum diffraction is also enhanced at high densities because the molecules are more localized.

Using these parameterized forcefields atomistic Molecular Dynamic simulation and probabilistic Monte Carlo simulation can be performed on adsorbate systems. We will discuss these in the following paragraphs.

2.7.6   Monte Carlo simulation

The most widely used simulation to study H_2 sorption in MOF is Grand Canonical Monte Carlo (GCMC) simulation.[146-148] Monte Carlo importance sampling technique is a stochastic method. In grand canonical Monte Carlo simulation, the chemical potential μ, volume V and temperature T are fixed. This represents a system that can exchange particle and energy with a big reservoir. The initial configuration has certain energy. The sorbate molecule is placed at an arbitrary position in the framework and energy is calculated again. Subsequent configurations are generated by random translation or rotation of the sorbate molecule. Configurations are accepted or rejected based on the configurational energy change (ΔE) and the probability given by:

$$P = \min(1 : e^{-\Delta E / KT})$$
(2.8)

If ΔE is -ve, new configuration is accepted. If ΔE is +ve, Boltzmann factor exp(-ΔE/kT) is compared to a random number between 0 to 1. If the Boltzmann factor is greater, the move is selected; otherwise it is rejected. Monte Carlo simulation has been used widely to understand sorption behavior in adsorbate structure and the related isosteric heat. It is computationally less expensive and predicts accurate result often comparable with experiment.

There are other Monte Carlo simulations performed on MOFs. For example, some researchers[149] performed a Canonical NVT Monte Carlo simulation including many body polarization effect. Total potential energy of the system was described as:

$$U = U_{electrostatic} + U_{polarization} + U_{vdW} \qquad (2.9)$$

The simulation was performed in a charged MOF containing Indium ion and dipole fluctuation was recorded. The integration of the dipole autocorrelation function gave hydrogen population inside the MOF.

Table 2.3 below gives some examples of the GCMC simulations and the findings from them.

Table 2.3   Examples of Monte Carlo simulation

Method	System	Findings
GCMC with UFF	MOF-5	High energy binding sites at the corner, form cluster at 77K.[120]
GCMC with OPLS-AA forcefield	IRMOF-1, IRMOF-8, IRMOF-18,	H_2 uptake at 77 K, 1 bar was similar to the experiment.[150]
GCMC with UFF and Dreiding	MOF-2, MOF-3, IRMOF-1, IRMOF-6, IRMOF-8, IRMOF-18,	Quantum correction with Buch potential gives better agreement with experiment.[145]
GCMC with Dreiding	Several MOFs	Several regimes identified for hydrogen sorption in MOF.[59]
GCMC with UFF with quantum correction	Zn(bdc)(ted)0.5, Cu-BTC	Quantum effect leads to low loading and high self diffusivity.[103]
Ab initio parameterized forcefield	$Cu_3(BTC)_2$	Newly derived Cu potential improved sorption prediction.[128]
Abinitio parameterized FF	IRMOF-8, 14 with alkoxide linker	Gravimetric capacity upto 10 wt% at 77 K.[70]
X3LYP parameterized FF	Hexagonal MOF	IRMOF-2-60 best, with capacity 6.5 wt % 243 K, 100 bar.[151]
Music code	Fe-IRMOF-16	6 wt% at 298 K 100 atm.[127]
NVT –MC with polarization	Soc-MOF-(Indium metal)	Polarization effect enhances hydrogen adsorption.[149]
GCMC in materials Studio.	PCN-12-Si	Excellent H_2 sorption capacity.[152]

2.7.7   Molecular dynamics

Molecular dynamics can give us information about diffusion, phase transition at different external condition like temperature or pressure, negative thermal expansion, etc. for a MOF system. Molecular dynamics is a technique to compute the equilibrium and transport properties of classical many-body system, which obeys classical mechanics.

Table 2.4   Examples of Molecular Dynamic simulations

Method	System	Findings
MD using OPLS-AA forcefield	IRMOF-1, IRMOF-8, IRMOF-18,	Steric hindrance for diffusion due to pendant CH3 group.[150]
MD, UFF, Dreiding	Zn(bdc)(ted)0.5	Quantum effect increase sorption at low loading.[103]
MD- empirically derived FF	MIL-47(V), MIL-53(Cr)	Hydrogen super mobility observed.[106]
MD empirically derived FF	HKUST-1	CQI included. At low loading diffusion is limited to the pore size.[126]
Abinitio MD in VASP	MOF-5 with Li	High H_2 capacity 2.9 wt% at 200 K.[79]
Abinitio MD in VASP	MOF-5	H_2 concentration at the center of the pore is high. [69]
GULP- new FF	MOF-5	Thermal conductivity calculated.[112]
MD using CVFF	MOF-5, pure and hydrated form	Water content at 8% result non reversible decomposition.[153]

MD simulations are like real experiment, where we prepare a sample, connect to the measuring deices and measure the property of interest. Similarly in MD simulation we prepare a sample, which is select a model system having N particles and solve Newton's equation of motion, until the properties of the system does not charge with time meaning the system reaches equilibrium. Then we perform the real measurement. To measure an observable of the system, we must be able to express the observable in terms of particle coordinates and momenta. MD simulations

may be used to study structure prediction and phase transition. Table 2.4 presents some examples of MD simulations in MOF system.

2.8 Li ion battery: Applications and challenges

2.8.1 Potential of Li ion batteries

Rechargeable Li ion batteries are key power source for new generation hybrid electric vehicle (HEV), portable devices, mobile phones, computers, laptops, camera, etc.[154,155] Fig. 2.14[156] below shows system level performance of three battery chemistries, capacitors, fuel cell, and internal combustion engines based on specific power, specific energy and discharge rates. The diagonal lines are discharge rate with long discharge time in the upper left. This demonstrates that high discharge rate, less power can be extracted, due to increased resistance in the cell. For transportation sector we need battery technologies that give high energy storage density, capacity and power delivery. From this figure it is evident that Li-ion battery can meet the goal for hybrid and plug in hybrid electric vehicle as set by DOE.
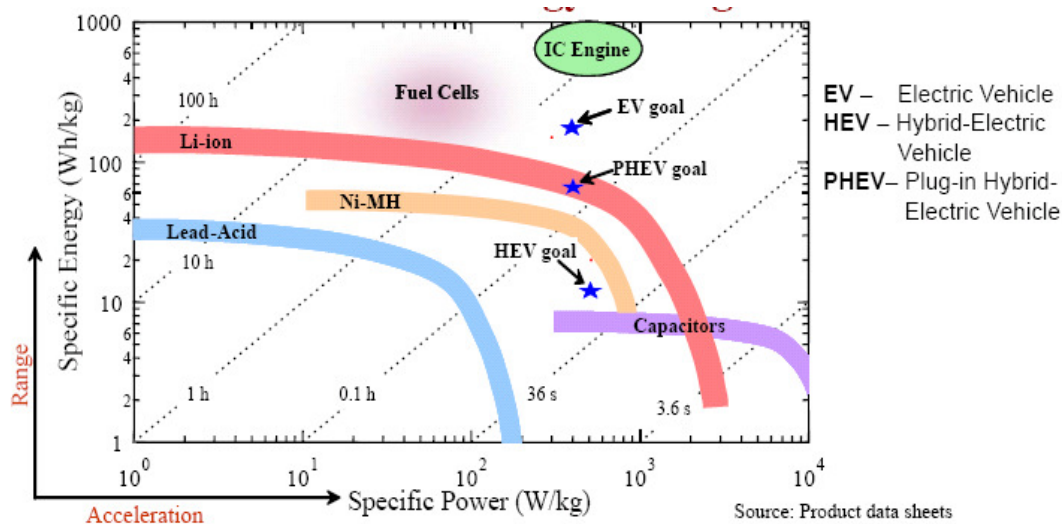
Fig. 2.14 Comparison of various energy storage options [156]

2.8.2   Li ion battery chemistry

During the past decades there has been development in chemistry and engineering of Li ion battery technology. A Li ion battery is made up of electrochemical cell containing a positive and negative electrode separated by an electrolyte solution that helps in ion transport (Fig. 2.15[157]). When the electrodes are connected externally, chemical reaction produces electrons and generate current.
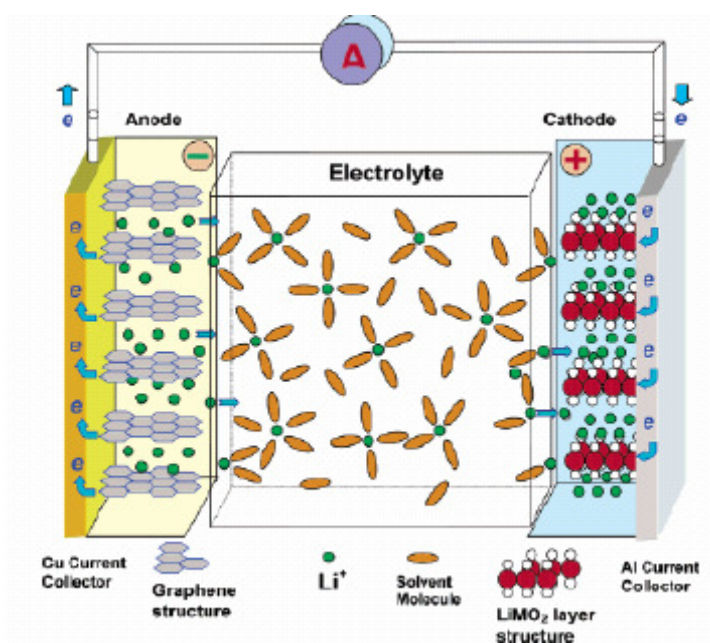
Fig. 2.15   General structure of Li ion battery [157]

The dominant lithium–ion chemistry involves lithium intercalation at each electrode. Intercalation reaction involves reversible insertion and extraction of an atom into a crystal without changing the crystal lattice of the host material.[156] At positive electrode the reaction for $LiCoO_2$ is :

$$Li^+ + e^- + CoO_2 \leftrightarrow LiCoO_2$$
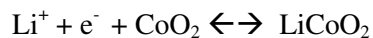
In negative electrode (for graphite) it is :

$$Li^+ + e^- + C_6 \longleftrightarrow LiC_6$$

The amount of electrical energy that can be stored in the battery is expressed either as per weight basis (W.h.kg^{-1}) or per volume (W.h.l^{-1}) basis. This stored energy is a function of the cell potential (V) and capacity (A h.kg^{-1}), which are linked directly to the chemistry of the electrode materials. Li is the most electropositive material (3.04 V versus standard H_2 electrode) and the lightest metal. Therefore Li ion battery has high energy storage density and capcity. Li ion battery chemistry also provides design flexibility and in addition it outperforms other battery technologies (Fig. 2.16).[154]
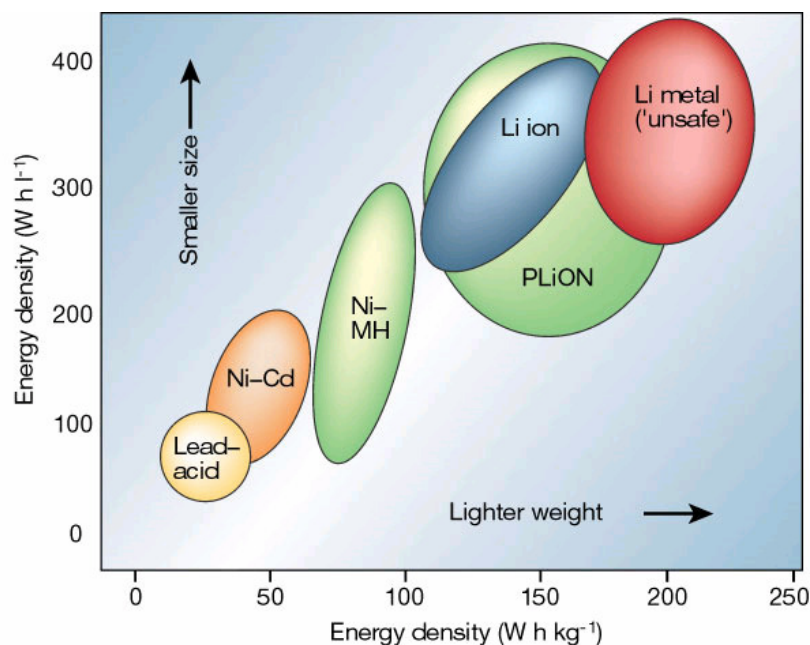
Fig. 2.16 Comparison of different battery technology [154]
(Reproduced with permission from ref.154, copyright (2001) Nature, Macmillan Publishers Ltd.)

2.8.3   Technical challenges and key design factors

During the initial stage of battery development, problem of Li growth (dendrite formation) during each discharge-recharge cycle was observed. Li metal was replaced with alloy, which solved the dendrite problem, but the battery survived only a limited number of cycles. Organic electrolyte can cause graphite exfoliation and result in fire hazards.[155]

In all these cases, the battery life and performance depends on the materials used in making the battery and the nature of interfaces between the electrode and electrolyte. Li ion battery's energy density can be improved by appropriate selection of electrolyte and electrode materials. On the other hand battery life and capacity depends on the structure and electronic property of the electrodes. This is because unwanted side reactions can reduce battery life and capacity. Therefore the chemical stability of the electrode material in the electrolyte is an important factor.

2.9   Ionic liquids

Ionic Liquids (IL) are solvents with many interesting properties such as: nonvolatility, good solvation and coordination property, low hydroscopicity, nonflamability, wide electrochemical window, high ion conductivity, wide liquid range, etc. [158] Therefore ILs have possible application in catalysis, batteries, fuel cell and solar photovoltaics. Even though ionic liquids were first identified more than a century ago, but their applications were limited to certain electrochemical reactions. Currently, more than 1000 ILs have been synthesized and these ILs are showing potential as solvent in electrodeposition, metal processing, environmental friendly reaction, extraction media, etc. The modern day ionic liquid are based on ions which are 'neutral' as they remain in positive-negative ion pairs and are unreactive towards acids or bases. Some reactions involving water sensitive metals and semiconductors can be easily carried out in IL solvents. As

a result, a lot of chemical reactions such as semiconductor electrodeposition, preparation of metal nanowires are conducted in these ILs. These are also called 'green solvents'.[43] They have negligible vapor pressure, thus the loss into the environment due to evaporation is minimal and they can be recycled indefinitely. Most products prepared in IL can be distilled off or extracted using water or organic solvents. This unique solvent property has made ILs solvent of choice for many emerging technologies.

2.10   Ionic liquid in Li ion battery application

2.10.1 Role of ionic liquids

ILs have the potential to be used as alternative electrolytes in lithium batteries as these are expected to improve the performance of these devices and avoid fire hazards. Traditional Li ion battery electrolytes are based on carbonate solvents mixed with Li salt to increase their condustivity.[159] These solvents are volatile and they easily catch fire if the temperature in the battery increases during operations due to exothermic 'graphite exfoliation' reaction. Therefore there is a concern about safety when such electrolytes are used. Whereas, ILs have negligible vapor pressure, pose no fire risk, and can be mixed with required concentration of lithium salt. Thermal stability of the ionic liquid based electrolytes are better and this thermal stability may be further increased by mixing a solid Li salt in ionic liquids.[159] Therefore ILs may improve the safety factor when used as alternative solvents in the battery electrolyte. However, to enable application of ILs in Li ion batteries, we need to understand several aspects about ionic liquids. Therefore, here we will discuss the current state of research on ionic liquid with a focus on application in Li ion batteries.

2.10.2   Li ion batteries with ionic liquids

Ionic liquid based battery electrolytes typically consists of a cation of quarternary ammonium, imidazolium, or pyrrolidinium and with a non coordinating anion. They show a broad electrochemical stability window, generally more than 4V.[160] Within this voltage window the electrodes and electrolytes do not have any unwanted side reactions that decompose either of them. There are examples of Li ion batteries that had used ionic liquids as electrolytes. Li/LiMn$_2$O$_4$ based battery prepared with 1,2 dimethyl-4-fluoropyrazolium tetrafluoroborate with LiBF$_4$ or LiAsF$_6$ ionic liquid. Another battery, consisting of Li/LiCoO$_2$ with n-PrMePipNTf2 (Pip=Piperidinium), also showed good cyclic efficiency. IL based on these NTF$_2^-$ anion gave good anode stability.

2.10.3   Challenges and approaches in using ionic liquids

However there are some challenges in using ionic liquid as electrolytes. One of the problems is that the Li metal (anode material) is incompatible with ILs. There are possibilities of unwanted reactions between the IL and the anode, which decompose the IL. In some electrochemical batteries this unwanted reactions some times do not proceed once a Solid-Electrolyte-Interface (SEI) is formed at the electrodes. SEI is an inert layer that is formed by initial reaction between the electrolyte and the electrode, which stops further reactions. Based on research carried out in past few years, we now know the mechanism of solid electrolyte interface (SEI) formation on negative electrode (anode). But the composition and nature of the SEI is still under controversy. For carbonate solvent based Li ion batteries, spectroscopic investigation showed that the SEI consists of electrolyte decomposition product such as Li$_2$CO$_3$ or LiF decomposition of LiPF$_6$. The SEI may extend upto 2 nm to several tens of nanometer.[160] It allows Li ion transport to

enable the electrochemical process for battery operation. More importantly, it helps electrode stability by preventing further corrosion of the electrode by the electrolyte.

However in Li ion batteries, the SEI that is formed during the charge-discharge process, is less stable. This limits the cycle efficiency of the battery.[160] Therefore understanding the SEI formation in IL based batteries and its composition is important as it can help to predict its stability. Moreover, in some situations this SEI might not even form.[161] Initial report on QA-NTf$_2$ ionic liquid based Li ion battery revealed that the SEI formation was mainly due to presence of NTf$_2$ anion. When the IL was ultra pure, in absence of O$_2$ or H$_2$O, there was no SEI formation. This means that we may have to think of batteries without SEI layer. Actually battery without a SEI may be a good idea, as it's absence can result in increased conductance at the electrolyte interface which can help to reduce battery impedence.

An alternate avenue of exploration would be how to create a good quality SEI. For example, molecular additives such as acrylonitrile, ethylene sulphide or vinyl carbonate in ILs may help to form SEI.[159] Another approach may be to modify ILs to incorporate functionality that induce SEI formation. For example, cyano group functionality in ILs was found to be effective to form SEI.[159]

Understanding the positive electrode (cathode) surface is also important because at high voltage it can drive catalytic decomposition of the electrolyte. Sometimes a coating is used to encapsulate electrode grains. However the coating must allow electron to tunnel through.[154]

Cathode materials are of spinal type, for example Li(M)$_2$O$_4$ - LiFePO$_4$, LiCoO$_2$. LiFePO$_4$ has good thermal stability, low fabrication cost, non toxicity, flat voltage –time discharge profile, it

has the potential to replace the most used cathode material, $LiCoO_2$. However, $LiFePO_4$ suffers from low electron transfer, and low lithium diffusivity leading to high charge transfer resistance. This may be overcome by coating $LiFePO_4$ with porous carbon material that will increase Li^+ diffusion to the electrolyte. Proper choice of electrode materials that have smaller particle size may also increase Li diffusion.[162] Metallic lithium has very high energy density (3860 mAh/gm), which is a good cathode material. But formation of dendrite at the electrolyte/electrode interface is a problem with traditional electrolytes.[159] Use of ILs are expected to avoid this.

The number of possible charging discharging cycles is one of the important parameter of Li ion battery. Batteries with traditional electrolytes show 500 to 1000 cycle life, whereas IL containing batteries shows 10 to 100 cycles of life time.[159] A $LiCoO_2$ cathode in imidazolium based IL $[Li^+][Me_2PrIm^+][NTF_2^-]$ showed high charge/discharge reversibility for more than 100 cycles without SEI formation.

Performance of cathode at higher current density depends on ionic liquid viscosity and conductivity. Cell impedance will become more pronounced at low temperature in case of battery with ILs since ILs have higher viscosity and diffusivity which will hinder Li ion transport.[163] However some ILs like imidazolium based ones perform better in this respect.

In some situations, use of IL had reduced energy storage capacity and cell output voltage with temperature variation.[159] Graphitized carbon materials also have problems of Li intercalation and deintercalation when quartenary ammonium (QA) and EMI imide ionic liquids are used. They will need additives for proper functioning. In addition, side reaction such as cation intercalation leads to graphite exfoliation during first cycle. This can lead to poor cycle performance.[164]

In order to address all these challenges a lot of research is being undertaken by other researchers. However the studies reported in this dissertation will focus on the physical properties of an ionic liquid. We are specifically interested to know their properties when they are in the bulk liquid, in contact with the electrode surface and in nano confinement. Much of the understanding about these physical properties of ILs can come from experimental studies but theoretical studies involving molecular dynamics simulation is also an important part. Hence in the next section will present the simulation methods for investigating liquids followed by simulation on ILs with focus on Li battery applications.

2.11   Properties of ionic liquids

2.11.1 Comparisons of liquid ionic systems and nature of interactions

There are different types of liquid ionic systems: (1) molten salts; (2) ionic solutions; (3) liquid metals; and (4) ionic liquid.[165] Molten salts have large cohesive energy and high ionic conductivity. Some crystalline salts called 'solid electrolytes' also have high ionic conductivity compared to the molten salts. Ionic solutions are liquids made in solvent from neutral, polar molecule and a solute that dissociate into cations and anions which are of comparable size. Macromolecular ionic solution consists of macro ions, like charged polymer chain, charged colloidal particle and micelles. Liquid metals are similar in composition to molten salts, but instead of anion there are electrons. However, ionic liquids (ILs) are different from all these three.

The difference between 'Ionic Liquid' and 'Molten Salt' is that ILs exhibit liquidity at low temperature (below 100^0C). But the main difference is that ionic liquid contains organic cation as opposed to inorganic cation in case of molten salts. The ion–ion interaction in IL is relatively

weaker, compared to that of the molten salt.[165] ILs also have low melting point compared to Molten salts, which is due to increasing size of the anion or cation.

Coulombic interaction in these ionic liquids is also small compared to that of the inorganic salts. This is due to size and charge difference and presence of flexible constituents. These factors introduce charge separation, disruption in lattice isotropy, inefficiency in packing, and introduce rotational and vibrational modes causing low melting point in ILs. Increasing cation symmetry increases melting point due to increase in more efficient packing. The balance of large electrostatic interaction and strong coupling between large collections of ions is the general feature of an ionic liquid.[166]

In ionic liquid the particles carry charges. Columbic interaction between these particles, decay slowly and span longer distances. This gives rise to many distinguishing features in ionic liquids.[165] In comparison, in general fluids, the range of the interatomic Coulumbic forces are shorter, in the order of a few atomic radii.
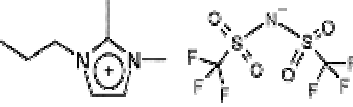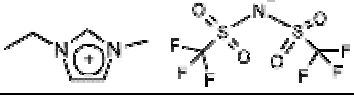
2.11.2 Types of ionic liquid systems

Ionic liquids are of three types based on how they attain the charge: (1) protic; (2) aprotic; and (3) zwitterionic. Protic IL are formed by proton-transfer reaction as acid and base, meaning they donate and accept hydrogen bonds making hydrogen bonded network like water.[167] Aprotic ILs consists of imidazolium and pyrrolidium based cations and form inter molecular hydrogen bonds but not as heavily networked as protic ILs.

Ionic liquid may be made up of pyridinium, imidazolium, quaternary ammonium, phosphonium, pyrrolidium and sulfonium cations.[168] Quaternary ammonium, phosphonium are investigated for

application in synthetic chemistry. Protic ILs are finding interest in hydrogen transport in fuel cell technology. Changing ion type, substitution and composition produces new ionic system, each with unique property. Toxicity of IL increased as alkyl chain length increased. [PF6]- anion is slightly more toxic compared to other anions. Table 2.5 presents some examples[169] of imidazole based ionic liquids along with their structures and names.

Table 2.5   Structures of some imidazole based ionic liquids

Name	Structure	Abbreviation
1-n-butyl-3-methylimidazolium tetrafluoroborate		[BMIM][BF4]
1-n-butyl-3-methylimidazolium hexafluorophosphate		[BMIM][PF6]
2,3-dimethyl-1-propylimidazolium bis(trifluoromethylsulfonyl)imide		[PMMIM][Tf2N]
1-n-ethyl-3-methylimidazolium bis(trifluoromethylsulfonyl)imide		[EMIM][Tf2N]

2.11.3 Structure

X-ray scattering, X-ray absorption, neutron diffraction and molecular dynamic simulations have been used to study ionic liquid structures. Imidazole based ionic liquids are the most studied ones. The general orientation of anion is near the carbon atom which is located between two nitrogen atoms in the imidazole ring of the cation.[170]   From abinitio calculation is has been observed that this carbon atom is most acidic in nature and the anion tends to bind to this site. The structure of the liquid changes depends on the length of the alkyl chain of the cation. As the alkyl chain length increases, nanodomains appear consisting of polar groups and separate non

polar groups. The polar groups consisting of the imidazole ring of the cation and the anion, forms an aggregate and the remaining spaces are filled by non polar alkyl chain. Thus ILs are heterogeneous in the nanoscale similar to the bicontinuoous microemulsion but in shorter length scale.[167] This liquid morphology is the reason behind its ability to dissolve unusual combinations of solute, distinctive performance over molecular liquid.[167]

Ionic liquid molecular structure is given by radial distribution function g(r). The ion coordination number is calculated from this function. The charge distribution function may be calculated from radial distribution function and cation-cation and anion-anion distribution functions ($g_{cc}(r)$ and $g_{aa}(r)$) are very similar in form and oscillates out of phase with the cation anion distribution function $g_{ac}(r)$. The charge –charge structure factor $S_{ZZ}(k)$ [($g_{11}(r)$ + $g_{22}(r)$ -2 $g_{12}(r)$)] gives very sharp peak in Fourier transform, whereas the number structure factor, $S_{NN}(k)$ [($g_{11}(r)$ + $g_{22}(r)$ +2 $g_{12}(r)$)]   is a structure less function. These results may be obtained from neutron scattering experiment.[165]

Structure and dynamics of [EMIM][NO_3] ionic liquid has been studied by MD simulation.[171] This study found that ions have long range local coordination and get arranged in a symmetrical structure. Compared to the neutral liquids, the local structure of IL is influenced by two phenomena: 'ion packing' and 'charge screening'. Packing of ions is determined by short range interaction and the volume of the ions. Whereas, charge screening phenomena is due to longer range columbic (electric field) interaction caused by presence of electric charge in the ions. The positive and negative charged ions get arranged in a particular order where they form alternate layers of positive and negative charged regions in shape of shells called 'coordination shells'. These alternate charged layers screen the electrical effect of any ion which is at the center. There is also a competition between packing and screening effect, which leads to charge ordering. The

measure of such screening effect is indicated by a unit named Debye. This Debye screening

length is the distance beyond which the electric potential due to an ion at the center is completely

screened by the local induced charge distribution. For example, the Debye screening length λ_D

for [EMIM][NO_3] was found to be ~7 Å, which indicates that the interaction between ions

decays very rapidly.[171] The radial distribution function also shows that the ions are strongly

correlated. Fluctuation of charge may give rise to high-frequency, collective modes similar to the

optic modes in ionic crystal and charge oscillation found in plasma.

2.11.4 Viscosity and density

Ionic liquids are mostly found to be Newtonian, meaning that the shear stress vs. strain curve is

linear and it passes through the origin. In general, ionic liquids are more viscous than most

common solvents and the range may be around 10 cP to 500 cP.[172] In comparison, the viscosities

of water, ethylene glycol and glycerol are 0.890, 16.1, and 934 cP at room temperature. Presence

of impurities and water influences the viscosity a lot. Presence of small amount of water, even as

low as 2 wt%, reduced the viscosity by 50% in case of [BMIM][BF4]. Larger cation size, larger

alkyl substations or presence of Li salt increases the viscosity. For battery application, high

viscosity creates certain problems. Highly viscous IL may not penetrate the porous electrode

materials and thus result in low battery capacity. Whereas, ionic liquid densities vary between

1.12 gm/cc to 2.4 gm/cc[169] and the density variation with temperature is very little.

2.11.5 Solvation property

Polarity is an important parameter to describe property of a solvent. Ionic liquids are considered

to be highly polar but weakly coordinating solvent.[173] Their polarity is between that of the water

and chlorinated organic solvents. Solubility of IL in water can be varied from completely

miscible to totally immiscible by changing the anion from Cl^- to PF_6^-. Solvent feature of ionic liquid comes from H-bond donation from cation, H-bond accepting functionality of the anion, and π-π bonding. ILs are immiscible to non polar organic solvents and can be used in two phase system.

Dielectric constant (ε_r) represents measure of polarity. Common solvents are considered as continuous dielectric media due to their structural homogeneity. But Ionic liquids are not continuous dielectric media as they have cations and anions which interact with each other to give rise to structural heretogeneity.[174] Microwave dielectric spectroscopy experiments indicated that the dielectric constant of some ILs varies between 9 to 15.[174] These values indicate that ILs are moderately polar solvents. Dielectric constant decreases as the length of the alkyl chain increases.

2.11.6 Ionic conductivity

Ionic liquids have several favorable properties such as high ionic conductivity that make them good solvent for electrochemical applications. They have desirable electrochemical window. This means that when the ionic liquid when used as battery electrolyte, the range of battery voltage over which the ionic liquid is stable and wide. For some ILs it is in the range of ~6V.[175] The potential window depends on the oxidative and reductive stability of the solvent or the resistance of the cation to reduction and the resistance of the anion to oxidation. The electrochemical window of 'dry' [BMIM][BF4] was 4.10 V whereas with 3 wt% of water, it was reduced to 1.95V. However choice of electrode has some effect on the electrochemical window. Ionic liquids with 4 coordinated nitrogen (ammonium, piperidinium, morpholinium) have larger electrochemical window compared to others.[175]

Ionic liquids have good transport property and electrical conductivity. The conductivity of a system is a measure of availability of charge carriers. These systems have overall neutral charge, and have mobile charge carriers. Ionic conductivity is measured by impedance bridge or by complex impedance method. In general, one might expect ionic liquids to have high conductivity, but that is not the case. Although they possess reasonably good ionic conductivity (~10 mS cm^{-1}) compared to best known non-aqueous solvent-electrolyte system, but they are less conductive than concentrated aqueous electrolytes. Room temperature conductivity of aprotic ILs range between 0.1 to 18 mS/cm. Conductivity at the level of 10 mS/cm is very common in ILs which have [EMIM] cations. The conductivity of such ILs are similar to that of carbonate based organic electrolytes.[175] Conductivity is lower due to ion pairing, lower availability of individual ions, and large ion size. Their conductivity often exhibits classical Arrhenius type relationship. The temperature dependence may be expressed by empirical Vogel-Fulcher-Tamann (VFT) equation. Variation of conductivity with temperature depends on complex interplay of short and long range forces. Presence of water impurity increases conductivity but this is due to decrease in viscosity due to presence of water. Ionic liquid conductivity is weakly correlated with ion size.

2.11.7 Microscopic dynamics

Behavior of ionic liquid as electrolyte depends on the transport properties of the ionic constituents. The transport properties depend on the rate and manner of individual ion or ion aggregate movement. The diffusion coefficient is a measure of the rate of movement of an ion in a solution whereas the transport number is a measure of the fraction of charge carried by an ion in the presence of an electric field.[175] Diffusion can be measured by electrochemical method or by NMR. Electrochemical method gives Fickian diffusion, (in the presence of a concentration

gradient) whereas NMR gives self –diffusion. Cation is found to be the majority charge carrier in ILs because it usually has higher diffusivity compared to anions.[175]

Much of these understandings come from molecular dynamic simulations. Ionic liquids behave like a supercooled liquid, with three regions in the ion diffusion trajectory. As observed from log plot of MSD vs time obtained from MD simulation, the dynamics show three different regimes. The first one, also called ballistic regime, is due to the inertial motion at the very short time scale, (<1ps) where $<\Delta r^2>$ (i.e. time average of Δr^2) varies quadratically with time. Then there is a diffusive regime occurs at long time (> 100 ps), where $<\Delta r^2>$ increases linearly with time and a subdiffusive regime in the intermediate zone, where $<\Delta r^2>$ proportional to t^α, where $\alpha <1$.[171] In the intermediate region the ions remain trapped in local cages by neighboring atoms, and need significant reorganization in the IL structure to move further. This is similar to the typical behavior of glass formers or in super cooled liquids.

The ILs exhibit significant dynamic heterogeneity, which means that different molecule have different rate of motion at different part of the liquid. Heterogeneity of translational dynamics is associated with non-Gaussian character of the self van Hove function,[166] This function is the time dependent probability distribution of the translational displacement. This function is given by the following equation.

$$\alpha(t) = \frac{1}{5}\frac{\left\langle \Delta x(t)^4 \right\rangle}{\left\langle \Delta x(t)^2 \right\rangle^2} - \frac{3}{5} \tag{2.10}$$

Heterogeneous dynamics of EMIM-NO$_3$ ionic liquid has been studied by MD simulation on two systems with 64 and 265 ion pairs.[176] It was found that the ion correlation increased with

decrease in temperature. It was found that some ions show short distance localized movement, whereas other ions that have higher energy, jumped over longer distances. At lower temperature the paths of these ions are intercepted by other ions and this reduced ion mobility. In IL and Li salt mixture, the Li^+ ions have very small probability of successful jumps as they are caged by other ions.

2.11.8 Behavior of ionic liquid on surface and in nanoconfinement

Understanding interfacial structure of ionic liquid is important because in applications like electrochemical cell, phase-separable catalysis, chemical extraction, solar cell and nanomaterial composites, the interfacial layer plays an important role. [177,178] Understanding the behavior of the microstructure and freezing process are also important in modeling properties like lubrication, adhesion, etc. In electrochemical application, electrochemical interface between ionic liquid and electrode (graphite) surface is important because, the operating efficiency of any electrochemical devices depends on the molecular ordering at the electrode/electrolyte interface and thus the compactness of the ion layer.[179] IL also comes in contact with grain boundary of electrode particles, thus understanding the behavior in nanoconfinement is also of a great interest.

The structure of ionic liquid in gas-liquid and solid-liquid interface has been investigated by many researchers by computational and experimental work. [158,177-195] These studies may be categorized in two ways: solid/liquid surface and liquid vapor surface. Graphite, silica and mica are most studied surfaces. Graphite is used as anode in Li ion batteries thus a lot of study focus on IL behavior on graphite surface. Graphite is considered as a model non charged surface, whereas mica is a representative negatively charged surface. Surface structure at the IL-surface interface has been studied by various experimental methods, like sum frequency generation,

surface tension measurement, IR, RAMAN spectroscopy, direct recoil spectroscopy, neutron reflectometry, X-ray reflectivity measurement, etc. Whereas computational methods like MD simulations have given us lot of insights about interfacial layering. The salient observations that emerged from these studies are: strong ion ordering or layering, oscillatory density and force profile, phase change, increase in viscosity, etc. These phenomena are triggered by the surface and confinement effects. These are discussed in the following paragraphs.

2.11.8.1 Phase change

Experimental study on [BMIM][PF6] on mica surface, by atomic force microscopy, indicated that ionic liquid remains in a solid phase near the surface.[194] Another study found that when this ionic liquid was confined in a multiwalled carbon nanotube, the liquids's melting point increased.[195] Liquid to solid phase transition for 1,3 dimethylimidazolium Chloride ionic liquid confined between two graphite walls was observed.[182] In general, reduction of liquid film thickness, fewer than 406 molecular layers, induced solidification. This may be compared with the anomalous phase behavior of water when confined in nanospaces. In this case, the liquid monolayer transforms into a solid layer. This is evident from the observation that the diffusion coefficient becomes zero when the distance between the surface walls is 0.8 nm.

In case of the 1,3 dimethylimidazolium Chloride ionic liquid on surface, the imidazole ring in the solid monolayer, remains planer to the surface. In this case each cation is surrounded by four nearest neighbor anions and each anion is surrounded by 4 cations. This monolayer has a 2D structure. In this ionic liquid, the imidazole ring is not always planar, and most probably the distribution of anion around cation is a 3D structure. However, when the same ionic liquid was

confined between hydrophobic surfaces, it did not induce any hardening in its molecular structure or phase transition.

2.11.8.2 Density oscillation

One characteristic behavior of liquids on surface and in confinement, is the presence of density oscillation. The ordering of hydrophobic [BMIM][PF6] on the hydrophobic graphite surface has been investigated by MD simulation using OPLS –AA forcefield in Gromac software with 490 ion pairs.[177] A dense layer was formed on the surface and there was a clear oscillation in the density profile, which indicates presence of solvation shells. The dense layer formation on the graphite surface was probably due to strong interaction between IL and the graphite surface. Number of oscillation cycles (or solvation shells) decreased with increase in molecular flexibility. This is because flexible molecules pack effectively without layering.[167] Another MD simulation study with [BMIM][PF6] and [OMIM+][PF6-] on graphite surface found that the density at the interfacial region is very high and the density oscillation extends upto 15 Å in the bulk.[181] Because of high concentration of ionic liquid and strong interaction between ions, the Gouy-Chapman classical model, that is used to describe ion layering on a surface in dilute electrolyte solution, is not valid. Thus a new theory is required that can account for the finite size of the ions. Recently a model for double layer capacitance of ionic liquid has been developed but this does not account for the asymmetry of the ions, intramolecular charge distribution and specific adsorption of ions at the surface. However, this theory does not describe the ion correlation effect in high concentrated solution. In a similar study, the researchers conducted MD simulation with [BMIM][PF6] on graphite surface using AMBER forcefield for 0.5 ns production run.[180] The simulation was performed on charged (both positive and negative) and uncharged surface. The relative mass density near the wall had an oscillatory profile. The highest

peak had a density almost twice of that of the bulk density and the density at the free surface was also higher.

2.11.8.3 Ion layering and orientation

In molecular liquid, presence of atomically smooth surface induces layering of liquid molecules on the surface. In ionic liquids, which already have some nano structures, presence of a surface induces alignment of those preexisting bulk structures. The width of the aligned liquid layer depends on the surface charge. Mica which is a highly charged surface induces thicker layer compared to weakly charged silica surface. Graphite surface induces six to seven solvation shell layers and this number of layer is more than those found on mica or silica. The difference is due to the manner ions prefer to pack on the surface (perpendicular orientation is preferred on mica compared to parallel on graphite).[167] Type of the ionic liquid and temperature seem to have an effect in the layering process. Crystal forming ionic liquids make stronger layer,[186] whereas higher temperature reduces ion layering on the surface.[191]

The cation orientation on the surface determines the anion orientation and the relative position of the double layer.[180] It is observed that organic compounds containing carbon or heterocycles orient parallel to graphite surface. In case of negatively charged surface, only cations forms layer on the surface. There are no anions in the first layer. The layers are formed in alternating fashion of positive and negative charges. The opposite phenomenon happens in case of positively charged surface.

Vapour/liquid interface also shows ion layering. Structure on free surface (vapour/liquid interface) was studied by various researchers using metastable atom electron spectroscopy[178] and molecular dynamic simulations.[183] In the experimental work, different ionic liquids were

investigated. These ILs have [$C_n$mim] cation, where the number of carbon atoms in the chain varies (n = 4, 8, 10). The different anions were BF_4 (tetrafluoroborate), OTf (trifluoromethane sulfonate) and TFSA (bis(trifluoromethylsulfonyl)amide). It was found that, for the IL with alkyl chain length n = 4, the free surface is made up of both anion and cation. The alkyl chain and the aromatic ring lie horizontally on the free surface. The alkyl chain preferred to be in the vacuum side. For ILs with longer alkyl chain (n>4), the alkyl chain oriented towards the outer most surface and covered polar moieties. Molecular dynamic simulation using [BMIM][PF6] also revealed similar orientation on free surface.[183] The mass density at the vapor liquid interface is also higher compared to the bulk density. The contribution of the cation on the mass density is higher than the anion.

2.11.8.4 Surface potential and solvation shell

Adsorption of ionic species tends to reduce surface potential. Behavior of ionic liquid [BMIM][PF6] and [OMIM+][PF6-] on graphite surface has been studied by MD simulation.[181] The larger cation [OMIM+] brings a larger potential drop on the graphite surface compared to the smaller cation, [BMIM+]. The positively charged cation layer on the graphite surface causes another ion layer and forms thicker IL-Graphite interface. The surface potential drop is caused by the protrusion of the alkyl side chain from the graphite surface. The IL with longer alkyl chain tends to coordinate more anion and lowers surface potential.

The polar groups tend to aggregate and form a polar domain, whereas the non polar groups fill the remaining space. Molecular simulation and X-ray diffraction shows distinct microstructure in ionic liquids due to clustering of polar and non polar groups which is similar to surfactant self assembly in water. The mechanical properties of such structure were measured by AFM.[167,179]

The AFM tip was used to measure the force necessary to push through the solvation shells found at the interface. The researchers defined 'solvation force' as the force required to rupture a salvation shell. They observed that there is a series of repeating 'push through'. This indicates presence of several solvation shell layers on the surface. In addition, there was significant increase in the rupture force that was necessary near the surface. As the molecular flexibility increased due to presence of long alkyl chain, the solvation layers become more compressible. The cations binded on the mica surface so strongly that even the AFM tip could not displace them. Drop in surface potential also results in reduction in friction coefficient. Shear stress measurement of the ionic liquid film confined between mica surfaces revealed 1 to 2 orders of magnitude less friction coefficient.[190]

2.11.8.5 Surface reaction

Traditional batteries depend on graphite anode and alloy anodes due to dendrite formation on Li metal anode. Dendrite formation can be prevented by using IL although no clear reason for this is known. Abinitio study was conducted with EMIM-BF4 crystal interaction with Li(100) surface as a model for IL/Li interface.[184] This showed that adsorption of EMIM-BF4 molecular pair on Li surface form Li_x-BF4 species and causes partial reduction of EMIM within the surface. Studies using EMIM-BF4 crystal also showed similar reaction features as the molecular EMIM-BF4. It was found that the reduced $EMIM^+$, which was not directly in contact with Li surface, may act as electron accumulator. This study was the first attempt to understand IL reaction on a Li metal surface.

2.11.8.6 Surface tension

Vapor liquid interface properties of [BMIM][PF6] ionic liquid has been studied by MD simulation.[183] The surface tension was measured using the diagonal element p_{ii} of the pressure tensor using the following equation.

$$\gamma = -\frac{L_z}{4}(p_{xx} + p_{yy} - 2p_{zz})$$
(2.11)

where L_z is the length of the periodic box in Z direction. But the computed results seem to underestimate the experimental result. Therefore other methods like free energy perturbation, polarization forcefield may be applied to find accurate result.

2.11.9 Behavior of ionic liquid and Li salt mixture

Viscosity of ionic liquid is around 30 to 50 cp, which is significantly higher compared to the viscosity of water (0.89 cp).[159] Addition of Li salt further increases IL's viscosity. This means that to enable penetration of the electrode pores by IL, the electrode may need prior treatment like keeping under vacuum. Room temperature conductivity of some ionic liquids are in the range of 0.1 to 18 mS /cm. This is similar to the conductivity of traditional carbonate based Li ion electrolytes.

Transport number of cation (t_+) and anion(t_-) is defined as the ratio of a particular ion diffusion and the total diffusion. It is given by the following equation where D_+ and D_- are the diffusion coefficients of cation and anion respectively.

$$t_+ = \frac{D_+}{D_+ + D_-}$$
(2.12)

and

$$t_- = \frac{D_-}{D_+ + D_-} \tag{2.13}$$

In a Li salt mixed system, Li transport number depends on the type of IL and its property such as diffusion and viscosity. Transport number of Li ion in ionic liquid mixture is found to be very less.[158]

Behavior of quarternary ammonium based ionic liquids and the effect of addition of Li salt LiTFSI was studied by heteronuclear NMR spectroscopy.[196] The researchers found that addition of salt increases viscosity and decreases ion conductivity. Glass transition temperature (T_g) is also increased due to addition of Li salt. Large amount of LiTFSI salt may results in total amorphization of the IL. This indicates loss of IL structure, which may result in detrimental effect on transport property of the IL.

2.12 Simulation of liquids

2.12.1 Liquid state

Liquid state is considered as intermediate between gas and solid state. The property of a liquid substance is given by the equation of state as presented below. This equation captures the relationship between pressure (P), temperature (T), and number density (ρ).[165]

$$f(P, T, \rho) = 0 \tag{2.14}$$

On a temperature scale, a liquid state is bounded from above by critical point and from below by triple point temperature. The liquids may be treated by classical theories to describe its property if the thermal De Broglie wavelength of the atoms is less than the nearest neighbor distance and

the rotational temperature of the molecules is less than macroscopic temperature T of the system which arises due to kinetic energy of the molecules. This rotational temperature Θ_{rot} is given by equation 2.15, where k_B is Boltzman constant, $\hbar$ is Planck's constant h divided by 2π and I is moment of inertia.

$$\Theta_{rot} = \frac{\hbar^2}{2Ik_B} << T \tag{2.15}$$

The classical approximation leads to a simplification that the thermodynamic property due to thermal vibration is separated from neighbor interaction and gives easy calculation of various properties. [165] If V_N is the total potential energy of the system, K_N is the total kinetic energy, then

in liquid state $\dfrac{K_N}{|V_N|} \approx 1$ whereas in gaseous state $\dfrac{K_N}{|V_N|} >> 1$ and in solid state $\dfrac{K_N}{|V_N|} << 1$

Liquids are different from dilute gases, in liquids there are more atomic collision, short range and positional correlations between atoms and molecules. However liquids lack of long range order which is present in solids. The repulsive interaction between atoms at short range creates the short range order for liquid molecules. The attractive force that operates at long range has small effect in creating liquid structure, but they form a uniform background of cohesive energy to stabilize the liquid.

Classical macroscopic measurements give information about static properties like thermodynamic property, equation of state, compressibility. The transport properties, like diffusion can be obtained from NMR and other spectroscopic methods. This can also give the reorientation motion of molecular liquids. The dielectric response measurement gives slow

structural relaxation of supercooled liquid. Other properties of interest are shear viscosity and thermal conductivity.

The fluid near the surface of confinement may be treated as inhomogeneous fluid where the homogeneity is broken by the exposure to the external field created by the surface or interface. The change in grand potential associated with the infinitesimal change in thermodynamic state of a system containing an interface is given by:

$$d\Omega = -SdT - PdV - Nd\mu + \gamma dA \qquad (2.16)$$

where the last term γdA represents the surface forces. The density profile shows a fluctuation behavior near the surface.[148]

The thermal expansion coefficient (α) is the change in volume with temperature and is calculated using the following equation, (the symbols have their usual meaning):

$$\alpha = \frac{1}{V}\left(\frac{\partial V}{\partial T}\right) \qquad (2.17)$$

The heat capacity is defined by:

$$C_p = \frac{\partial E}{\partial T} \qquad (2.18)$$

and specific heat capacity is given by:

$$c_p = \frac{1}{m}\left(\frac{\partial E}{\partial T}\right)$$

(2.19)

Whereas, compressibility can be calculated from the V vs P graph as the change in volume with pressure by the following equation:

$$k = -\frac{1}{V}\left(\frac{\partial V}{\partial P}\right)$$

(2.20)

Bulk modulus, which gives the resistance to compression, is defined as ($1/k$). However a different formula based on fluctuation property may be used to calculate isothermal compressibility.[197]

$$k = \frac{\langle V^2 \rangle - \langle V \rangle^2}{k_B T \langle V \rangle}$$

(2.21)

2.12.2 Structural feature

Structure of the liquid can be obtained from radial distribution function $g(r)$, which can be measured from radial scattering experiment. This function gives a probability of finding a pair of atoms which are apart by a distance r. This function shows a pattern of peaks and troughs, and tends to be 1 at large r and 0 at small r. The integration of g(r) upto the first minimum gives the nearest neighbor number, or the 'coordination number'.[148] A similar function called charge distribution function $Q_i(r)$ may be defined as the net charge at distance r from a central ion i having charge q_i. It is given by the equation 2.22 as below.

$$Q(r) = 4\pi r^2 q_i Q_i(r) dr \tag{2.22}$$

Charge distribution function is related to the radial distribution functions as:

$$Q_C(r) = \rho[(g_{cc}(r) - g_{ca}(r)] \tag{2.23}$$

and

$$Q_a(r) = \rho[(g_{aa}(r) - g_{ca}(r)] \tag{2.24}$$

$$Q(r) = Q_{cc}(r) + Q_{aa}(r) \tag{2.25}$$

where $Q_a(r)$ and $Q_c(r)$ are the charge distribution function for anion and cation respectively and $Q(r)$ is the total charge distribution function. Charge distribution function may be fitted to the following equation 2.26. This equation represents strongly coupled ionic system where the total charge has oscillatory decay profile with λ_D, the Debye- Huckel screening length, A is decay amplitude, d is the period of oscillation, Φ is the phase shift.[198]

$$Q(r) = (A/r) \exp(-r/\lambda_D) \sin(2\pi r/d + \varphi) \tag{2.26}$$

λ_D may obtained by fitting total charge distribution function to this equation or from the slope of the tangent through the maximum points of the periodic function of   ln| rQ(r)| vs r plot (i,e λ_D =(1/ slope) of the ln| rQ(r)| vs r plot).

2.12.3 Transport properties

Time dependent correlation and response function of any observed dynamic variable such as dipole fluctuation, velocity fluctuation, etc., which is obtained from molecular simulation give the transport properties of the fluid. Time correlation function gives a clear picture of the dynamics of the fluid. The integral of the correlation function gives the macroscopic properties. The Fourier transform of the time correlation function may be related to the experimentally observed spectras.[148] A dynamic variable, A(t) of system of *N* particle, is a function of some or all the time-varying coordinates, r_i and momenta p_i, i = 1 to *N*. Considering that we have two such variables, their time correlation can be given as :

$$C_{AB}(t',t'') = \langle A(t')B(t'') \rangle \tag{2.27}$$

where *t' >> t''*. The angular brackets < > represent an ensemble average over initial condition or an average over time. The most important class of time correlation is the autocorrelation function C_{AA} (t',t''), for which *A* and *B* are the same.

For example, the velocity autocorrelation Z(t), where *A* as in equation 2.27 is the particle velocity u(t), gives the self diffusion constant of the particles, as below.

$$Z(t) = \frac{1}{3} \langle u(t).u(0) \rangle \tag{2.28}$$

Where diffusion is the time integral of this autocorrelation function and is given by:

$$D = \int_0^\infty Z(t)dt \tag{2.29}$$

This is called Green-Kubo formula. These classes of relations are very important in obtaining macroscopic dynamical property from time integration of microscopic time-correlation function.[148]

Diffusion can also be obtained from the mean square displacement of the 'random walker' using the Einstein equation:

$$D = \lim_{t \to \infty} \frac{\left\langle | r_i(t) - r_i(0) |^2 \right\rangle}{6t} \tag{2.30}$$

Ionic liquid has been observed to behave like supercooled liquid. Thus a Vogel-Fulcher-Tamman (VFT) equation describes its diffusion behavior with temperature rather than Arrhenius equation. This VFT equation is given by equation 2.31, where B and D_0 and T_0 are constants.

$$D = D_0 \exp[-\frac{B}{(T - T_O)}] \tag{2.31}$$

2.12.4 Conductivity

Conductivity can be calculated from diffusion coefficient. As described earlier, the velocity autocorrelation and self diffusion coefficient gives single particle motion. If the mixture is nearly ideal the total diffusion becomes:

$$D = x_2 D_1 + x_1 D_2 \tag{2.32}$$

where x_1 and x_2 are mole fractions of two diffusing species and D_1 and D_2 are their diffusion coefficients. For neutral particles, the cross correlation between particles are negligible. The static electrical conductivity σ is proportional to the time integral of the electric current

autocorrelation function which again depends on diffusion coefficients. The simpler form may be given by the equation below:

$$\sigma = \beta e^2 \rho (x_1 z_1{}^2 D_1 + x_2 z_2{}^2 D_2)(1 - \Delta) \qquad (2.33)$$

The deviation factor, Δ is a measure of the importance of cross correlation terms. When Δ equals to 0, then the above equation is called Nernst-Einstein relation.[165] In case of ionic liquids, the molar ionic conductivity (Λ_0) can be calculated using Nernst-Einstein relation, where D^+ and D^- are the diffusion coefficients for cation and anion respectively.

$$\Lambda_0 = \frac{z^2 F^2}{RT}(D^+ + D^-) \qquad (2.34)$$

2.12.5 Viscosity

An important feature of liquid is the viscosity, which is the ratio of shear stress vs shear strain. The viscosity of the liquid arises due to internal friction in the fluid that results in resistance to flow in the macroscopic level. Liquids are classified as Newtonian or non-newtonian based on their viscosity. Newtonian fluids, for example, low molecular weight pure liquids have constant viscosity irrespective of the strain. Polymer, colloidal suspension and emulsions will undergo increase or decrease in viscosity (thicker or thinner) with applied strain. Viscosity may be defined as kinematic or dynamic (absolute) viscosity. The unit of absolute viscosity (η) is Poise (P), gm. $cm^{-1}.s^{-1}$. Kinematic viscosity (v) is dynamic viscosity divided by density (ρ) with unit Stokes (St, $cm^2\ s^{-1}$).

In a molecular simulation viscosity is measured by pressure fluctuation method and then using Green–Kubo method. However this may have problem like non convergence, and thus non equilibrium method is employed sometimes.[199] But it has been demonstrated that using a slightly different method of data analysis may give us viscosity value with reasonable accuracy.[199]

The shear viscosity is obtained using Green-Kubo formula as below:

$$\eta = \frac{V}{k_B T} \int_0^\alpha \left\langle \sum_{\alpha\beta} P_{\alpha\beta}(0) P_{\alpha\beta}(t) \right\rangle dt \tag{2.35}$$

or by Einstein relation as follows:

$$\eta = \frac{V}{k_B T} \lim_{t \to \alpha} \frac{d}{dt} \left\langle \sum_{\alpha\beta} (G_{\alpha\beta}(t) - G_{\alpha\beta}(0))^2 \right\rangle \tag{2.36}$$

where

$$G_{\alpha\beta}(t) = \int_0^t P_{\alpha\beta}(t') dt \tag{2.37}$$

$P_{\alpha\beta}$ is the symmetrized traceless portion of the stress tensor. It is defined as :

$$P_{\alpha\beta} = \frac{1}{2}(\sigma_{\alpha\beta} + \sigma_{\beta\alpha}) - \frac{1}{3}\delta_{\alpha\beta}(\sum_Y \sigma_{YY}) \tag{2.38}$$

Where $\delta_{\alpha\beta}$ is the Kronecker delta. $\delta_{\alpha\beta} = 0$, when α is not equal to β. This equation uses averaging over diagonal components of the stress tensor and gives better result.

Sometimes short correlation may be used to calculate viscosity, preferably at early correlation time than later times.[166] Once the linear region of the MSD has been reached then that data can be taken for viscosity calculation to avoid larger statistical error at longer time scale. If the time period at which the viscosity calculated is long, the integration will be influenced by the noise in the pressure correlation function and may result in large errors.

2.12.6 Dipole moment and dielectric constant

Dipole moment of the molecules may be calculated from the charges and the positions of the atoms as follows:

$$\mu_i = \sum_{i=1}^{n} r_i q_i \qquad (2.39)$$

Total dipole moment is given by summation over all molecular dipoles :

$$M_j = \sum_{j=1}^{N} \mu_i \qquad (2.40)$$

Dielectric constant can be obtained by using Clausius-Mossotti equation as follows:

$$\frac{\varepsilon - 1}{\varepsilon + 1} = \frac{4\pi}{9k_B TV}[\langle |M|_j^2 \rangle - \langle |M|_j \rangle^2] \qquad (2.41)$$

The amount of time required to reorient the dipoles are called relaxation time. At low frequency operation of the battery, when the periods (1/frequency) are longer than relaxation time the

dipoles will be fully oriented. Thus relaxation time is important in electrode polarization. This indicates the allowable frequency range to operate the battery electrode.

Relaxation time (τ) may be calculated as follows:

$$\tau = \int_0^\alpha C(t)dt \qquad (2.42)$$

It is the time integral of the orientation correlation function. Usually τ decrease with increase in temperature. Relaxation time may also be obtained by fitting the dipole auto correlation function to a multi-exponential function[200] and taking the time constants as follows:

$$\phi(t) = A_1 e^{(-\frac{t}{\tau 1})} + A_2 e^{(-\frac{t}{\tau 2})} + A_2 e^{(-\frac{t}{\tau n})} \text{........} \qquad (2.43)$$

2.12.7 Challenges in simulation studies on ionic liquids

Ionic liquids are challenging materials to study using computational methods. Suitable forcefield are required to accurately predict the complex interplay of various atomic interactions. In molecular simulation, a Forcefield is the mathematical expression that represents all different types of interaction that are present in the particular atomic/molecular system. The difficulty in modeling ionic liquids arises because of several reasons.[201] These are described in the following paragraphs.

In general, liquid phases are difficult to model computationally as these have atoms with long range correlation. This difficulty arises because liquid molecules interact with each other unlike molecules in a gas, which are far apart, therefore does not need any computation to model such nearly non existent interactions. But compared to solid molecules for which the interactions are

symmetric and static, the interaction in liquid molecules are randomized and dynamic. Thus errors are introduced when one tries to extract a part of the liquid and study its properties. Ionic liquids being made up of charged species, further increases this difficulty. A combination of quantum mechanics, molecular dynamic and Monte Carlo simulation may be used to handle some of these problems.

In addition, there is another problem. High viscosity of ILs results in sluggish dynamics and requires simulation in much longer time scale compared to simple liquids. Size of the ions are large thus even a reasonable simulation system size may contain large number of atoms and make the calculation computationally expensive.

Furthermore, the complex types of interaction between the cations and anions involving coulomb, van der Waals, dipole-dipole, solvophobic, hydrogen bond requires careful formulation of the forcefield. Coulomb interaction tends to produce charge ordering. The aromatic π electrons above and below the imidazole ring plane may interact with anion electron cloud and the resulting dispersion forces may be significant, and it is extremely difficult to model. In addition, also due to anisotropy of the ions, alignment of higher multipoles may induces orientational correlation in charge densities. This affects the dynamic behavior.

Study on the effect of variation in charge distribution on the dynamics of molten salt found that introduction of symmetry has a profound effect on liquid dynamics.[202] By changing the combination of cation and anion one can obtain 10^{15} variations of the IL, all of which have completely different properties. Studies have shown that structural inhomogeneity and electronic polarizability of ions affect ion dynamics. Although liquid charges are not highly sensitive to ionic charge distribution, dynamic property is sensitive to charge distribution. Asymmetric ions

diffuse more rapidly because of stronger coulomb interaction coupling between rotational and translational motion of the asymmetric species. In the absence of such coupling, rotation is relatively rapid but the translation is slow. It is possible that quadrupole terms or even higher terms influence collective dynamics of ionic liquids. Thus incorporating all different types of interaction in the forcefield is essential to obtain reliable results from the simulation.

Thus the electronic structures of the ions need to be well described and require accurate charge distribution on the atoms to obtain acceptable result from molecular simulations.[201] Therefore in order to understand the properties of IL a combination of different computation tools are required.

2.12.8 Forcefield for ionic liquids simulation

OPLS-AA forcefield (FF) has also been used to study dynamic behavior of [BMIM][BF4] using molecular dynamic simulation using.[203] The computed liquid density, heats of vaporization, diffusion coefficients are quite similar to the results reported to the experimentally observed values and the value obtained for other ILs.

Most widely used FF is the all-atom molecular forcefield proposed by Lopes and coworkers, based on OPLS-AA with AMBER parameter.[204] This FF predicts the density well but the dynamic and thermodynamic properties are not well represented by this model. In addition, the interaction between anion and cation are overestimated by this FF.[205]

The above FF has been refined by changing the LJ parameters to represent experimental data accurately. Dynamic behavior of five different ionic liquids [$C_n$mim][NTf2] (n =1,2,4,6,8) has been studied with parameterized forcefield.[205] This study computed self diffusion coefficient,

rotational correlation times and viscosity. These values were very similar to the experimentally observed values.

One of the major improvements in forcefield for ILs is that polarization effect was incorporated. Polarization has two effects. The first one includes additional charge-dipole, and dipole-dipole interaction that enhance short range electrostatic interaction and the second one takes care of charge screening effect that reduces long range interaction. All of these are present in IL systems. An electronically polarizable FF has been used to model the properties of [EMIM][NO3] and was compared with those of a non polarizable model.[206] The forcefield parameters were based on AMBER FF. Polarizable model showed altered radial distribution function and enhanced structural heterogeneity compared to non polarizable model, due to enhance delectrostatic interaction. Simulation with polarization model showed slow dynamics of the liquid, free rotor behavior of hydrogen atoms, faster ionic relaxation of the ethyl group due to weak interaction. The EMIM cations have a tendency to pack with imidazole rings parallel to each other and bridged by hydrogen bonds. Simulation based on polarization model was suggested to be similar to non–polarization model at higher temperature.[206]

Monte Carlo simulation has been performed to understand structure, thermodynamics and solution dynamics and CO_2 adsorption in [BMIM][PF6].[197] The researchers used an all atom forcefield (with no explicit hydrogen of fluorine) which is computationally less demanding yet provided accurate prediction for experimentally observed parameters. The density, isothermal compressibility, volume expansivity and solution thermodynamics of CO_2 in IL was determined.

CHAPTER III

SIMULATION METHODOLOGY

In this chapter we present the molecular structures, computational methods and tools used in the simulation studies on scaffolded carbon nanotubes, MOFs and ionic liquids.

3.1   Studies on sorption by carbon nano structures

3.1.1   Carbon nanotube scaffold structures used

The nano scaffolds with (6,6), (9,9), (12,12), (21,0), (15,15) and (18, 18) tubes, having tube diameters 8.14 Å, 12.20 Å, 16.27 Å, 16.44 Å, 20.34 Å and 24.4 Å respectively, were prepared by using Materials Studio (MS)[207] suite of programs. The tubes were arranged in a triangular lattice, connected by methylene di-aniline linker. For (n, n) or (n,0) tube, n is a multiple of three, because the linkers were placed 120^0 apart on the circumference of the tube cross section to get a strain-free triangular lattice (Fig. 3.1).
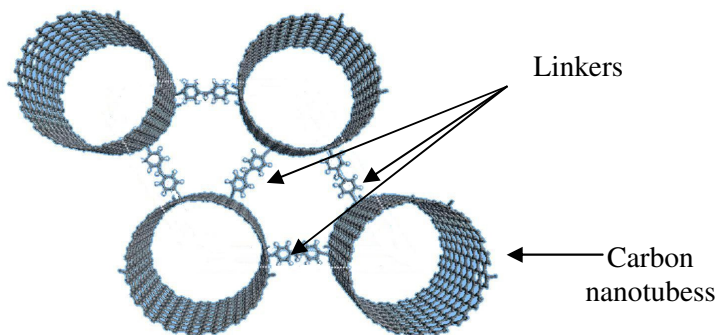
Fig. 3.1 CNT scaffold showing three linkers in triangular arrangement

The linker length is ~11 Å and this effectively defines the distance between the tubes. For each type of tube, different structures were prepared with linker molecule attached at different spacing in the tube axis direction for studies aiming to understanding the role of linker spacing/frequency on the sorption behavior. Scaffolds with linker spacing of: 4L, 7L, 9L and 12L, having inter liker distances of 9.8 Å, 17.2 Å, 22.1 Å and 29.5Å respectively, were considered

3.1.2   *Sorption simulation methods used*

The sorption studies were performed by Grand Canonical Monte Carlo (GCMC) simulation using Cerius2 software.[208] We choose GCMC method because it is computationally inexpensive and a quick yet reliable method to get a general idea about the hydrogen sorption efficiency of nanoporous materials based on van der Waals and electrostatic interactions. In this method, the H_2 sorbate molecules (with rotational and translation degrees of freedom) are randomly created and destroyed. Probability of creation and destruction of hydrogen molecules was set at 0.3. Dreiding forcefield which is suitable for organic molecules was used to perform the simulations. For proper electrostatic interaction representation, hydrogen was specifically modeled as a quadrupole with -0.96e charge at the center and +0.48e charge positioned at the two ends. In all these simulations, coulomb interactions were considered in addition to van der Waals interaction, while calculating the total interaction energy and forces. Special attention was given to exclude the spaces that are inaccessible to the sorbate molecules. Atoms in the scaffold framework were kept rigid during the simulation.

Usually when the tubes are prepared experimentally they are capped at both ends by fullerene which prevents hydrogen sorption inside the tubes. To simulate this, we placed a suitable

diameter column of point particles, inside the nanotubes, which blocked hydrogen sorption on the inside tube surfaces (shown as blue spheres in Fig. 3.2).
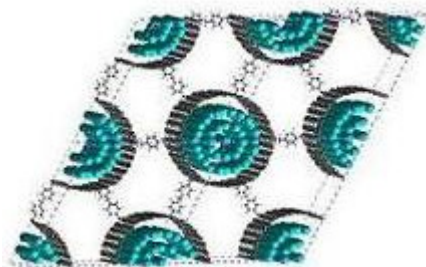
Fig. 3.2 Scaffold with point particles inside the tubes

The simulations were run for 1 million steps at each pressure, of which last half a million steps were considered for data collection. Each simulation was started at lowest pressure with an empty framework. Each subsequent simulation step was started with the final structure of the previous step. Simulations were carried out at two different temperatures: 77 K and 298 K, over a range of gas pressures (1 to 100 atm). Surface area and accessible volumes were calculated by using the method provided in Cerius2 program.

Cerius2 uses Connolly surface area method to find the solvent accessible surface of a molecule or a structure. Connolly surface is the van der Waals (VDW) surface that is available to a probe molecule having a nonzero radius. A spherical probe (in this case a molecule with radius 1.4 Å) is rolled on the VDW surface of the scaffold structure to generate the Connolly surface. This gives the surface area available for sorption.

In our simulation we have assumed that the same periodic boundary condition exists in all direction. This means that all the cells are equally available for gas adsorption. In real structures, the spacer material creates barrier for hydrogen flow that has to diffuse in the cells that are

embedded deep inside the scaffold. Our simulation does not capture the hydrogen diffusion barrier due to depth of the scaffold material which will lower the adsorption capacity in the cells that are buried deep inside. We only observe that the effect of denser spacer arrangement on sorption capacity due to stearic hindrance to gas diffusion, but not due to depth of scaffold material.

3.1.3   Studies with functionalization on tube surface

Based on the initial simulation results with scaffolds with different tube diameters, the best performing scaffold made up of (18, 18) tubes were selected for further studies. Also considering the fact that experimentally observed tube diameter is ~14 Å, the scaffold with (12, 12) tube having similar 16.27 Å diameter, was also chosen to be studied further. These (12,12) and (18,18) tube scaffolds were used to study effect of exclusion of tube interiors, different covalent functionalization and Li incorporation.

To study the effect of a variety of functionalization of the tube surfaces on sorption capacity in the similar lines as done by others[17] who studied with only chlorobenzene group, we have added: chlorobenzene, nitro, carboxy, amino and carbene functional groups with and without sulfonate groups. These functional groups were attached to the tube exterior walls, in addition to the cross linking agent.

3.1.4   Studies with Li

For studying effect of Li incorporation on tube surfaces, we incorporated 100, 120, and 150 Li^{+1} atoms on the external surface of (12,12), 12L and (18,18), 12L tube scaffolds. These values were chosen considering the fact that previously studied[24,25] optimum Li:C ratio was found to be 1:6.

The forcefield was set with Lennard-Jones (L-J) 12-6 potential parameters of Li. These parameters were based on the experimental LiF crystal properties. The experimental cohesive energy and lattice parameter of LiF crystal is 246 kcal/mole and 4.02 Å.[209] The LJ parameters r_0 and D_0 for Li as given in Dreiding forcefield were optimized by until a matching value (within +/- 5% of the experimental value) for the cohesive energy and the lattice parameters was obtained. The final LJ parameters for Li are r_0= 2.6975 Å and D_0= 0.065 kcal/mole. This type of parameterization has been done for other metals like K, Rb, Br_2 and they were found to be good to predict various properties for metal intercalated graphite intercalation compound.[210] Thus we assumed that this parameterization method is also good to capture Li interaction with CNT and hydrogen and therefore it was used in our simulation.

3.1.5   Sorption capacity measurement

Sorption capacity was measured in terms of total adsorption and excess adsorption percentages.

The total adsorption capacity % is defined as:

$$\text{Total wt \%} = \frac{N * m}{(M + N * m)} * 100 \qquad (3.1)$$

Where, N is the total loading of hydrogen (number of molecules), m is the molecular weight of H_2 and M is the molecular weight of the empty scaffold framework.

Excess adsorption is defined as the amount of additional hydrogen that can be stored in a given volume when adsorbing substrate is present, compared to free volume hydrogen storage. A positive excess capacity measures the effectiveness of the adsorbing substrate. Therefore the excess adsorption capacity % is defined as:

$$\text{Excess wt } \% = \frac{(N - \rho_{bulk}V_{cell}) * m}{\{M + (N - \rho_{bulk}V_{cell}) * m\}} * 100 \qquad (3.2)$$

Where ρ_{bulk} is the bulk hydrogen density (molecules per m^3) at the same temperature and pressure at which the adsorption took place. Hydrogen density was obtained from NIST database.[211]

3.2 Study on mechanical properties of MOFs

3.2.1 MOF structures used

The structures for IRMOF-1 (MOF-5), IRMOF-3, IRMOF-6, IRMOF-8, IRMOF-10 and IRMOF-14, used in this study, were constructed in Cerius2 software[208] based on the coordinates obtained from available literature.[28]

3.2.2 Computational methods used

Molecular dynamic simulations were performed using Universal Forcefield (UFF). UFF is suitable for both inorganic and organic molecules and have been used successfully for hydrogen sorption studies on MOFs and similar Covalent organic frameworks (COF).[212,213] Thus we have used this forcefield to conduct preliminary study on structural behavior of various MOFs. Periodic boundary condition was applied to simulate bulk behavior. Minimum energy configuration was obtained by minimizing the potential energy as a function of the coordinates and unit cell parameters by the standard convergence criteria (atomic root mean square energy 0.1 Kcal/mol) using smart minimizer. It uses a combination of steepest descent (maximum gradient >100) conjugate gradient (maximum gradient <100) and Newton-Raphson (final convergence) methods. Before every simulation the energy in the structure was minimized to

remove bad contacts, if any, to optimize bond lengths and angles, and to get the final and stable conformation.

Molecular dynamics (MD) simulations was carried out to determine the time evolution of MOFs at different conditions. Molecular dynamic simulation solves classical equation of motion of a system of N atoms interacting according to the potential energy set by the forcefield. The atoms are given an initial velocity and integration time step (1 femto second). The integration of the equation of motion is carried out by Verlet Leapfrog algorithm to determine the new coordinates and the calculation continues for the desired time step. The system was first equilibrated using NVE ensemble simulation for 10 pico sec (ps). To observe the behavior under a given pressure the NPT ensemble simulation was carried out for 100 pico sec of simulated time. Temperature was kept constant by using Nose-Hoover thermostat. Pressure was controlled by Parrinello-Rahman method where both the size and shape of the crystal cell can change.

In NPT ensemble the surrounding is maintained at desired constant pressure and the virtual piston is used to transmit the same pressure to the system. Mass pre-factor, which gives an idea how tightly the system is connected with the surrounding, was kept between 0.1 and 0.025. The molecular trajectory data were processed to compute required variables like change in lattice parameters, volume, intermediate conformations etc. These were used to obtain diffraction pattern, IR Raman spectra, diffusion behavior, mechanical property, etc.

We considered hydrogen as a representative gas and performed molecular dynamics simulations with hydrogen filled MOFs, as described below. The amount of hydrogen introduced was based upon experimental observations carried out by other researchers.[29,57] The first observation showed that 17.2 hydrogen molecules (4.5 wt%) were adsorbed per formula unit in MOF-5 at 77

K and at 1 atm pressure, which amounts to 136 hydrogen molecules per unit cell of MOF-5. This was considered as baseline of how much hydrogen can be introduced in the system. This is also comparable to the maximum possible number of 167 molecules of hydrogen that can be entrapped within the volume of a single cell crystal at 100 MPa at room temperature based on hydrogen density at same condition.[211] This number of 167 is calculated based on volume of the pore and volume of hydrogen molecule.

In our hydrogen filled MOF-5 simulation, we introduced 34, 68, 102 and 136 molecules per unit cell at room temperature. This study was performed to see how MOF-5 behaves when the pores are filled with hydrogen and also to study the high pressure diffusion behavior of H_2 in MOF. H_2-H_2 and H_2-MOF interaction were represented by Lennard-Jones potential as available in UFF. We have ignored H_2-MOF quadrupole-charge interaction and any quantum effect for hydrogen as these have little effect on simulating hydrogen diffusion behavior at room temperature.[106] The rate of diffusion of hydrogen was calculated from the slope of mean square displacement (MSD) of hydrogen molecules. Simulated powder X-ray diffraction pattern was obtained by Analytical-1 module of Cerius2. IR/Raman spectra were obtained by Analytical-3 module of Cerius2.

3.2.3   Calculation of elastic constants

The mechanical properties were calculated by Mechanical property module of Cerius2. The 6X6 stiffness matrix (C) and the compliance matrix (S) were calculated by the second derivative method. It calculates the coefficients from the second derivative of the potential energy function as given below:

$$C_{ij} = \frac{1}{V} \frac{\partial^2 E}{\partial \varepsilon_i \partial \varepsilon_j}$$

(3.3)

where i , $j =$ 1, 2....6

C_{ij} is the element of the stiffness matrix, E is the total energy, V is the volume of the unit cell and ε_i, ε_j are the strain components.

3.3   Simulation method for study on ionic liquids

We studied [BMIM][BF4] ionic liquid (the structure was presented in Fig. 1.3). QM calculations were performed in Gaussian 09[214] using density functional theory (DFT) employing B3LYP 6311-G++(d,p) basis sets, which uses both polarization and diffuse functions. Individual ions were optimized and the equilibrium structure was used to obtain charges (using ChelpG and MK method) and the IR spectra. Molecular mechanics (MM) with Dreiding forcefield was used to minimize the structure for further use in molecular dynamics (MD) simulation. MM and initial MD simulation was conducted using Cerius2 software.

Amorphous builder in cerius2 was used to create a simulation cell of 100 ion pair (3000 atoms) initially. All subsequent calculations were performed in a simulation box containing 800 ion pairs (24000 atoms). The energy was minimized while changing the simulation cell size to obtain a cell that has atom density similar to the experimental density. Further minimization and molecular dynamics was run in LAMMPS code.[215] The [BMIM][BF4] structure was annealed using NVT ensemble and Nose-Hoover thermostat. Annealing and compression was done to ensure that the configuration is well equilibrated, it is not trapped in any metastable state and also to achieve desired density value. The structure was heated in steps starting from 300 K to 700 K and then cooled back to 300 K, and this cycle was repeated for 3 times, with NVE equilibration in between. This made sure that the final structure is well equilibrated, based on

which further study will be conducted. The final structure has density 1.13 g/cm^3. Reported density for [BMIM][BF4] was 1.17 g/cm^3 at 303 K,[216] and 1.2048 g/cm^3 at 295.3 K.[169]

To understand volume change profile with temperature, MD simulations using NPT ensemble was conducted at temperatures from, 273 , 298, 323, 373, 423, 473, 523, 573 623, 673 K at 1 atm pressure. Temperature and pressure control was achieved by Nose-Hoover thermostat and Parinello-Rahman barostat, with integration time step of 1 femtosecond. Interaction cutoff distance was 15 Å. Simulation at each temperature was run for 500,000 steps (500 picoseconds) and thus for a total of 5 nanoseconds (ns). Velocity and positions were saved after every 100 steps.

Similar simulation was carried out at different pressure, 50, 100 200, 300 400 500, 600, 800 and 1000 atm to study pressure–volume relationship. The trajectory files and output files were analyzed to obtain various thermodynamic parameters. NVT dynamics were performed on bigger system (800 ion pairs) to 1 ns time range to understand dynamics properties at different temperatures.

To study behavior of ionic liquid on graphite surface and in nano confinement, 10 graphene layers was prepared using materials studio program. These layers were used for both the surface and nano confinement studies. For the surface study, 800 ion pairs of the ionic liquid were put on top of the graphene layers, where as for the confinement study two sets of layers were used and liquid ions were put in between. For the confinement system, NPT dynamics was carried out and for the single surface NVE dynamics was preformed. The Z direction of surface simulation box was extended upto 400 Å. The graphite surface and liquid was placed at the centre of the cell. The graphite layer was of 65 Å x 65Å x 36 Å in dimension.

Analysis of simulation trajectories were performed using equations and theories described in Chapter II to obtain radial distribution function, mean square displacement, diffusion coefficient, dipole autocorrelation function, velocity autocorrelation, dielectric constant, etc. Matlab[217] mathematical tools were used for data processing and analysis.

CHAPTER IV

HYDROGEN STORAGE IN CARBON NANOTUBE SCAFFOLD

In this chapter, we present the results obtained from our simulation studies on hydrogen sorption behavior of carbon nanotube scaffolds. We begin by presenting the physical properties of the chosen carbon nano structures as observed from our simulation models. Then, we present how the hydrogen sorption capacity of these materials varied with variation of hydrogen gas pressure, carbon nano tube diameters and linker spacing. These are followed by our observations and analysis of the thermodynamics of the adsorption. Next, we show the preferred adsorption locations in the carbon nanotube scaffolds. Finally, we ascertain the effects of incorporating functional groups and Lithium metal atoms on the carbon tube surfaces, to evaluate whether these can improve the adsorption capacity.

4.1 Physical properties of the scaffoldings

The key physical properties like: surface area, volume, density, which affect sorption capacity of the SWNT scaffolds, as observed from our simulation models are presented in Table 4.1.

Table 4.1 Physical properties of nanotube scaffolds prepared for the simulations

Tube type (n,n), Diameter		Functionalization	Cross linking periodicity (Å)	Density gm/cc	Surface Area m^2/gm
(6,6) 8.14 Å	4L		9.83	0.809448	2781.513
	7L		17.23	0.712581	2553.158
	9L		22.15	0.67953	2473.886
	12L		29.52	0.649885	2385.137
(9, 9) 12.20 Å	4L		9.83	0.739811	2188.441

Table 4.1 Continued

Tube type (n,n), Diameter		Functionalization	Cross linking periodicity (Å)	Density gm/cc	Surface Area m²/gm
	7L		17.23	0.679319	2539.790
	9L		22.15	0.662859	2475.454
	12L		29.52	0.631833	2421.857
(12, 12) 16.27 Å	4L		9.83	0.678073	2666.411
	7L		17.23	0.627196	2523.567
	9L		22.15	0.614861	2479.290
	12L		29.52	0.598775	2454.506
		12L (6chloro)	29.52	0.656707	2615.505
		12L (18chloro)	29.52	0.769751	2768.567
		12L (6cl4Sulfo)	29.52	0.719278	2647.463
		12L (only outer surface)	29.52	0.598775	1476.017
(15, 15) 20.34 Å	4L		9.83	0.627025	2605.198
	7L		17.23	0.585594	2454.279
	9L		22.15	0.571777	2425.953
	12L		29.52	0.561984	2414.323
(18, 18) 24.4 Å	4L		9.83	0.575879	2551.447
	7L		17.23	0.544859	2438.269
	9L		22.15	0.536811	2404.194
	12L		29.52	0.525671	2383.982
		12L (6chloro)	29.52	0.55712	2517.512
		12L (6cl4sulfo)	29.52	0.596679	2596.863
		12L (only outer surface)	29.52	0.525671	1368.341
(21,0) 16.44 Å	2L		8.52	0.6966	2573.634
	4L		17.04	0.629818	2346.271
	5L		21.3	0.616624	2299.179
	7L		29.82	0.594123	2248.593

We prepared several different types of scaffolds with different tube diameter, linker periodicity and tube surface functionalization for this study. The specific surface areas of the scaffolds vary between 1368 to 2781 m²/gm, which are comparable to the surface area of typical carbon

materials.[8,19] But the estimates from our simulation are higher than the experimental estimates by other researchers.[17] For example, the densities of these scaffolds vary from to 0.52 to 0.8 gm/cc which is lower than the experimentally observed densities (1.0 to 1.2 gm/cc) for SWCNT scaffolds.[17] Their experimentally observed surface area of 515 m^2/gm is less compared to the 1368 to 2781 m^2/gm values obtained from our simulation. In those experiments,[17] oleum (fuming sulfuric acid) was used in the preparation process. Oleum tend to attach to the linkers and tube wall and the researchers have to employ various strategies, such as heating at high temperature, reduce number of linker, etc to remove the solvent molecule. In addition water as contaminant may be present[218] which can lead to less than ideal surface area estimate. These issues are often associated with experimental work.

However, in our case we worked with atomically clean structures without any defects, imperfections or impurities, which gave us the ideal surface area estimate based on theoretical Connelly surface area calculation. Therefore given these realities we speculate that presence solvent, catalyst, water, impurities, etc. are some reasons which might explain the discrepancy between calculated (larger value) and experimentally (lower values) surface areas

4.2   Sorption capacity variation with gas pressure

Grand Canonical Monte Carlo (GCMC) simulations were performed on the scaffolds at pressures range of 1 bar to 100 bar at two temperatures, 298 K and 77 K. Fig. 4.1 and Fig. 4.2 present the adsorption isotherms, both in terms of excess adsorption capacity and total capacity respectively, for the scaffolds with linker periodicity 12L (cross linkers at every 12th layer). This linker separation exhibited the highest sorption capacity. At both temperatures, the scaffold of (18, 18) SWNT with cross linkers at 12L, exhibited the highest sorption capacity. For all types of

scaffolds, the excess adsorption capacity at 77 K is higher than that at 298 K. This is because, at low temperature, repulsive interactions between hydrogen molecules are less compared to higher temperature[138] thus more hydrogen molecules can be packed together.

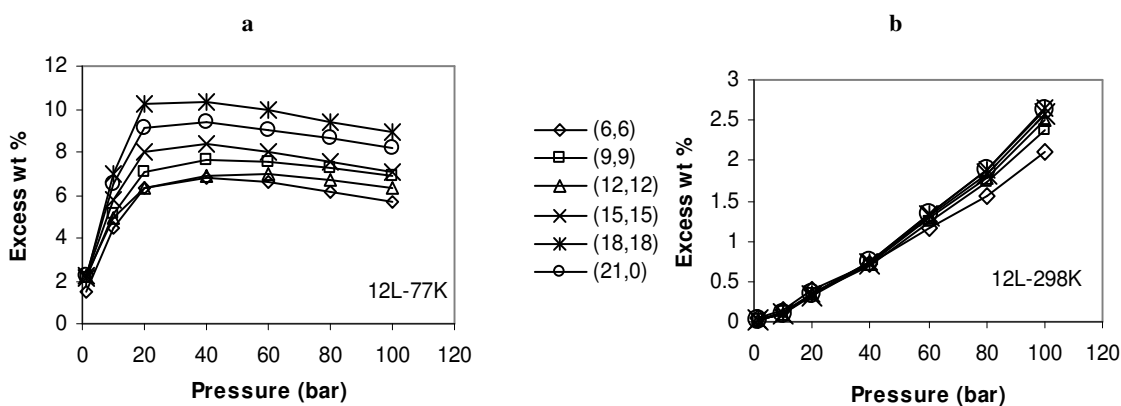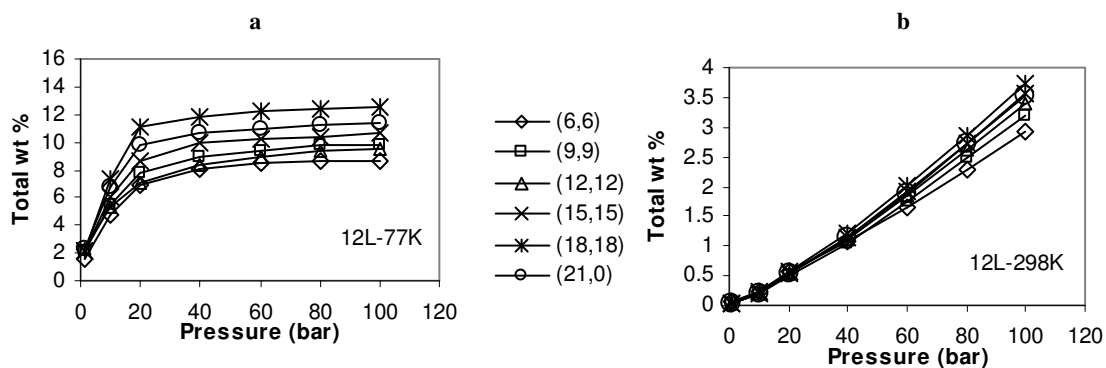**Fig. 4.1 Excess sorption capacity variation with pressure at 77K and 298K**

Fig. 4.2 Total sorption capacity variation with pressure at 77K and 298K

The 77 K sorption isotherms in Fig. 4.2a, show that the capacity reached a saturation point around 20 to 40 bar pressure region and only increased slightly at higher pressures above 40 bar. Fig. 4.1a shows that in this saturation region the excess capacity dropped

slightly. This is because the bulk density of hydrogen ρ_{bulk} increased more rapidly than the total loading of adsorbed hydrogen N (refer to the equation for calculating excess adsorption in section 2), and not because the adsorption decreased.

The (18,18), 12L scaffold showed the highest excess sorption capacity of 10.33 wt% (11.87% total capacity) at 77 K, and 40 bar. The maximum total capacity was 12.58 wt% with (18,18), 12L scaffold, obtained at 77 K and 100 bar. The volumetric sorption capacity (not shown in figure) reached a maximum value of 81 gm/L for (12,12) tube with cross linker with 9L periodicity at 77 K, 100 atm. At 77 K the volumetric capacity for all other scaffolds, except (9,9) tube with cross linkers at 4L, exceeded DOE volumetric storage target (45 gm/L).[5]

At 298 K, for a pressure range up to 40 bars, there is not much difference in sorption capacity between the scaffolds of different tubes (Fig. 4.1b & Fig. 4.2b). The difference becomes prominent only at higher pressure. At 298 K, the (18,18) tube with 12L cross linker spacing exhibited a maximum excess capacity of 2.66 wt% (total capacity 3.72 wt%) at 100 bar without reaching saturation. This indicates that there is still plenty of space available for further storage at 298 K, which may be achieved at higher pressure. The (12,12), 9L scaffold has the highest volumetric capacity of 28 gm/L at 298 K amongst all.

The sorption capacity did not vary much with tube chirality at 298 K. Sorption capacity of (12, 12) tube at 100 atm, 298 K was 3.39 total wt% compared to 3.51 total wt% for (21, 0) tube under similar condition. However at 77 K, (21,0) tube adsorbed higher amount compared to the (12, 12) tube having similar diameter and cross linker distance. For example (12, 12) tube adsorb 8.29 total wt% at 40 atm, 77 K compared to 10.67 total wt% for (21,0) tube under similar condition. This difference becomes higher at high pressure. At 100 atm, 77 K (12, 12) tube

adsorb 9.57 total wt% compared to 11.32 total wt% for (21,0) tube under similar condition. Thus it seems tube chirality may have some effect at lower temperature but seem not important at higher temperature. However, the specific reason for this difference needs further investigation.

The higher sorption capacity at 77 K corroborates with figures reported by other researchers.[19,20] A total capacity of 11.2 wt% at 10 MPa (100 bar), 77 K with tube diameter 22 Å and inter-tube spacing of 11 Å was reported by others.[20] The tube diameter and spacing reported by Darkrim and Levesque quite similar to our 24 Å tube diameter and 11Å tube spacing of (18,18) tube scaffold. Their reported adsorption capacities also agree with our values.

4.3 Impact of tube diameter and linker spacing on sorption capacity

Fig. 4.3 summarizes the results presented in Fig. 4.2 and it shows that tube increasing diameter and linker spacing improves sorption capacity at higher pressures.
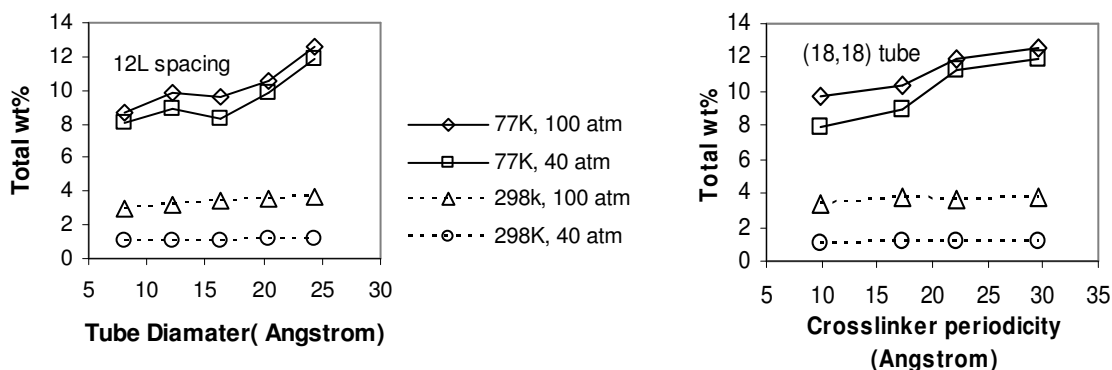

Fig. 4.3 Sorption capacity variation with tube diameter and inter-linker

These observations are explained as follows. For smaller diameter tubes, the van der Waals potential from opposite tube inner surface walls overlaps to create energetically favorable

location. However narrow tubes only allow a very thin column of sorbate molecules inside the tubes. Whereas larger diameter tubes allow a much thicker layer of hydrogen molecules, even though these interaction sites have lower energy compared to narrower tubes (illustrated in section 3.6). Thus larger availability of free space volume within the large diameter tubes favors adsorption capacity at higher pressure (loading).

Similarly higher linker frequency also reduces the available volume within the confines of the outer surface of the tubes and the linkers. This is because each linker occupies space and higher linker frequency (and lower inter-linker distance) leave smaller volume for the adsorption and reduce hydrogen diffusion due to stearic hindrance. Therefore it seems that adsorption capacity increases with free space volume within the scaffolds. We call these as "volume effects".

4.4   Sorption capacity of capped tube

Carbon nanotubes that are produced in laboratories in normal production process are generally capped at the ends. This means the inner tube surfaces are not accessible to sorbate molecules unless these tubes are uncapped by special treatment. Such exclusion of the interior of tubes reduces the sorption capacity by almost half. For example, the excess capacity for the open (18,18) tube is 10.33 wt% at 77 K at 40 atm, whereas it is only 6.30 wt% for the tubes when the interior volume is prohibited under the same loading conditions. This difference is more pronounced for larger (18,18) tube scaffold compared to (12,12) tube scaffold. This is because a large diameter tube allows a larger surface inside the tubes compared to the space outside the tubes. Therefore, for large tubes, when sorption inside the tubes are excluded, then sorption capacity reduces more pronouncedly from that of the uncapped tubes. The interior volume is also larger for bigger diameter tubes. This means two things. Firstly, the inner free volume is an

important factor towards higher sorption capacity. Secondly, to have high sorption capacity open tube scaffolds are necessary. Thus all other simulations and analysis were conducted with the open tube scaffold models.

4.5   Thermodynamics of adsorption: isosteric heat

When a gas molecule is adsorbed on the surface, some amount of heat is released. This is called isosteric heat of adsorption (q_{st}). This is a measure of the strength of the interaction between sorbate and sorbet/substrate molecules. Therefore a higher isosteric heat indicates a stronger van der Waals interaction between the sorbate and surface molecules, and therefore a greater adsorption capacity. Isosteric heat influences adsorption equillibria, kinetics and overall sorption process.[219] Thus it is important to study variation of q_{st}. The computed value of q_{st} for these scaffolds lie in the range of 0.88 to 2.14 kcal/mole. These values are comparable with reported values for other carbonaceous materials.[19,90]

The sorption dynamics have been explained to clarify how isosteric heat varies with loading (hydrogen sorption).[219] Isosteric heat may vary in different manner depending on the nature of interaction. These phenomena can be classified as follows:

1.   A constant q_{st} with increasing loading shows absence of sorbet-sorbet interaction, so that the q_{st} does not change even though more sorbate molecules are added. This also shows that the substrate is energetically homogeneous, which means there are no special location on the substrate surface that have higher q_{st} to encourage preferential adsorption.

2. An increase in q_{st} with loading indicates sorbent-sorbent van der Waals interaction (at the attractive range) at high loading.[219]

3. A gradual decrease in q_{st} with loading happens due to energetic heterogeneity of the surface. Once all the adsorption locations on the substrate which has higher q_{st} gets filled up, then only low q_{st} sites are available for further loading, showing a falling q_{st} trend.

4. Another case may be an initial increase followed by a decrease in q_{st} with increasing loading. In this case, q_{st} initially increases due to sorbet-sorbet van der Waals interaction (when within the attractive range), but as more sorbate is added to the system under high pressure and temperature, sorbate-sorbate repulsion comes to play to deteriorate the adsorption phenomenon.

All these phenomena were observed in our sorption studies. Behavior of q_{st} with various loadings for the (n,n) and (21, 0)-tubes with the same 12L cross linker spacing at 298 K is shown in Fig. 4.4.
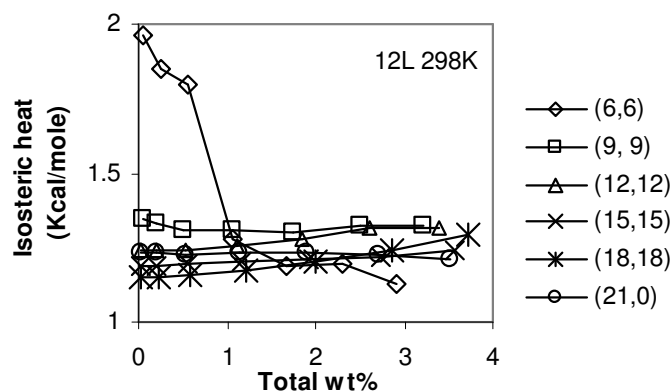

Fig. 4.4 Variation of isosteric heat with total wt % at 298 K

As observed in Fig. 4.4, q_{st} is almost constant at different loading for all the scaffolds except for the (6,6) nanotube based one. For the (6,6) tube scaffold, at low loading, the initial q_{st} is quite high and it decreases with loading up to a certain point. Later as loading increases the q_{st} becomes flat similar to the behavior observed for other tubes. This observation is explained as follows. For (6,6) tube, the tube diameter is small and thus, as explained before, this lead to superposition of the attractive van der Waals interactions from both sides of the tube wall on the hydrogen molecules in the proximity of tube surfaces. For these adsorption sites the sorbent-substrate interaction potential is strong which results in a high q_{st}. At low gas pressure or low loading, this tube wall potential dominates,[18] because sorbent molecules first gets adsorbed in these sites. As loading increases, all these sites get filled up, and the sorbent molecules then get accommodated to outer surface adsorption sites, where the potential field is weak and q_{st} is uniformly low.

In case of other armchair tubes and the zigzag tube (21,0) the q_{st} trend remains flat with increased loading. This indicates an energetically homogeneous substrate and absence of sorbate-sorbate interaction. At 298 K since the loading is still low compared to saturation loading, the gas molecules are farther apart and are not interacting with each other showing no change in q_{st}.

Fig. 4.5a shows that, at low (1 atm) pressure, as the tube diameter increases, the q_{st} decreases. For every point in the inner surface of the tube, there is an overlap of potential from other neighboring points on the inner tube surface. This curvature effect is greater for higher curvature tubes (smaller diameter means greater curvature).[220] For outer tube surface, an opposite kind of curvature effect is manifested because the potential overlap decreases with increased curvature (smaller diameters). Both curvature effects are evident only at lower pressures. At higher

pressures, other effects (e.g. volume effect) dominate to increase the adsorption capacity as the tube diameter increases. Whereas, the isosteric heat does not change much with linker periodicity as expected (Fig. 4.5b), because linkers do not create large number of high interaction sites. This will be evident in the next section.
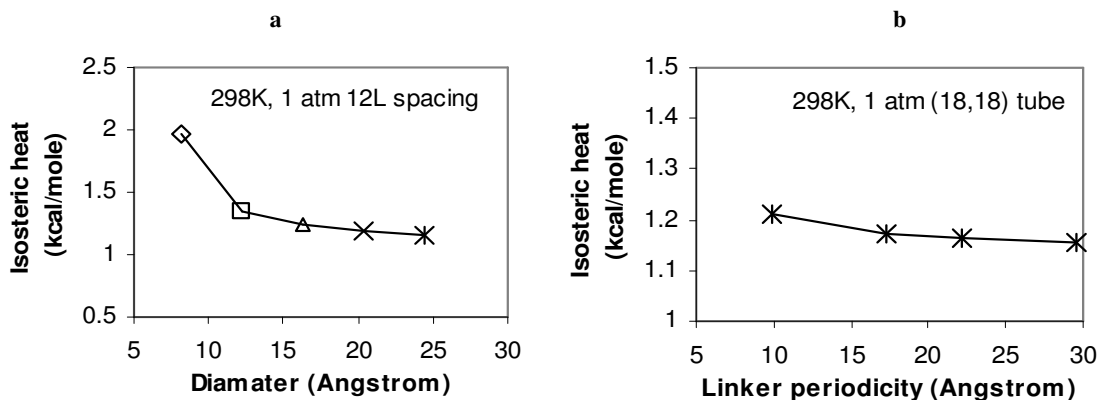

Fig. 4.5 Variation of isosteric heat with tube diameter and linker distance at 298 K

Behavior of the isosteric heat for the scaffolds at 77 K is presented in Fig. 4.6. The curves do not display a consistent pattern or trend. In the case of (6,6) tubes, q_{st} initially decreases with loading then increases. This indicates a three stage sorption loading phenomenon. These three stages are: 1) initial adsorption at the higher energy adsorption sites possibly at the inner tube surfaces; 2) followed by adsorption at the next available sites that have low adsorption energy which shows decrease in q_{st}; and 3) lastly, as all the sites get populated with more and more sorbate molecules under higher pressure, there is higher sorbate-sorbate interactions which increases q_{st}.
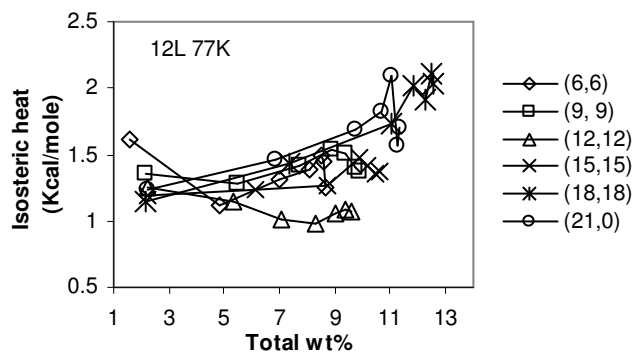
Fig. 4.6 Variation of isosteric heat with total wt % at 77 K

For (12,12) tubes q_{st} gradually decreases with increase of loading. This type of trend indicates energetically heterogeneous surface, i.e. higher energy sites get populated first followed by lower energy sites. Whereas, for (18,18) and (21,0) tube, q_{st} increases with loading indicating sorbate-sorbate interactions at high loading. This results also show a difference in trend for tubes with different chirality, such as (12, 12) and (21,0) tubes having similar diameter and crosslinker spacing. It may be recalled that at 77 K, (21,0) tube has higher sorption capacity compared to (12, 12) tube although they have similar diameter and linker spacing. This higher capacity may have contributed to sorbate-sorbate lateral interaction and thus high isosteric heat for (21,0) tube.

Fig. 4.7a shows variations of q_{st} with diameter. The trend is the same as in case of 298 K due to similar reasons as explained earlier. Similarly, the isosteric heat also remains flat with variation in linker periodicity (Fig. 4.7b).
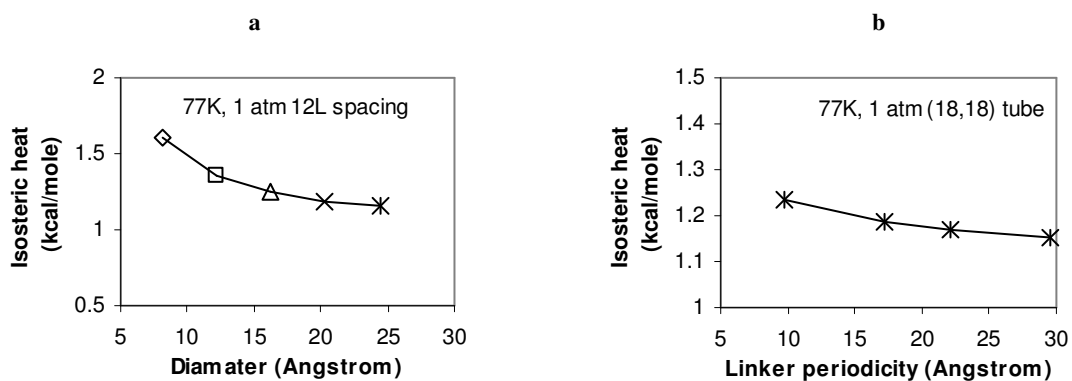
a

b

Fig. 4.7 Variation of isosteric heat with tube diameter and linker distance at 77 K

4.6   Physical distribution of adsorbates

The mass density plot and snap shot of physical distribution of hydrogen adsorbate inside the scaffolds confirm the insights presented in the previous section. Figure 4.8 and 4.9 show the mass density plots of hydrogen adsorbate molecules superimposed on the scaffold structures. A mass density plot gives the position of center of mass of each sorbate molecule in the framework as their positions were sampled. The red dots represent the high interaction (higher q_{st}) zones, while the blue dots represent low interaction areas, and yellow through green zones have intermediate q_{st} values. The high interaction sites have higher preference for adsorption and are occupied first.

a: Top view **b: Side view** **c: Bare scaffold**

High interaction

Medium interaction outside tube wall

High interaction near linker

High interaction inside tube wall
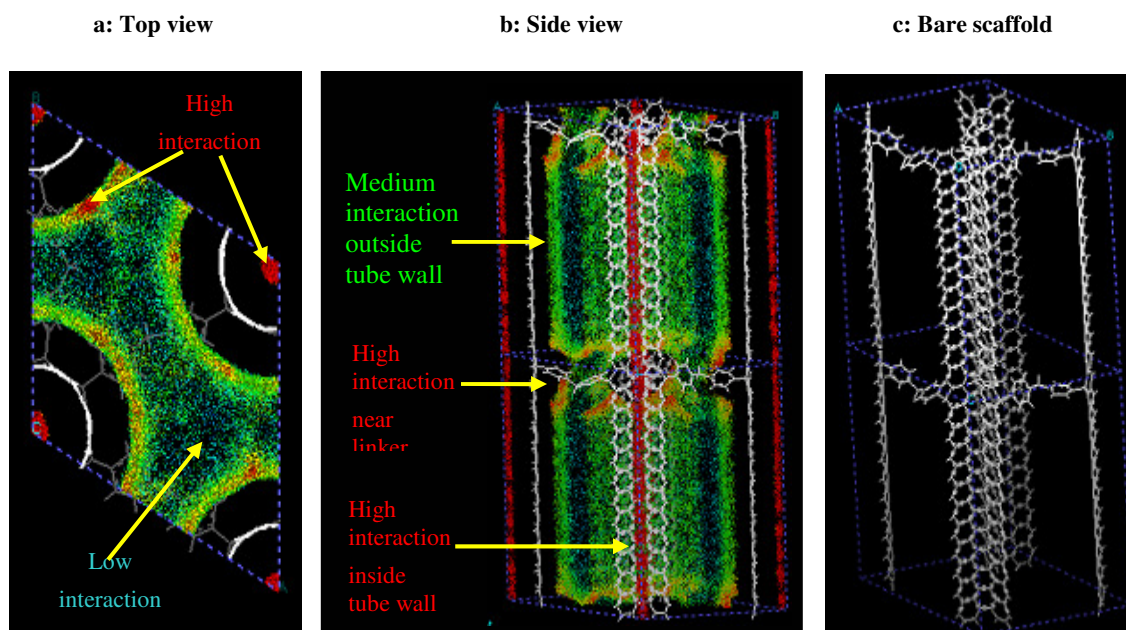
Low interaction

Fig. 4.8   Distribution of hydrogen molecules in the (6,6) 12L at 1 atm, 77 K

Fig. 4.8a and Fig. 4.8b show the top view and side view, of the mass density plot in the case of

(6, 6), 12L scaffold at 77 K, 1 atm. Figure 4.8c shows the side view of the empty (6, 6), 12L

scaffold structure to help interpret the side view shown in Fig. 4.8b. Figure 1 shows the top view

of H_2 mass density plot for (18, 18) 12L scaffold at same temperature and pressure. There are

several observations to be made from these figures. From Fig. 4.8a and Fig. 4.8b, it is evident

that the adsorption location of hydrogen molecules inside the (6, 6) tube is confined to a very

narrow column (red and yellow color). This column is shown as a small red circles in the top

view (Fig. 4.8a) and a red-yellow elongated tube from the side view (Fig. 4.8b). For bigger

diameter scaffold, for example in (18, 18), this column is much thicker (bigger red-yellow circles

in Fig. 4.9). This shows that bigger diameter tubes allow larger adsorption volume (i.e. the

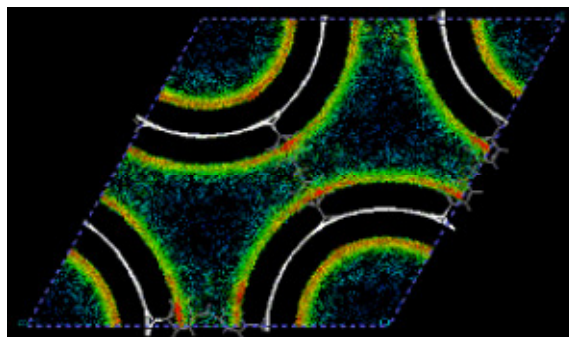volume effect) as mentioned in section 3.3.

Fig. 4.9 The mass distribution of hydrogen molecules in the (18,18)

The red, yellow and dense green marked locations in Fig. 4.8a, Fig. 4.8b, and Fig. 4.9, shows the high energy interaction sites in the immediate vicinity of: (1) inner, (2) outer tube surfaces, (3) near the locations where the linkers are attached on tube external surfaces and (4) all around the linkers. The dark locations show the volumes where there are no adsorption sites. These are generally the spaces which are taken up by the carbon atoms and linker molecules. It is evident from these figures that linkers create only a small amount of high interaction sites compared to the tube surfaces. It is also evident that the linkers take up significant space; which means, the larger linker densities (smaller inter-linker distances) will leave lesser space for the adsorption locations and will cause lower adsorption as mentioned in section 4.3.

4.7   Sorption capacity, surface area and inter-linker distance

As adsorption is a surface phenomenon, it is naturally expected that the adsorption capacity should increase with surface area. With such expectations, other researchers[221] suggested that typical activated carbon material achieve ~1 wt% for every 500 m^2/gm by for a pressure range of 30-50 atm. For CNT scaffolds, a capacity of 3.7 wt % for 1000 m^2/gm at 77 K at 2 bar was suggested.[17] For comparison, here we present the sorption capacities and specific surface areas

for different scaffolds at 1 atm and 40 atm for 77 K and 298 K. However, in real scaffolds, some other factors may come into play to conceal a positive correlation between surface area and adsorption capacity.

The open tube scaffolds have surface areas in the range of 2188 to 2781 m^2/gm. Total sorption capacities of these scaffolds at 77 K, 1 atm are in range of 1.22% to 2.44 wt%. At 298 K, 1 atm these numbers are between 0.018 to 0.06 wt%, at 77 K, 40 atm they are between 5.01 to 11.86 wt% and at 298 K, 40 atm the values are within 0.77 to 1.21 wt%. For the (18,18) tube scaffold, where the sorption to interior regions is prohibited, the surface area was around 1500 m^2/gm and this scaffold showed a total sorption capacity of 1.22 wt% at 77 K 1 atm. This is less than the capacity of ~3.7 wt% for 1000 m^2/gm at 77 K, 2 atm., as suggested by others.[17] A higher capacity is observed in their experiments compared to our simulations. This is perhaps due to the influence of impurities present in the experimental samples. In comparison, our simulations consider pristine structures and ideal behaviors.

To show the relationship between sorption, surface area and cross linker periodicity of open tubes scaffolds, these metrics are presented in Fig. 4.10.
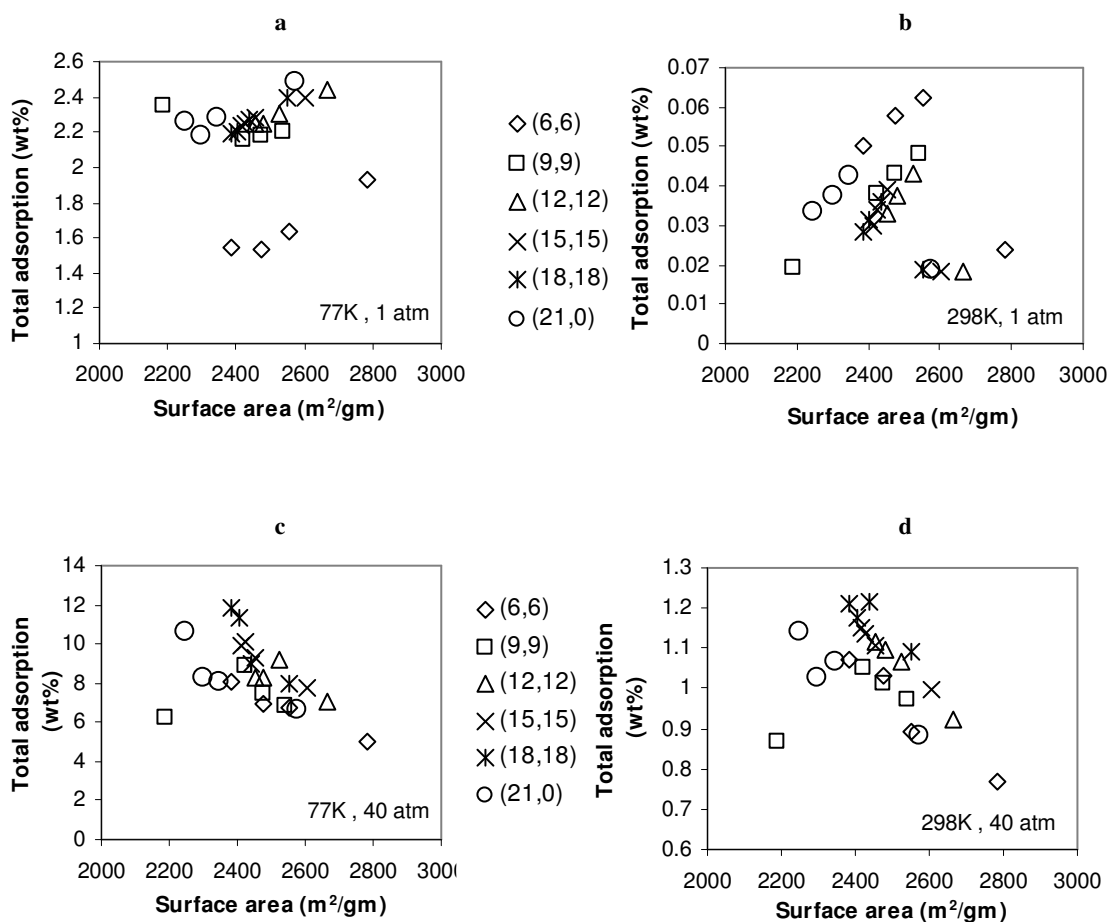
Fig. 4.10 The sorption capacity vs. specific surface area at 77K, 298K, 1 atm and 40 atm

From Fig. 4.10, we make the following key observations. First, in general, the smaller tube scaffolds show lower capacity than others because the smaller tubes allow only limited amount of sorbate molecules within the tubes due to limited tube volume (the "volume effect").

The second observation is that at lower (1 atm.) pressure the sorption capacities increases with increase of specific surface areas, but opposite is true at higher (40 atm) pressure. It seems that availability of more surface area favors sorption capacity at lower pressure ranges (e.g. at 1 atm), but other factor(s) dominates at higher pressure ranges (e.g. 40 atm). The volume effect and

stearic hindrances, as elucidated in section 3.3, can explain why capacity and surface areas are negatively correlated at high pressure. Higher linker frequency decreases free volume and increase stearic hindrance. On the other hand, higher linker frequency (with lower inter-linker distance) scaffolds have higher specific surface area (refer Table 4.1 in section 4.1). Therefore it is only natural that sorption capacity and specific surface areas will be negatively correlated.

4.8   Effect of different functional group

Covalent functionalization of tube surfaces in SWNT by using aryl diazonium chemistry, leads to various beneficial properties.[90] For example, the isostearic heat may be manipulated by attaching functional groups. For example chlorobenzene was attached to the tube wall to create space between the tubes and keep them separated, while reducing linker density (which improves the volume effect).[17] With this approach they reported an increase in porosity and sorption capacity. Thus, we were motivated to assess the real benefits of tube surface functionalization on sorption capacity. This is because we suspect that other factors might have contributed to the increase in sorption, rather than the tube surface functionalization alone. In that experiment[17] sulfuric acid (oleum) in the preparation process, hence there is a possibility that some sulfonate groups may be present in the tubes which improved sorption capacity. This hypothesis is supported by a report on the beneficial effect of sulfonate group on gas storage capacity.[72]

To asses the benefits of functionalization, we attached various kinds of groups on the tube outer surface and assess their effect on sorption capacity. At this point onwards, we choose to only study the (12, 12), and (18, 18) tube scaffolds for the reasons stated earlier in section 2.3.

Fig. 4.11a gives the schematic representation of various functional groups used in our study and Fig. 4.11b displays a scaffold model where additional functionality is present.
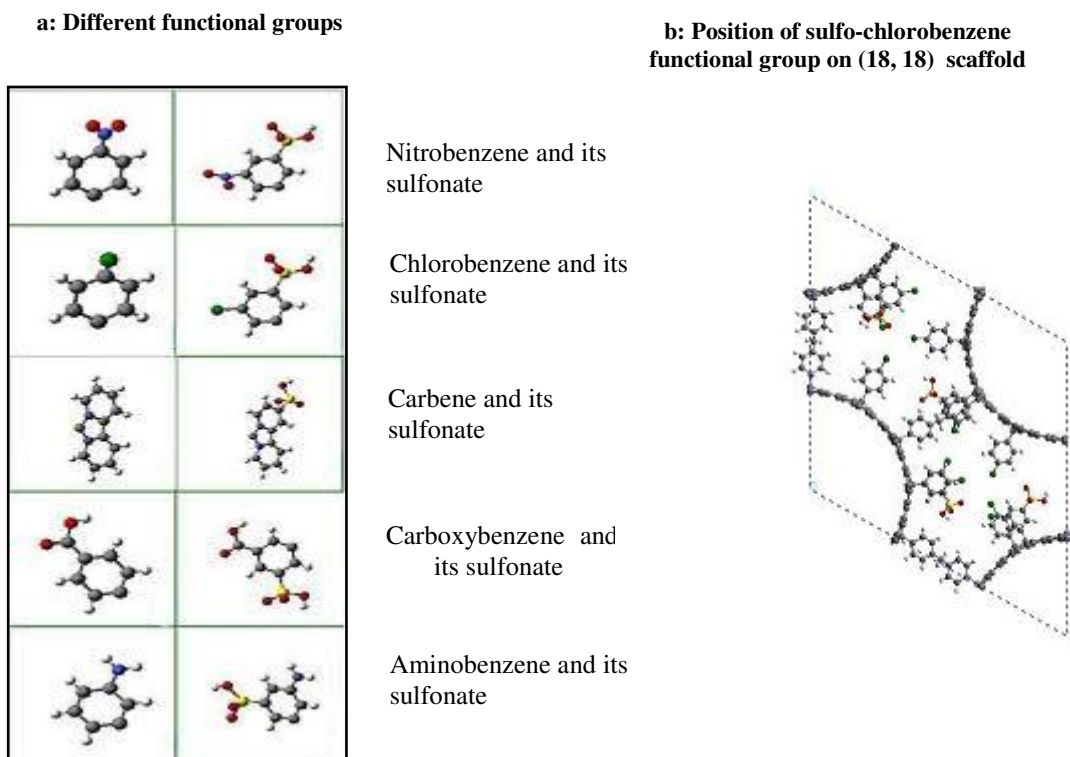
a: Different functional groups

**b: Position of sulfo-chlorobenzene
functional group on (18, 18) scaffold**

Nitrobenzene and its
sulfonate

Chlorobenzene and its
sulfonate

Carbene and its
sulfonate

Carboxybenzene and
its sulfonate

Aminobenzene and its
sulfonate

Fig. 4.11 Different functional groups for decorating carbon nanotube scaffold

Fig. 4.12 presents adsorption capacities of these scaffolds for various pressures at 77 K and 298 K temperatures. We observed that with the incorporation of different functional groups, both, volumetric adsorption and the total adsorption capacity wt% decreased. Although presence of additional function groups increases the surface area, they reduce the available volume of the scaffolds, and thus reduce sorption capacity.
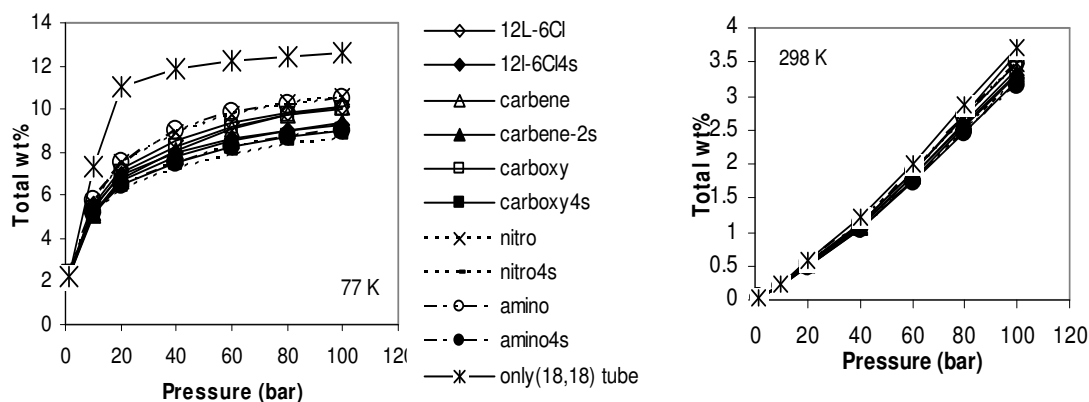
Fig. 4.12 Effect of covalent functionality on sorption capacity of (18,18), 12L

Presence of functional groups does impart some charges to the tube walls and improves isosteric heat, however this charge is very small. This is not sufficient to compensate for the stearic hindrance induced loss in volume due to presence of the functional groups on the tube walls. Thus, we contend that the experimental observations of sorption capacity increase by functionalization is primarily due to physical separation created by the functional groups and perhaps also due to residual sulphonates.

4.9   Impact of Li^{+1} on the tube wall

Li incorporation on carbon materials improved their hydrogen sorption capacity.[24-26] Li improves sorption capacity by imparting charge to the tubes and thus increases the interaction energy. To study this behavior on scaffolds, we performed simulations with 100, 120, 150 Li^{+1} ions per unit cell, placed on the outer side of the tube walls for (12, 12) and (18, 18) tube scaffolds where the amounts have a Li:C ratio similar to 1:9, 1:7.5 and 1:6.

Fig. 4.13, shows the space-filling model of Li decorated (18, 18) tube scaffold. Here, the Li^{+1} are the pink colored spheres. After energy minimization, Li^{+1} have almost vertical alignment along

the tube wall. As the number of Li increases, the compensating charge on the tube also increases (becomes more negative). For example, 150 Li^{+1} decorated tubes carry ~ -0.1625e charge, 100 Li^{+1} decorated tubes carry ~ -0.1094 e charge compared to the ~-0.0012e charge when no Li^{+1} is present. The presence of Li^{+1} has two different impacts. The presence of Li^{+1} increase the van der Waals interaction. In addition, the static charges result in preferable strongly binding Columbic interactions between tube and sorbate molecules,[222] i.e. quadruple moment of hydrogen molecule – negatively charged tube-atoms interactions are very effective in attracting more hydrogen.[222] Both these effects increase the interaction energy q_{st} to increase the adsorption and form more dense sorbate layers around the scaffold.
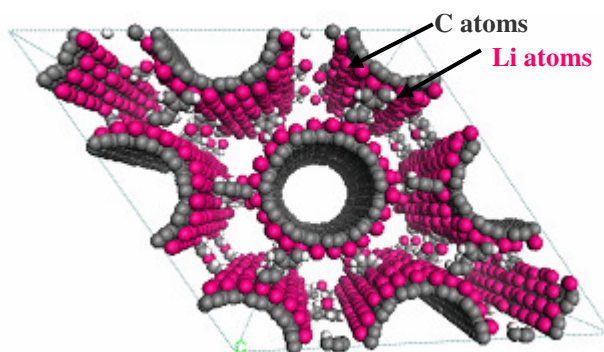

Fig. 4.13   Li $^{+1}$ decorated scaffold with (18,18), 12L nanotubes

Increase in interaction energy is evident from the mass density plots displayed in Figure 4.14 which compares hydrogen molecule densities around the (18, 18), 12L scaffolds with and without the decorating Li atoms.
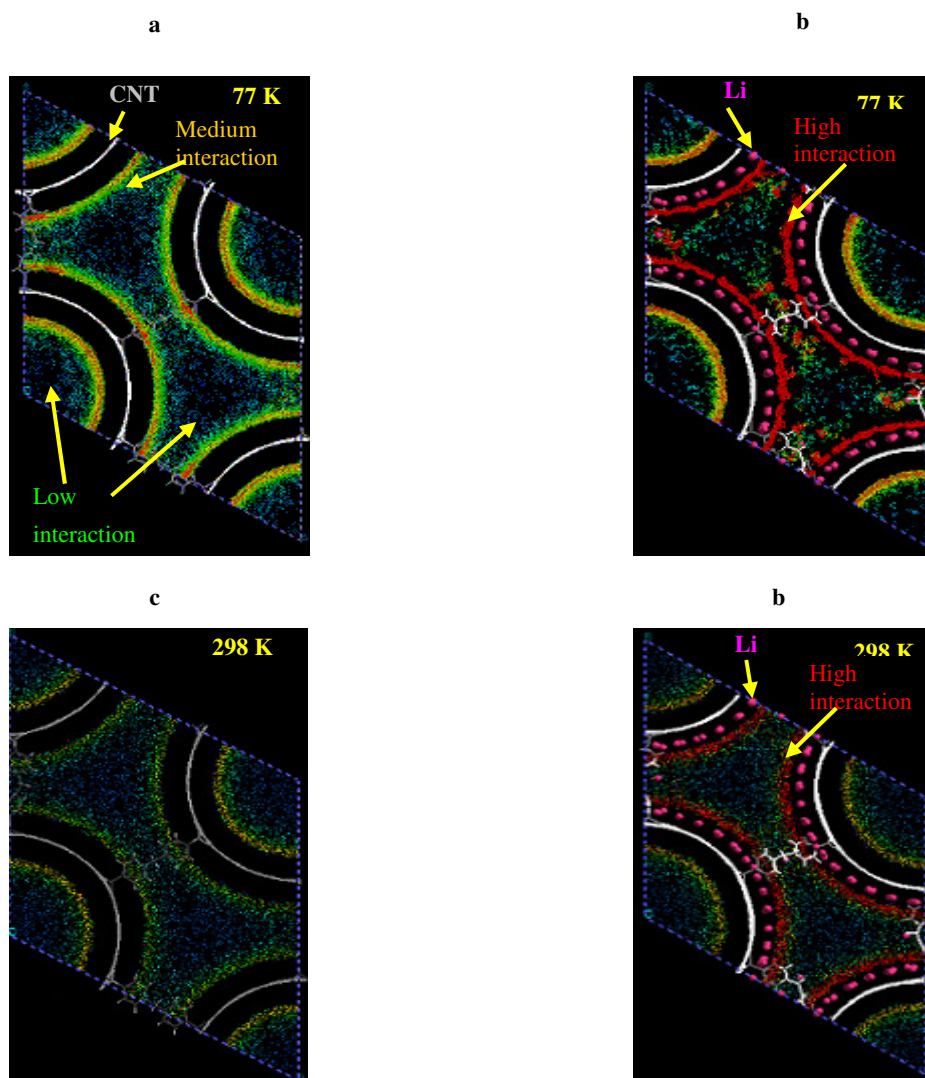
Fig. 4.14 Mass density plot for (18,18), 12L with and without Li

Fig. 4.14a is for the scaffold without Li at 77 K 1 atm and Fig. 4.14b is with Li at same temperature and pressure. Whereas, Fig. 4.14c is without Li at 298 K 1 atm and Fig. 4.14d is with Li at same condition. Fig. 4.14b and Fig. 4.14d shows that when Li atoms are present on the tube outer surface, there is a thicker high interaction zone, shown in red color, near the Li atoms.

Fig. 4.15 shows the impact of Li^{+1} on sorption capacity by comparing sorption capacities for scaffolds with and without Li^{+1}. Fig. 4.15a shows that, the scaffolds with Li^{+1} has higher total capacity at 77 K at lower pressure range (below 6 atm), but a lower capacity at higher pressure range (above 6 atm). The volumetric capacities (not shown in figure) also show the same pattern. This is because when incorporation of Li reduces the available volume but increases interaction potential and surface area. At lower pressures, when the volume effects do not dominate, the higher surface area leads to higher capacity. At higher pressures, when the volume effect dominates, the capacity suffers when Li is present. This is because the molecular weight M of the Li decorated substrate has increased significantly lowering the excess adsorption capacity wt% ratio.
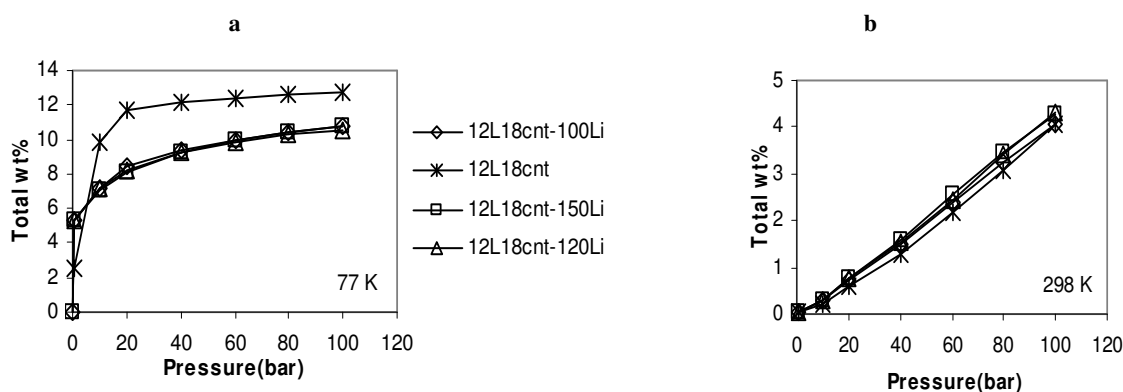
Fig. 4.15   Total capacity of Li^{+1}decorated scaffolds at: a) 77 K, b) 298 K

Fig. 4.15b shows that at 298 K, Li incorporation substantially improved the adsorption capacities. The scaffold with Li decorated (12, 12) tubes shows less capacity than that for the (18,18) tube.

We found that the optimum Li:C ratio was 1:6 (i.e. 150 Li atoms per cell). At 298 K, the 150 Li^{+1} atom decorated tube achieved excess capacity 3.39 wt% (total capacity 4.26 wt %) at 100

atm with q_{st} being 1.77 kcal/mole compared to bare tube excess capacity of 2.99 wt% (total capacity 4.04 wt%) and q_{st} of 1.258 kcal/mole at the same condition. The q_{st} of the 150 Li decorated tube at 77 K, 1 atm is 2.68 kcal/mole (11.213 kJ/mole) and at 298 K, 1 atm it is 1.98 kcal/mole (8.29 kJ/mole) compared to the 1.18 kcal/mole (4.93 kJ/mole) for the bare tube at both of these conditions. These values of q_{st} of Li decorated tubes and also empty tubes corroborates well with other reported values. For example, for a MOF system,[79] Li-H binding energy was found to be in the range of 12-18 kJ/mole and for a Li decorated graphene sheet,[37] the binding energy was ~13 kJ/mole. The hydrogen binding energy on a simple benzene molecule or graphene sheet is in the order of ~5 kJ/mole.[79,223] These values are similar to our calculated values.

The behavior of the isosteric heat curve against excess weight % for Li decorated scaffolds (Fig. 4.16) show two distinct patterns at two different temperatures: 77 K and 298 K. At 77 K, when Li is present, q_{st} decreases sharply with increase in loading, whereas for the bare tube without Li, the q_{st} increases with gas loading. As Li creates a very high interaction potential near the tube wall, thus at low loading (and low pressure), the sorption capacity and q_{st} both are twice as big compared to the values for bare tubes. This drastic reduction in q_{st} represents energetically heterogeneous substrate and no sorbate-sorbate interaction, as explained in section 4.5. Li incorporation creates this heterogeneity with locations of high energy sites and low energy sites. Once the higher energy sites are filled at low pressure the remaining low energy sites are filled at higher pressure. At 298 K the sites are energetically more homogeneous as represented by the almost flat lines for q_{st} with increased loading. But Li decorated scaffolds have higher q_{st} than bare scaffolds.
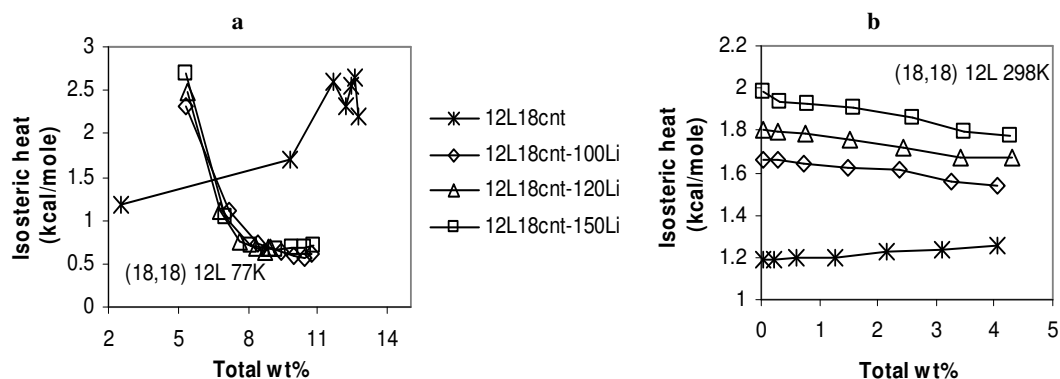
Fig. 4.16 Isosteric heat of Li+1 decorated (18, 18) scaffold at 77 K and 298 K

There is an important phenomena in some of the Li decorated structures. In some structures, as mentioned in various studies,[24,223,224] there is clustering of Li atoms and formation of LiH. Although we do not see such phenomena in our simulation, but this is discussed in details in the following paragraphs for clarification of certain issues.

We used Monte-Carlo simulation with empirical forcefield to model the equilibrium sorption behavior of scaffold structures. Whereas others[24,223] used DFT method which is based on quantum calculation on electronic structure on a much smaller number of atoms. Use of DFT has enabled them to capture the Li clustering and metal-hydride formation phenomena. On the other hand in our Monte Carlo simulation, the Dreiding forcefield which we used, is not equipped to capture the atomic reaction (metal-hydride) phenomena, thus we can not directly comment on formation of metal-hydride in our structure. However, based on the available literature, we can make some relevant observations which will give some insight on whether there may be metal hydride formation phenomena in our structure or not. These are presented below.

There are quite a few studies,[24,25,79,223,224] which commented on the optimum Li:C ratio (Li density) in carbon nano structures, based on minimum total energy of the structure, number of Li

aggregate formation, highest hydrogen binding, etc. Different optimum ratios have been reported, which are between 1:3 to 1:18, but most of them reported the optimum Li:C ratio to be around 1:6. Lithium graphite intercalated compounds having various Li concentrations (Li:C as 1:6 to 1:18) also have been prepared experimentally.[225] These indicate two things. Firstly, these studies show that it is possible to prepare Li decorated CNT with Li:C ratio of 1:6. Secondly, different studies have found different optimum ratios, which may be attributed to the difference associated with the substrate molecular structure.

For example, the researchers[223] who did a DFT calculation on co-intercalation of Li and small organic molecule on graphite, reported that a maximum Li containing graphite intercalated compound that they could prepare without Li clustering was of $Li_4(THF)C_{72}$ (where Li:C ratio was 1:18). They found that at high Li ratios, there was a tendency to form Li clustering and Li-hydride formation. According to them, when the bond distance between Li atoms are around 2.8 Å, that indicates occurrence of Li clustering. Such Li clustering will eventually lead to Li-hydride formation in their structure. On the other hand, a Li:C ratio of 1:8 without any Li^{+1} clustering was used by researchers[24] who studied hydrogen storage in Li dispersed carbon nanotube using DFT method. Moreover others[224] who performed DFT calculation on Li coated Fullerene, found a optimum Li:C ratio of 1:5 without Li clustering. Therefore it seems that optimum Li:C ratio depends on the particular structure and it is not an universal ratio. The notion of "high Li density" (expressed as Li:C ratio) which leads to hydride formation may be dependent on the particular structure and its chemical environment. Thus it is possible that a particular Li:C ratio that is considered high for one structure (leading to hydride formation) may not be high enough to lead to a similar phenomenon in another structure. Thus the ratio of 1:6 may not be necessarily considered as high enough in our CNT scaffolds to form metal-hydride.

Furthermore, in our study, we found the optimum Li:C ratio to be 1:6 (150 Li), above which we observed a decrease in sorption capacity. In case of 150 Li-decorated scaffold (Li:C ratio 1:6), we observed that the average Li-Li distance was 4.81 Å (shortest being 2.66 Å observed for few cases of Li atoms. This shortest distance is similar to the bond distance in a Li_2 molecule,[224] which may indicate limited amount of Li clustering.. However this necessarily does not indicate metal hydride formation. The reason is explained below.

In our study, the minimum Li-H distance was ~3.4 Å which is larger than the Li-H bond distance for a LiH molecule (~1.61 Å).[224] Hydrogen was in the molecular form and the bond distance between hydrogen atoms were maintained at 0.74Å. In several studies[24,25,79,223,224] it has been observed that hydrogen binds as a molecular form on Li intercalated or Li decorated structures. Thus even though there is a limitation in our simulation method, but we still believe that the hydrogen is adsorbed in the molecular form and there is no hydride formation. However this needs further investigation.

4.10   Sorption capacity at 243 K

DOE target was already achieved by bare scaffolds at 77 K. So next we wanted to verify whether presence of Li^{+1} may improve the sorption capacity and help move towards the achievement of the DOE target. We conducted a sorption study for the (18, 18), 12L tube scaffold with 150 Li atoms with stoichiometry LiC_6, to see the sorption capacity at 243 K (-30 ^{0}C) which is the lowest temperature DOE target. For this study we have increased the van der Waals interaction cutoff to 15 Å. This scaffold achieves 5.84 total wt% at 100 bar (Fig. 4.17).
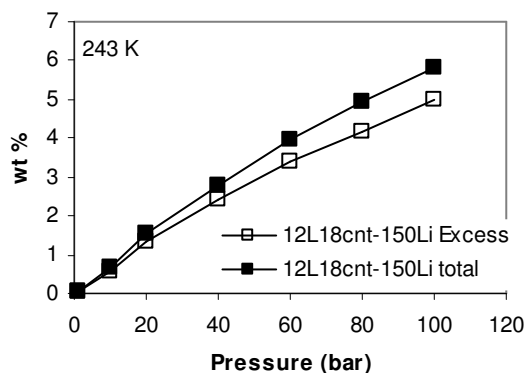
Fig. 4.17 Sorption capacity at 243 K

We prepared two more (18,18) tube scaffolds with: 1) 200 Li placed outside surface of the tube wall, and 2) in another case 150 Li at the outside surface and 50 Li at the inside surface of the tube. However this high amount of Li did not increase sorption capacity but decreased it. So we considered the (18, 18), 12L tube with 150 Li (Li:C ratio of 1.6) to be the optimum. For this scaffold the system volumetric capacity reached 35.7 gm/L, which is an improvement over the bare tubes (28.8 gm/L). But this is lower than the DOE target (45 gm/L).

4.11   Summary

Efficient storage of hydrogen is one key challenge for hydrogen economy. Carbon nanotubes are considered as potential hydrogen storage materials because they have large surface area and high adsorption capacities. However, single wall carbon nanotubes bundle up tightly, so most of their surface areas become inaccessible for adsorption. One way to improve the sorption capacity of these carbon nanotubes, is to hold the tubes at distance from each other in a scaffolded structure, so that their external sorption surfaces become accessible to hydrogen molecules.

With a goal to improve the sorption capacities of such scaffolds, we analyze the effect of linker densities, tube diameter, carbon nanotube surface functionalization and Li decoration on sorption capacity. We studied sorption capacity of scaffolds with a range of volume and surface areas, using molecular dynamics and grand canonical Monte Carlo simulation. For these studies we prepared SWNT scaffolds that had different diameters and were covalently connected by methylene-di-aniline crosslinker after every 4th, 7th, 9th and 12th layers of benzene rings. The scaffolds with larger diameter tubes and wide linker spacing showed higher sorption capacities. At 77 K, several of these scaffolds achieved and exceed DOE gravimetric and volumetric hydrogen storage targets. We studied one zigzag tube as a test case and found that chirality may have some effect on sorption capacity at lower temperature (77 K), but has no effect at room temperature. This needs further investigation. We found that additional functionalizaton of the tube walls had detrimental affect on sorption capacity due to stearic hindrance and adsorption space reduction caused by bulky functional groups. On the other hand, incorporation of Li^{+1} ions on the outer tube surface increased sorption capacity by increasing the adsorption interaction energy. At 243 K, Li^{+1} incorporated (18,18), 12L scaffold reached a total capacity of 5.84 wt%. However actual performance of this Li^{+1} incorporated scaffold have to be experimentally measured in the laboratory to confirm this. Future studies may be conducted to see the effect of other transition metals in the scaffolds.

CHAPTER V

HIGH PRESSURE BEHAVIOR OF METAL ORGANIC FRAMEWORKS

In this chapter, we present the results obtained from our simulation studies on high pressure behavior and mechanical properties of certain MOF crystals. We begin by presenting some results to establish that the forcefield we choose is suitable for these simulation studies. Then, we present how these empty MOF crystals behave under high pressure. These are followed by our observations on hydrogen filled MOFs under similar high pressure and our analysis of the thermodynamics of the adsorption.

5.1   Behavior of empty MOF-5 crystal

5.1.1   Validation of the forcefield (UFF) for MOFs

Forcefield (UFF) validation was performed on MOF-5 structure. MOF-5 has a cubic crystal structure with experimental lattice parameter of 25.669 Å[27] (25.88 Å reported elsewhere[28]) at ambient condition. The energy minimized equilibrated structure obtained by us has a lattice parameter of 25.64 Å, which is very close to the experimental value reported by others.[27] Calculated density 0.69 gm/cc is in the same order of the experimentally observed density of 0.59 gm/cc of the evacuated crystal[27] and is also similar to the density theoretically calculated by others.[37,38,41] The values of some selected bond length and angles of the energy minimized equilibrated structure are given below. The calculated bond lengths for Zn–O and O-C was 1.922 Å and 1.305 Å respectively which is very similar to the experimentally observed value of 1.91 Å and 1.30 Å.[27] The calculated angles O-C-O, Zn -O- C and O-C-C are 125.0, 129.3 and 116.7 respectively which are also similar to the experimentally observed values[27] of 125.0 130.4

and 117.5 respectively. These show that the UFF is reasonably good to predict the crystal structure parameters.

5.1.2   Pressure-volume relationship

We conducted a detailed study on IRMOF-1 (MOF-5). The pressure-volume relationship of MOF-5 is given in Fig. 5.1a. The MOF crystal structure is stable upto ~250 MPa and phase transformation takes place at a higher pressure. After a threshold pressure (around 250 MPa, 298 K); the crystal rapidly collapses to a different crystalline structure. At low temperature (77 K) this threshold pressure is lower (200 MPa). This is probably because at low temperature the atoms possess less energy (k_BT). All further analysis was performed on the structures at 298 K since this is more relevant for practical application.
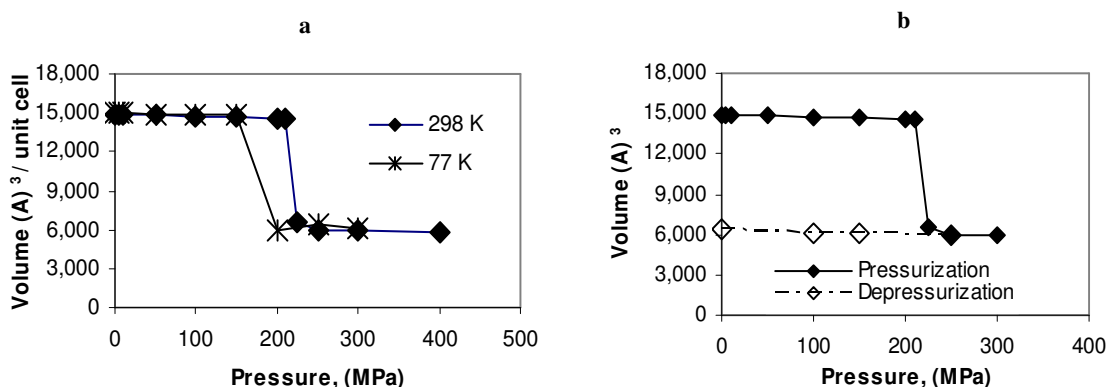

Fig. 5.1 Pressure-volume behavior of MOF-5 crystal structure at 77 K and 298 K

Structural transformation of empty MOF was found to be irreversible (Fig. 5.1b). The final structure obtained at 250 MPa was subjected to a reduced pressure, but the structure did not regain the original volume.

Similar high pressure deformation behavior was observed when shear stress was applied on YZ plane. In this case volume collapse happened at 500 MPa pressure. Similar to the observation in hydrostatic pressure, the deformation process was found to be irreversible.

5.1.3   Change in lattice parameters

Fig. 5.2a and Fig. 5.2b present the ball and stick diagram of original MOF-5 crystal and the deformed crystal (both in z axis projection) at high pressure (250 MPa) respectively. As observed, at high pressure the crystal gets deformed and compressed to about half of its initial volume and loses its cubic symmetry. There is a phase transition from cubic lattice structure at low pressure to triclinic lattice at high pressure. The density of original MOF-5 is around 0.69 gm/cc which increases to 1.6 gm/cc as the structure is deformed.
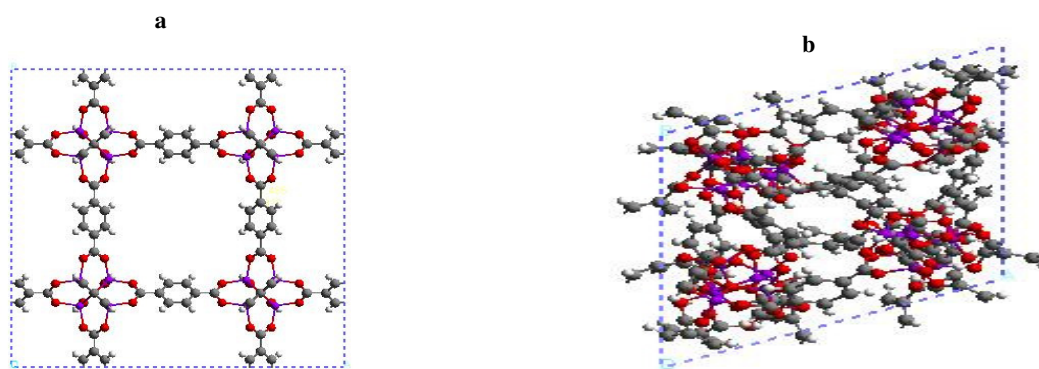

Fig. 5.2 Ball and stick representation of original and deformed MOF-5 crystal

During the deformation process at room temperature, the changes in the lattice parameters: a, b and the angles α, β are similar. But the major change happens in lattice parameter c and the angle γ (Fig. 5.3a & b). At 250 MPa, the lattice parameters are: a = 21.86 Å, b = 21.82 Å, c = 20.79 Å, $\alpha = 55.4^0$, $\beta = 55.4^0$ and $\gamma = 61.6^0$. A different structure emerges at even higher pressure (300 MPa), when the lattice parameters become: a = 22.34 Å, b = 22.24 Å, c = 22.2Å, $\alpha = 69.5\ 0$, β

= 63.5^0 and γ = 115.3^0 . At even higher pressure (400 MPa) this deformed structure is maintained.
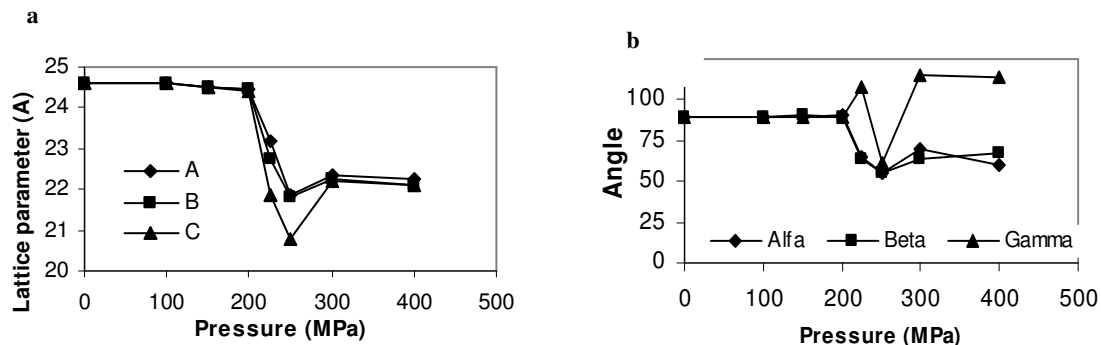

Fig. 5.3 Change in unit cell length and angle of MOF-5 crystal structure at 298K

Fig. 5.4 shows the simulated powder X Ray (PXRD) diffraction pattern of the original crystal structure at ambient condition and the deformed structure at 250 MPa. From the strong peak it is evident that the deformed structure is still a crystal. In the deformed structure, strong peaks are at (002), (020), (220), (202) planes appeared compared to the strong peaks in (200), (220), (400) planes in the original structure.
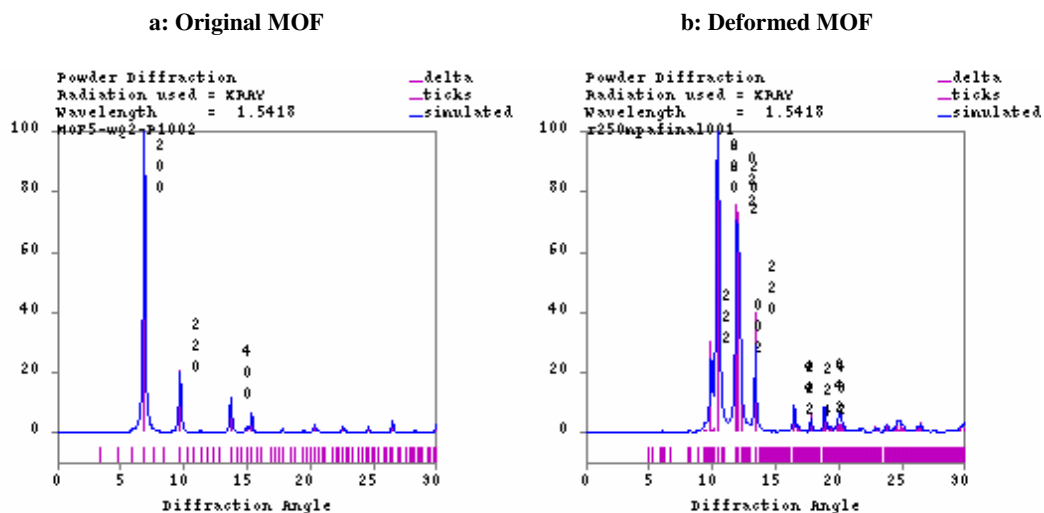

Fig. 5.4 Simulated powder X-ray diffraction pattern of MOF-5

The original and the deformed structures were analyzed by IR/RAMAN vibration mode analysis (data not shown). The peak at wave number 3000 which represents the vibration modes of C-H bond is similar in the original and the deformed structure. Similarly, the strong peak at wave number 1652, which is due to C-O stretch, is the same in both original and deformed structures. The peaks at softer modes between wave number 1 to 1000 have shortened and some of them disappeared in the deformed structure. The peak at wave number 562 in the original structure that represents the group vibration of the whole framework is shorter for the deformed structure. However the IR spectrum does not reveal any appearance or disappearance of strong peak. Therefore the deformation appears to be by reorganization of the linkers and ZnO_4 clusters.

Previous theoretical study also reported no structural instability over a pressure range of -0.5 to 0.5 GPa and the variation in lattice parameter is of the order of 0.46 Å/GPa in the same pressure range.[40] However, a recent experimental work on MOF-5 found that the MOF-5 sample undergoes amorphization at a pressure of 3.5 MPa.[110] The reason of the difference between the theoretical study and the experimental work may be explained as follows.

It is known that the real samples contain defects, grain boundaries, which may lead to inferior mechanical properties. Whereas the current theoretical simulation and the study in ref 15 deal with atomically clean crystal devoid of any defects thus gives result for an ideal situation. Thus the results of the theoretical study and the experimental observation are different. Secondly, MOF-5 is known to undergo decomposition upon exposure to atmosphere.[111] The MOF-5 sample used by the researchers[111] was prepared without exposure to air showed partial conversion to a new phase within 10 minutes exposure to atmospheric air. The sample in the experimental work[110] although was prepared without exposure to air; it is unclear if the 30 minutes compression experiment was also performed in the absence of air. Thirdly, it is not clear whether

the DAKE pressure machine used in the study[110] had an online X Ray diffraction machine as it is present in diamond anvil cell used in high pressure experiment for Cu-MOF and ZIF-8.[35,36] If not then the samples after compression test required further handing and transportation for the PXRD test which indicates further exposure to air, and thus further decomposition. All these may lead to a result different from the theoretical study.

However, there is a limitation of the forcefield used in the study. Universal forcefield is not equipped to capture crystal to amorphous transition which may involve bond breaking. Thus further study with appropriate forcefield is required to predict the transition from crystal to amorphous phase.

Therefore we conclude that the difference between the results of theoretical study and the experimental findings may arise to the fact that theoretical study assumes ideal conditions (unless the non ideality is explicitly taken into consideration) whereas experimental result depends on sample preparation, handling and measurement techniques. Next we explain the lattice transformation process that involves atomic rearrangement.

5.1.4   *Progression of lattice transformation*

The bulk modulus of MOF-5 under low pressure (calculated from our simulation) is 18.85 GPa and the C_{44} elastic constant is 1.254 GPa. These values are in good agreement with the values obtained from other theoretical and nanoindentation studies.[37-41] Other researchers have described MOF-5 as a soft, ductile material. Very small C_{44} elastic constant indicates that the original structure is almost on the verge of mechanical instability and shear strain along XY (YZ and XZ) are the major deformation modes. We observed that under hydrostatic pressure, the deformation progresses by shearing along a plane, resulting in extension in one direction and

compression in the other (Fig. 5.5). At 250 MPa, the corner to corner oxygen distance on the same face is 18.54 Å for one pair and 11.059 Å for the other pair, compared to 16.33 Å and 17.531 Å for energy minimized equilibrium structure under low pressure. Although the z axis projection of the deformed crystal gives an impression that the benzene rings are facing each other (refer Fig. 5.5b) but they are actually far apart (C-C distance between two carboxylate-carbon on two opposite linker are 12.088 Å and 10.065 Å for two different pairs). This also indicates that there is still open space within the structure.
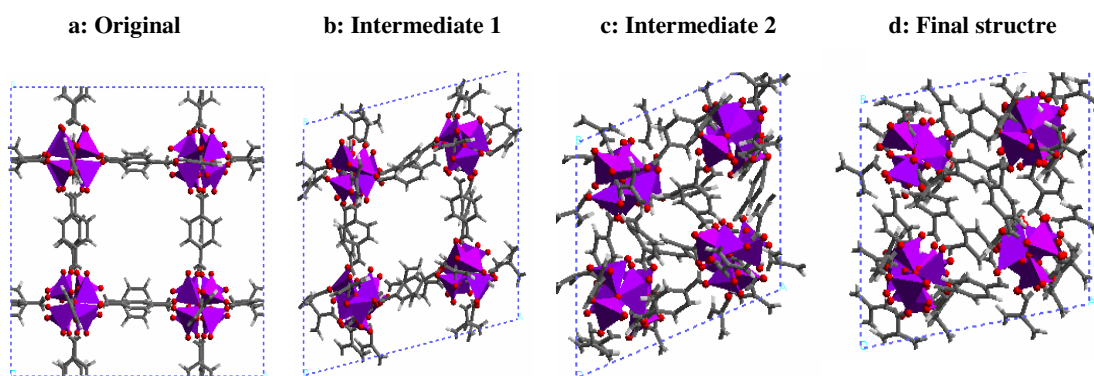
a: Original	b: Intermediate 1	c: Intermediate 2	d: Final structre

Fig. 5.5 Bond rearrangement progression by tetrahedral tilting and bond rearrangement

High pressure deformation and lattice change have been widely reported for other porous materials like zeolites.[42] Similar to zeolites, MOFs are composed of rigid unit modes (RUM) made up of the ZnO_4 clusters which can translate, rotate and reorient. These modes are connected by BDC linkers by a flexible hinges. Various previous studies[37-41] have reported that the connection between the organic linkers and the metal clusters are the weakest bonds in the MOF structure. Our molecular dynamic simulation also revealed that the deformation of MOF-5 progresses through cooperative rotation of the rigid BDC linkers and semi-rigid metal oxide cluster around the flexible carboxylate joints. ZnO_4 tetrahedral tilting and BDC linker rotation and lattice distortion as observed from MD simulation are presented in Fig. 5.5.

5.1.5   Effect of pressure

5.1.5.1 Effect on bond lengths and angles

The major bond angles (Zn-O-Zn, O- Zn-O, O-C-O, Zn-O-C) and distances (Zn-O, O-Zn) were analyzed to see if there is major changes in the lengths and angles. Cluster 1 and cluster 2 represents two metal oxide clusters at the two opposite corners of the (001) plane of the MOF-5 crystal. Atom numbers are provided to illustrate different similar angles (bonds) associated with the same atom.

The oxygen in (Zn-O-Zn) is the central O_2 in the metal oxide cluster where all four tetrahedra are connected, or, in other words, this is the inter-tetrahedral angle. The angle (O-Zn-O) is the intra-tatrahedral angle. We found negligible change in these angles with increase in pressure. From this table we observe that the inter-tetrahedral angle (between the four tetrahedral) at the Zn_4O cluster increases for some and decreases for the other, indicating tetrahedral tilting. This may also be observed from the simulation snapshot in Fig. 5.5. For a single tetrahedral, two of (O-Zn-O) increases from 109° to 115° and two of them decrease to 106° after deformation. Thus there are small changes in the tetrahedral shape. Thus we can conclude that the metal–oxide cluster behaves as if it is almost rigid. The (Zn-O-C) angle and the angle between O-C-O show small increase at 250 MPa and then decrease at 400 MPa. The change in (O-C-O) angle is also negligible.

The change in the major bond lengths: Zn-O, O-Zn, O-C remain negligible. O-C bond and C-C bond distance remain almost same (~1.38 Å and ~1.48 Å respectively). Thus it seems that although there are negligible changes in the bond length and the angles, major atomic displacement of the atomic clusters (and not single atoms) took place under external pressure, resulting in lattice distortion and deformation.

5.1.5.2 Effect on lattice energy

The total energy of the system increased upon compression, (Fig. 5.6). Crystal energy is a sum of potential and kinetic energy of atoms. Kinetic energy is imparted to the crystal as a part of the simulation, to study structural evolution. So at certain temperature it remains constant. Major changes are in its potential energy. Lattice potential energy is the summation of bonded (due to bond, angle, torsion and inversion) and nonbonded energy (coulomb, van der Waals). Bonded energy can give an indication of how the bonding environment changes inside the crystal. As observed from Fig. 5.6b the major contributing factor in the energy change is due to change in the torsion energy. In fact, a high amount of torsion was observed in the dihedral angle O-C-C-C. As mentioned before and indicated by other researchers, the O-C-O connection may be considered as a flexible hinge, across which the BDC linker can rotate freely.
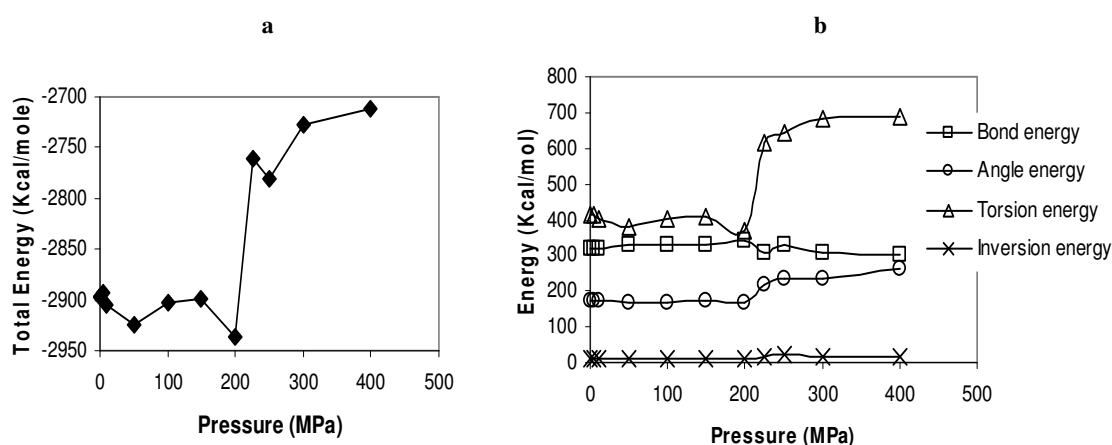

Fig. 5.6 (a) Total and (b) different bond energy profile of MOF-5 compression

5.1.5.3 Effect on torsion in BDC linker

Next we studied the torsion in the dihedral angle (O-C-C-C) connecting the BDC linker with the metal cluster (Fig. 5.7). There are 12 such modes in a single unit cell. The torsion along the

dihedral angle (O-C-C-C) is high. The dihedral angles changes by 180 degree for some cases indicating high torsion. Some researchers[40] also predicted by using first principle calculation and analysis of phonon dispersion curves that C_6H_4 linker twists around the crystal axis.
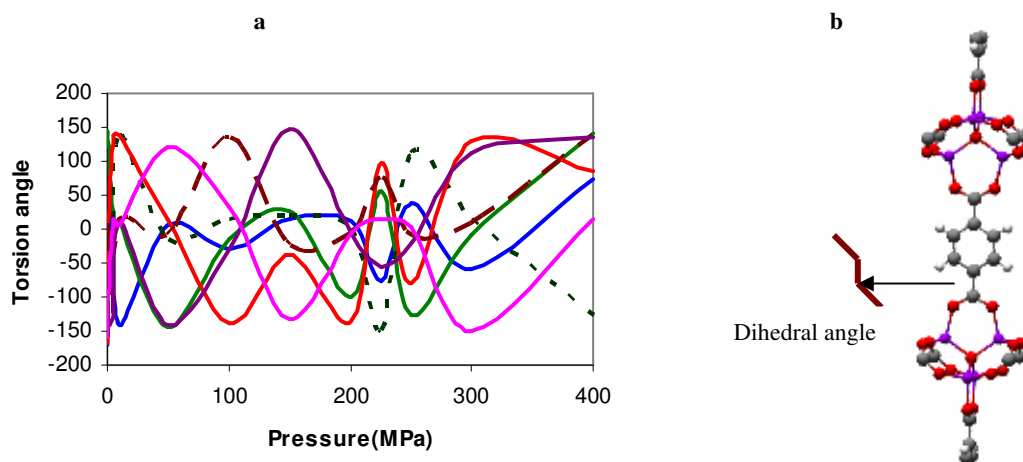

Fig. 5.7 (a) Change and (b) depiction for 6 selected dihedral O-C-C-C angles for torision

5.1.5.4 Effect on porosity

As the MOF crystal deforms under pressure, its porosity decreases. The channel dimension and the orientation in the deformed structure changes compared to the original structure (Fig. 5.8). The original structure has symmetric square channels in all three directions. But the deformed structure does not have uniform and through channels. They rather appear like isolated pockets. In the picture, light blue surface is the solvent accessible surface, grey surface surrounding the atoms are the inside surface which is not accessible. This shows that the deformed structure may not allow molecular passage through the crystal.
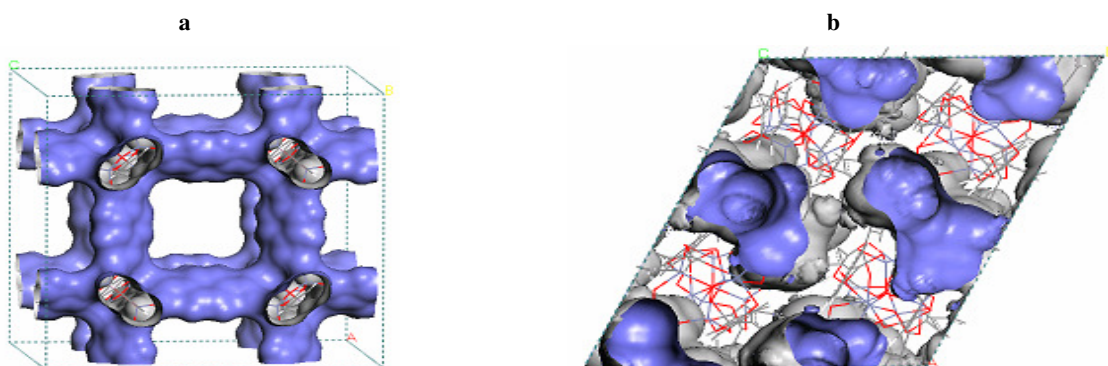
Fig. 5.8 Change in porosity after compression: a) original and b) deformed MOF-5

5.2 High pressure behavior of hydrogen filled MOF-5 crystal

5.2.1 *Pressure-volume behavior*

In order to understand the effect of presence of hydrogen on the deformation behavior we studied hydrogen filled MOFs crystal. We filled the original crystal with different amount of hydrogen i.e. 34, 68, 102 and 136 molecules per unit cell, which corresponds to 1.09, 2.16, 3.2 and 4.2 wt% hydrogen and these were subjected to high pressure. Pressure vs. volume relationship for hydrogen filled MOF-5 is similar to the empty MOF-5 (Fig. 5.9). However, in this case the threshold pressure required for collapsing the crystal is higher than the empty MOF-5 (Fig. 5.9). Also this threshold pressure depends on the amount of hydrogen present in the crystal. It seems that the presence of hydrogen renders resistance to the compression of the MOF-5 crystal. At low pressure the diffusion rate of hydrogen inside the MOF was high. This diffusion rate decreases with increase in the amount of hydrogen present inside the crystal. For example, when MOF-5 was filled with 102 molecules of hydrogen the self diffusion coefficient of hydrogen at atmospheric pressure (298 K) is $\sim 1.08 \times 10^{-3}$ cm^2/sec (1.08×10^{-7} m^2/sec). These values are comparable with other findings. For example, a diffusivity value of $\sim 1.5 \times 10^{-8}$ m^2/sec

at 77 K and 10 MPa was found by others.[150] The difference in value is probably due to the temperature difference.
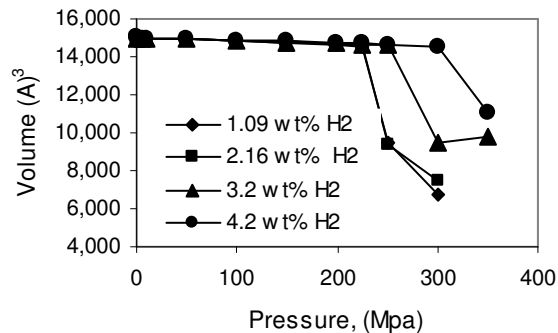

Fig. 5.9 Pressurization behavior of hydrogen filled MOF-5

5.2.2   Reversibility under depressurization

We carried out the depressurization study of these hydrogen filled MOF. Fig. 5.10 shows the pressure-volume behavior of hydrogen filled MOF-5 under depressurization. This showed that the volume reversibility depends on the amount of hydrogen present in the crystal. For low hydrogen (34 molecules) filled MOF-5, deformation is reversible only when the pressure difference between low and high pressure is large. However for crystals with higher amounts of hydrogen, the deformation is reversible when the pressure differential is smaller.
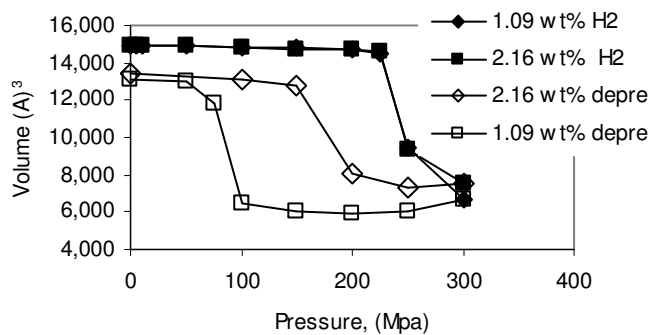

Fig. 5.10 Depressurization behavior of hydrogen filled MOF-5

The pressurization and depressurization behavior is reversible even when multiple cycles were carried out. The results for multiple cycles for 102 molecules of hydrogen filled MOF-5 is presented in Fig. 5.11. Though we considered short simulated cycle time of 100 pico sec. to curtail the simulation run time, but the observations made here will be similar when the cycle time is of higher order. This is because the 100 pico sec. time is sufficiently large compared to time events in the atomic scale.
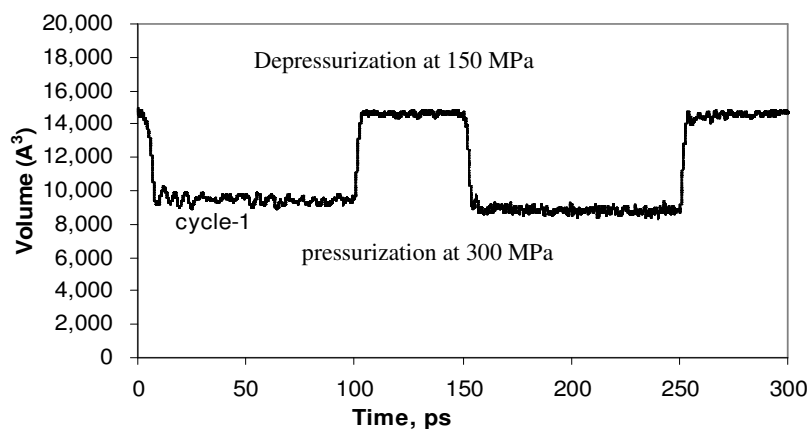
Fig. 5.11 Cyclic pressurization behavior of H$_2$ filled MOF-5 at 300 MPa and 150 MPa

As observed, MOF-5 gets deformed to ~40 % of its volume at 300 MPa and this deformation is reversible from any stage of the trajectory. This is in contrast with the behavior of empty MOF-5, where reversibility could not be achieved. The reason may be that with hydrogen filled MOF-5, 1) some amount of hydrogen still remained inside the crystal after compression. The presence of this hydrogen probably assists in decompression process, 2) the volume compression is less (~40 %) compared to empty MOF (~50%). Since the volume of hydrogen filled MOF-5 after compression is bigger than the empty MOF-5 (~9000 Å^3 and ~6000Å^3/unit cell, respectively),

the atoms are farther apart, and hence possibility of forming any strong interaction (π-π interaction) may be less.

5.3   High pressure behavior of other MOF crystals

5.3.1   Elastic properties

Similar pressure -volume studies was performed with other MOFs: IRMOF-3, 6, 8, 10 and 14 having aniline di-carboxylate, cyclobutylbenzene-di-crboxylate, naphthalene-dicarboxylate, biphenyl-di-carboxylate and pyrene-di-carboxylate linkers respectively (Fig. 5.12).

IRMOF-3   **IRMOF-6**   **IRMOF-8**   **IRMOF-14**
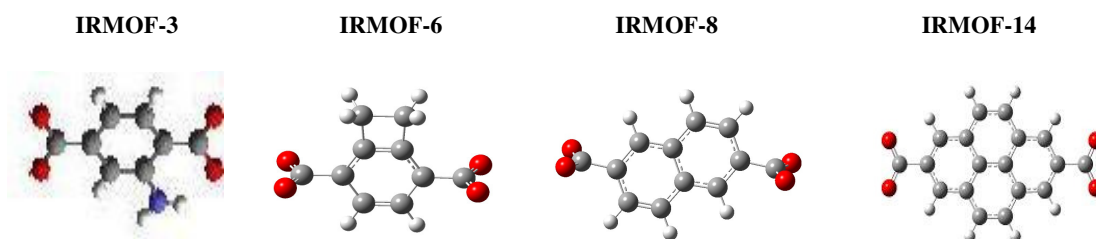
Fig. 5.12 Linkers of IRMOF-3, IRMOF-6, IRMOF-8, IRMOF-14

Mechanical property of these MOFs are tabulated below (Table 5.1).

Table 5.1   Comparison of mechanical property of the selected MOFs

MOF	C_{11}	C_{44}	Bulk Modulus(GPa)	Young's Modulus(GPa)
IRMOF-1	43.32	1.597	18.5834	41.76
IRMOF-3	42.2204	0.51826	13.246	40.428
IRMOF-6	27.57891	0.36599	7.5805	27.1129
IRMOF-8	32.87211	0.24688	7.1358	15.7069
IRMOF-10	91.8342	11.5123	36.2109	90.4266
IRMOF-14	31.65842	0.51909	13.182	30.7847

All these MOFs, except IRMOF-10, have lower C_{44} constant compared to IRMOF-1, indicating that these are more unstable than IRMOF-1 and thus these require lower pressure to deform. Similar values of bulk modulus and low C_{44} constants have been observed by others.[38-41] IRMOF-10 is a stiff material and thus could not be compressed more than 20 % of its volume.

5.3.2   *Pressurization and depressurization behavior*

Deformation process of these MOFs progresses similarly as the MOF-5, by bond rearrangement and large atomic displacement. The results for empty MOFs are presented in Fig. 5.13.
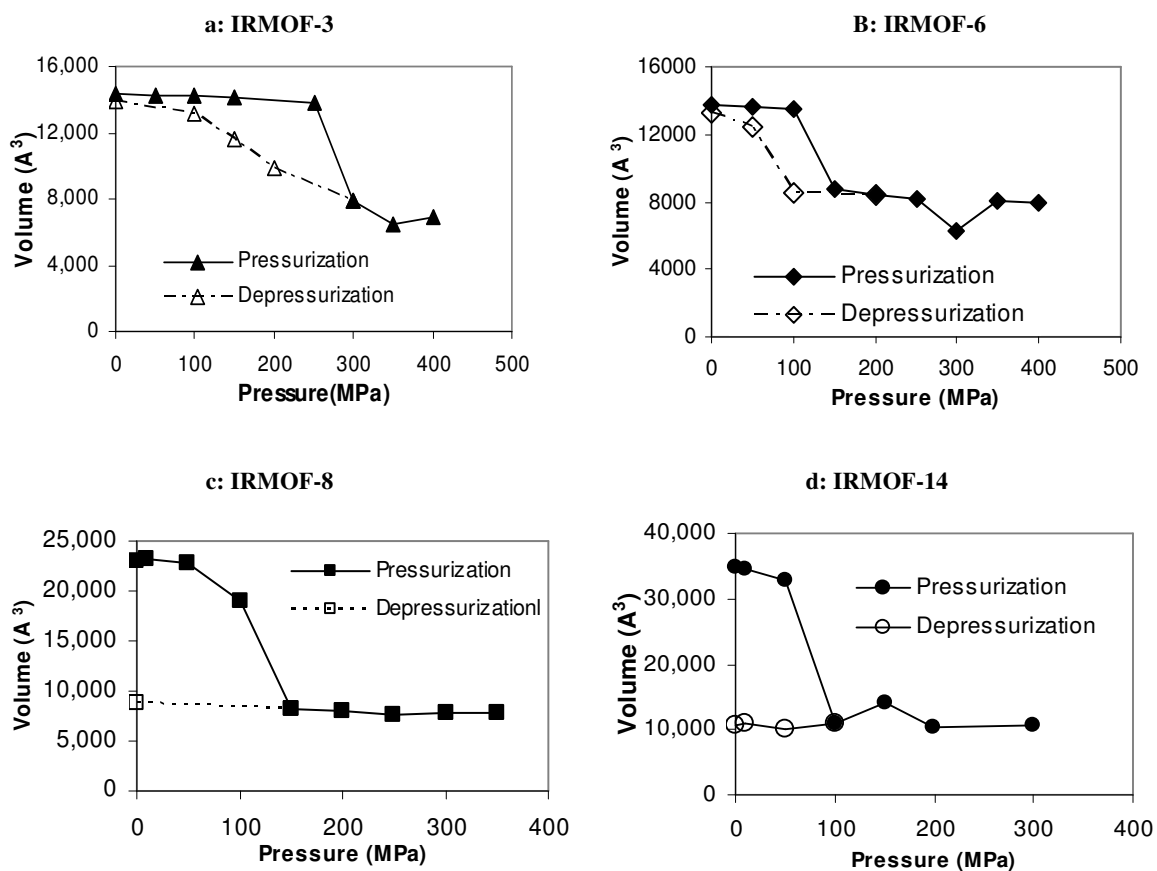

Fig. 5.13 Pressurization, depressurization behavior of different empty MOFs

IRMOF-3 and IRMOF-6 (Fig. 5.13a & b) with linkers of substituted benzene undergo completely reversible pressure induced transformation irrespective of whether the crystal is empty or filled with hydrogen. This is probably due to the fact that the volume compression in these two crystals are less (44.7% and 36%) compared to MOF-5 (55.9%) making the organic linkers in the compressed structure far apart from each other compared to IRMOF-1 and hence π-π interaction is weaker. MOFs with fused benzene rings seem to be more compliant. Deformation of IRMOF-8 and IRMOF-14 was irreversible (Fig. 5.13c & d). IRMOF-8 & 14 has low threshold pressure for compression. IRMOF-14 (pyrine dicarboxylate linker) deforms at a lower pressure (100 MPa) compared to MOF-5. IRMOF-14 undergoes a volume compression of 68%, which is higher than MOF-5 and in the deformed structure; the pyrene linkers face each other, thus indicating stronger π-π interaction.

Deformation process of IRMOF-8 crystal when filled with 2.7 wt% H_2 was reversible (Fig. 5.14a). But the deformation of hydrogen filled (2.8 wt%) IRMOF-14 was irreversible (Fig. 5.14b) for the hydrogen concentration studied here. IRMOF-10 with longer biphenyl dicarboxylate linker is a stiff material (C_{44} constant 11.5123) and seems not to be amenable to any large deformation. It undergoes lower volume compression (~20%) compared to other MOFs.
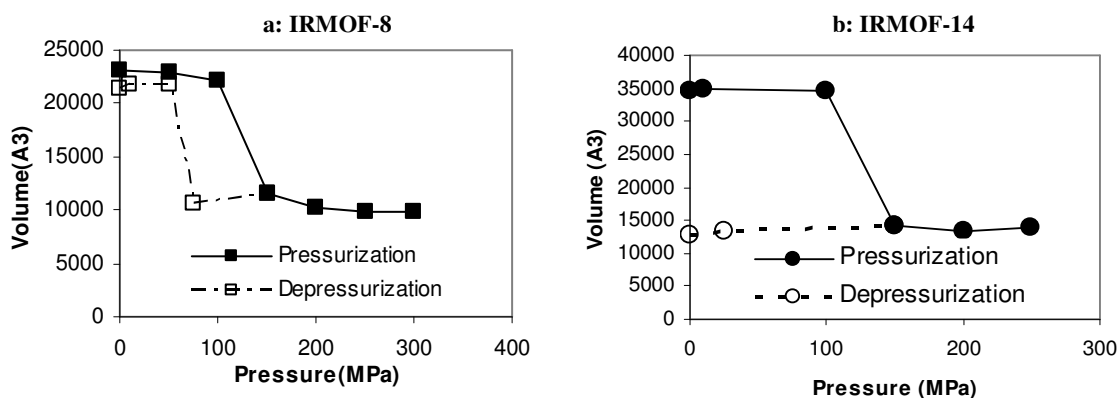
Fig. 5.14 Pressurization, depressurization behavior of other hydrogen filled MOFs

5.4 Summary

Using molecular dynamics simulations, we have shown that IRMOF-1, IRMOF-3, IRMOF-6, IRMOF-8 IRMOF-10 and IRMOF-14, undergo structural deformation and subsequent large scale volume compression at high pressures. This deformation is due to reorganization of the linkers and ZnO_4 tetrahedra. There is large torsion energy along the dihedral angle O-C-C-C. MOFs with fused rings seem to be softer than single benzene ring which is evident from the low C_{44} constant and low deformation pressure. These high pressure induced deformation is reversible for some empty MOF with functionalized linker but for other MOFs reversibility depends on the presence of hydrogen. In a real crystal, the actual pressure required to observe these transformations is expected to be lower due to presence of defects, making the process more feasible.

Crystal to amorphous transition has been observed in case of ZIF-8, a similar porous structure with a bulk modulus 6.52 GPa. At around 0.3 GPa ZIF-8 loses crystallinity which was evident from broader and vanishing peaks in the x-ray crystallography study. IRMOF-6 and IRMOF-8 has similar low bulk modulus and C_{44} constant. Thus this type of amorphization may be possible

for the softer MOFs with low bulk modulus and C_{44} constant. However, universal forcefield is not equipped to capture this crystal to amorphous transition. Further study with appropriate forcefield is required to predict the transition from crystal to amorphous phase.

CHAPTER VI

BEHAVIOR OF IONIC LIQUID

In this chapter, we present our observations on structure, thermodynamic and transport properties of imidazolium based ionic liquid [BMIM][BF4] (1-butyl-3-methyl imidazolium- tetrafluoro borate) computed from our simulation studies. The molecular structure of this ionic liquid is presented in Fig. 6.1. In these studies, we used quantum mechanics (QM) calculation and molecular dynamics (MD) simulations. In the QM calculation, we have used density functional theory (DFT). Then using the results obtained from QM calculations, we had parameterized the forcefield (CVFF) and conducted MD simulation using LAMMPS software.

Fig. 6.1 Structure of [BMIM][BF4] ionic liquid
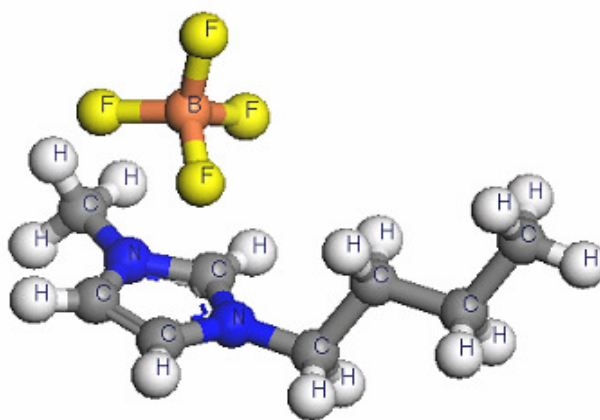
To establish the validity of our QM calculations, we have compared the charge distribution, bond length and angles as observed from our models with the experimentally measured values. We also present the results from the molecular dynamic simulation that characterize the bulk behavior, i.e. pressure volume relationship, structural and transport properties and dielectric

constant of this ionic liquid. Next, we discuss the results that describe its behavior on graphite surface, a situation which will be encountered in Li-ion batteries. Finally we show the results that portray the behavior of this ionic liquid and LiBF$_4$ salt mixture.

6.1   Observations from quantum mechanical calculations

6.1.1   Observed charge distributions

Fig. 6.2 gives the surface charge distribution of cation and anion complex as observed from quantum calculation. Charges were also calculated using ChelpG and Merz-Kollman (MK) methods.[204] Table 6.1 compare these charges obtained by various methods. For atom names used in the table refer Fig. 6.3.
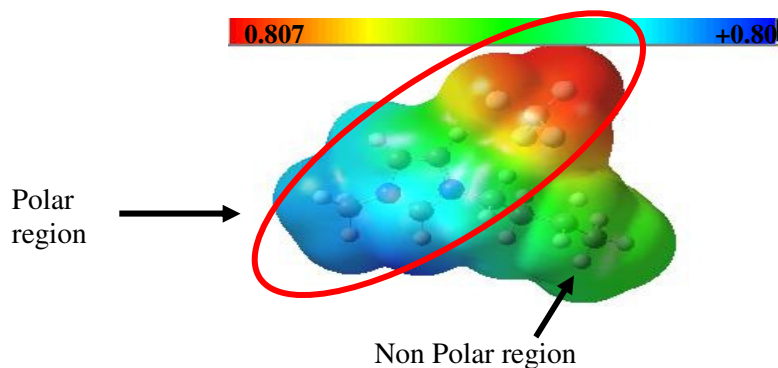

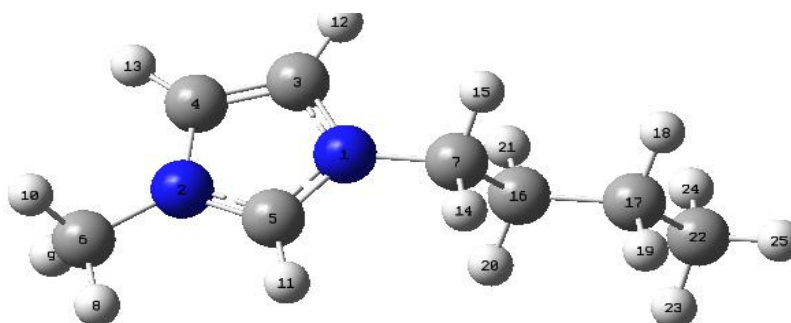**Fig. 6.2 Charge distribution on BMIM^{+1} and BF4^{-1}**

Fig. 6.3 Atom numbers on BMIM^{+1} as given in Gaussian software

Table 6.1 Atom numbers and charges by different method on BMIM^{+1} and BF4^{-1}

BMIM^{+1}		Charge		
Atom No.	Element	Mulliken	ChelpG	MK
1	N	0.114	0.189	0.349
2	N	-0.019	0.142	0.269
3	C	-0.094	-0.177	-0.288
4	C	-0.104	-0.110	-0.176
5	C	-0.082	-0.106	-0.218
6	C	-0.238	-0.194	-0.385
7	C	-0.481	-0.188	-0.432
8	H	0.171	0.130	0.180
9	H	0.218	0.135	0.181
10	H	0.223	0.134	0.181
11	H	0.21	0.225	0.249
12	H	0.205	0.225	0.275
13	H	0.217	0.198	0.234
14	H	0.185	0.101	0.167
15	H	0.228	0.104	0.171
16	C	0.044	0.145	0.116
17	C	-0.24	0.140	0.153
18	H	0.143	-0.010	0.005
19	H	0.144	-0.012	0.002
20	H	0.155	-0.020	0.017
21	H	0.144	-0.018	0.010
22	C	0.6	-0.233	-0.368
23	H	0.145	0.605	0.093
24	H	0.146	0.061	0.096
25	H	0.167	0.083	0.120

BF4^{-1}		Charge		
Atom No.	Element	Mulliken	ChelpG	MK
1	B	1.065	1.202	1.191
2	F	-0.516	-0.551	-0.548
3	F	-0.516	-0.551	-0.548
4	F	-0.516	-0.551	-0.548
5	F	-0.516	-0.551	-0.548

As observed in case of BMIM^{+1}, unlike Mulliken charges, ChelpG and MK methods both had shown positive charge on the imidazolium nitrogen atom. The charge in case on MK method is higher than that of ChelpG method. Other researchers have reported similar charges based on

ChelpG method.[204] We decided to work with the charges based on ChelpG method because it is widely used. The charges on BF4[-1] are similar in all the three cases and comparable with other results.[204]

6.1.2   Bond length and angles

We have compared the experimental and calculated values of bond lengths, angles and dihedrals on BMIM[+1] in Table 6.2 (atoms are identified in Fig. 6.4). The atom nomenclatures were kept the same with the available literature[216] for easy comparison.
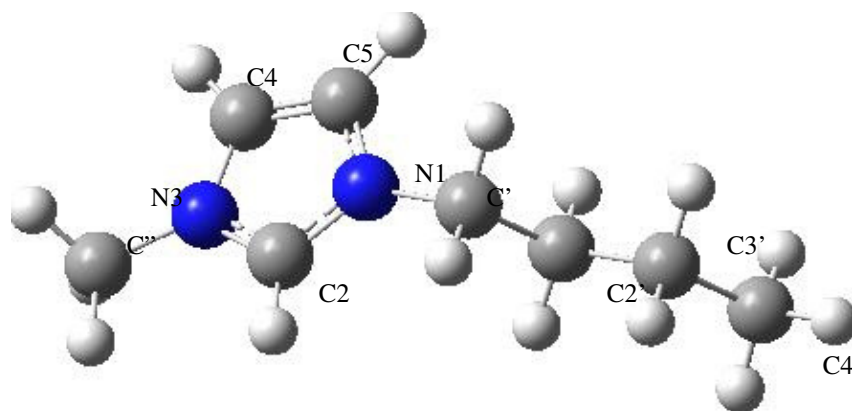
Fig. 6.4 Atom nomenclature on BMIM[+1]

As observed from Table 6.2, the calculated bond lengths, angles and dihedrals observed from both QM and MM (molecular mechanics) method match quite well with the experimental values obtained by X-Ray diffraction.[216] There is slight deviation in dihedrals but these values matches with other theoretical results reported in the literature.[216] For example, the angle for BF4[-1] is 109.5 degree and the B-F bond length is 1.417 Å in QM compared to 109.5 degree and 1.481 Å in MM.

Table 6.2 Major bond length angles and dihedrals on BMIM[+1]

Major Bond Distances(Å)				Selected angles(degree)			
	X-ray	QM	MM		X-ray	QM	MM
C1"-N3	1.465	1.471	1.435	C1"-N3-C2	124.9	125.9	127.3
C4'-C3'	1.518	1.531	1.552	C1"-N3-C4	125.9	125.7	125.6
C2'-C3'	1.475	1.535	1.554	C4'-C3'-C2'	116.1	112.5	111.1
C1'-C2'	1.526	1.53	1.552	C2'-C1'-N1	110.9	112.6	110.6
C1'-N1	1.478	1.483	1.438	C1'-N1-C2	125	125.8	126.6
N1-C2	1.332	1.336	1.352	C1'-N1-C5	125.9	125.9	126.5
C2-N3	1.334	1.338	1.351	N1-C2-N3	107.9	109	110.2
N3-C4	1.369	1.382	1.346	C2-N3-C4	109.2	108.4	107.1
C4-C5	1.355	1.361	1.388	N3-C4-C5	106.9	107.1	107.8
C5-N1	1.373	1.381	1.348	C4-C5-N1	107	107.3	108
Main Dihedral angles (degree)				C5-N1-C2	109	108.3	106.9
C2'-C1'-N1-C5	112.4	99.8	69.9	**Ring Total**	540	540.1	540
C2'-C1'-N1-C3	66.5	-77.36	110				

6.1.3   Dipole moment and IR spectrum

The anion BF4[-1] has no dipole moment as observed in case of other anions.[231] However BMIM[+1]

has a large dipole moment of 5.6615 Debye. We also calculated the IR spectra of these two
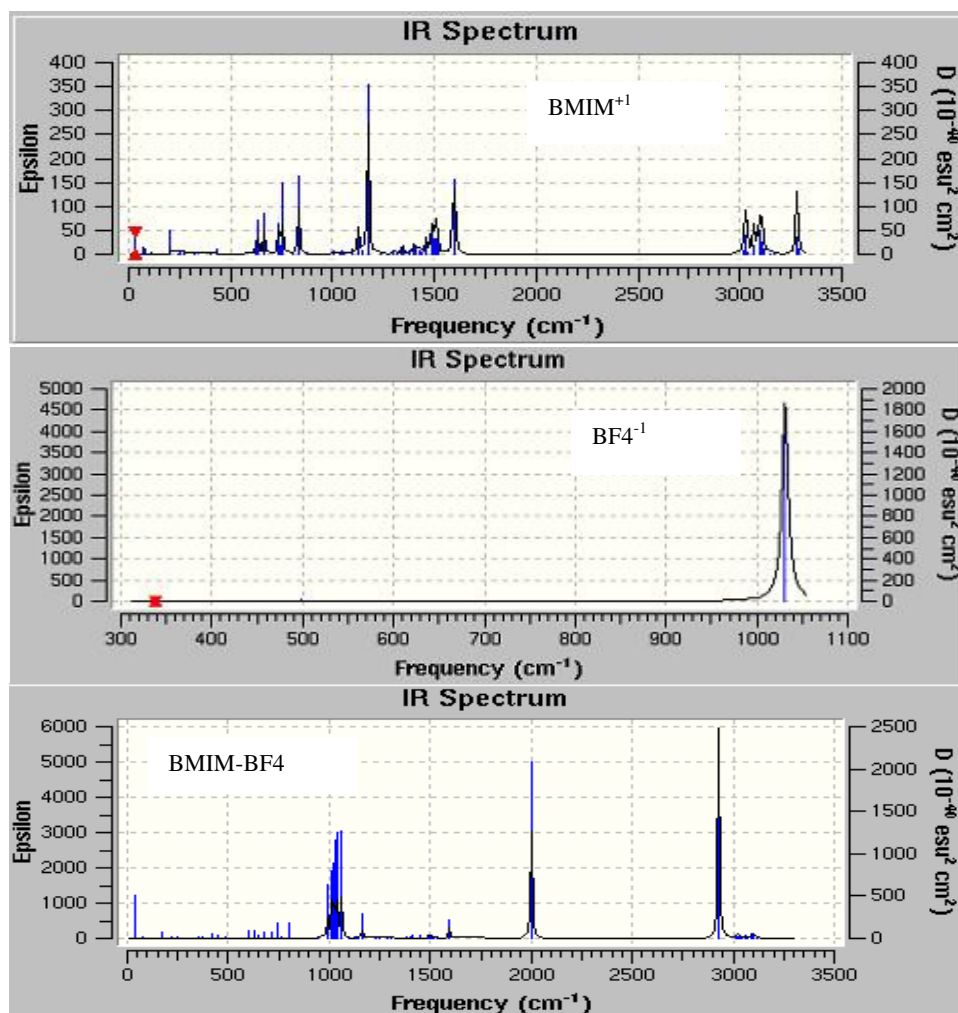
molecules and presented them in Fig. 6.5.

Fig. 6.5 IR spectra of BMIM^{+1} and BF4^{-1} and the combined ions

6.1.4 Orientation of anion and cation

We have conducted a DFT calculation of the anion and cation complex to observe the preferred orientation of the ions. This is presented in Fig. 6.6. There is a possibility of forming hydrogen bonds with the F atoms of anion and the H atoms of cation as observed by the distance between these two atom types. Along with other types of interactions like Coulombic and van der Waals, presence Hydrogen bonding will contribute in ion interaction and formation of networked structure in the ionic liquid.
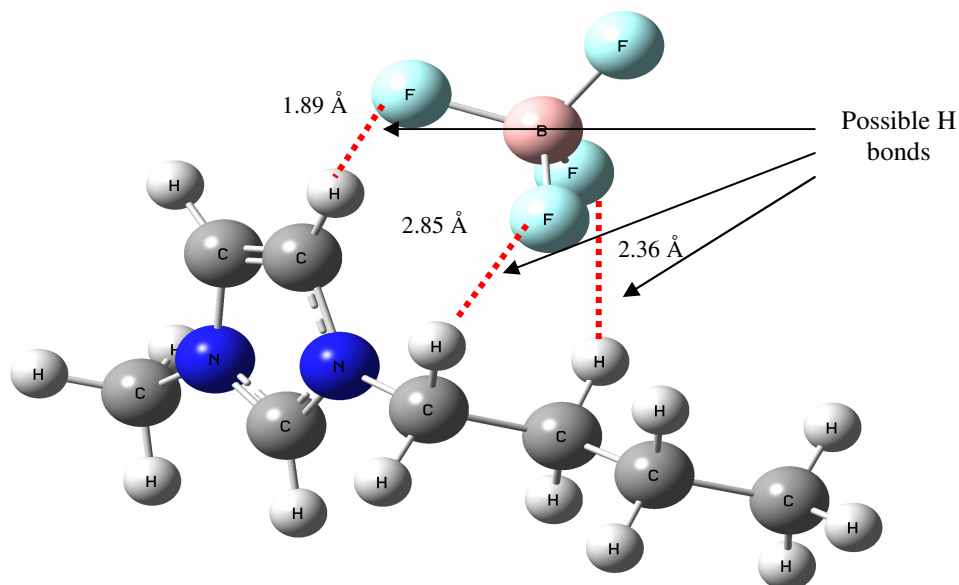
Fig. 6.6 Orientation, charges and possible H bonds in [BMIM][BF4]

6.2 Observations from molecular dynamic simulations

6.2.1 Thermodynamic properties

6.2.1.1 Density and volume

Fig. 6.7a & b gives the density and volume relationship with temperature. The thermal expansion coefficient α was calculated using the equation 2.17, as presented in Chapter II. The thermal expansion coefficient calculated from the slope of the volume-temperature trajectory in Fig. 6.7a is 5.92×10^{-4} K^{-1} at 298 K. The reported experimentally observed value is 6.05×10^{-4} K^{-1} at this temperature.[169,226] Thermal expansion coefficients do not change much with temperature. The values are similar to the α of water but it is lower than other organic liquids and higher than high temperature molten salts.[227]
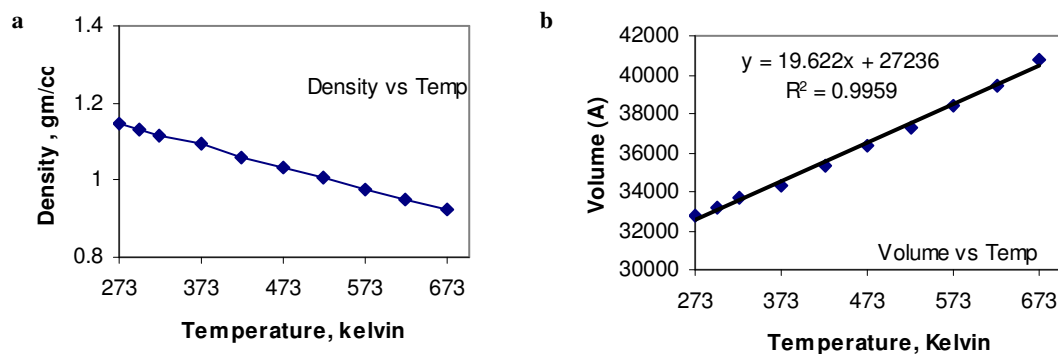
Fig. 6.7 a) Density vs temperature relation, b) volume vs. temperature relation

The average value of total energy of the system at different temperature was calculated and is presented in Fig. 6.8.
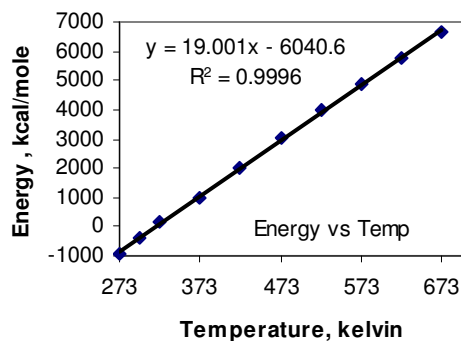

Fig. 6.8 Total energy vs temperature profile

From the slope of energy vs temperature graph, the specific heat capacity was calculated as 397.12 J/mole/ K, using equation 2.18. The experimentally observed value of heat capacity is 351.5J/mole/K.[169]

Using MD simulation, the average volume was calculated at different pressures: 1, 50, 100 200, 300 400 500, 600, 800 and 1000 atm. The pressure-volume relationship profile is given in Fig. 6.9.
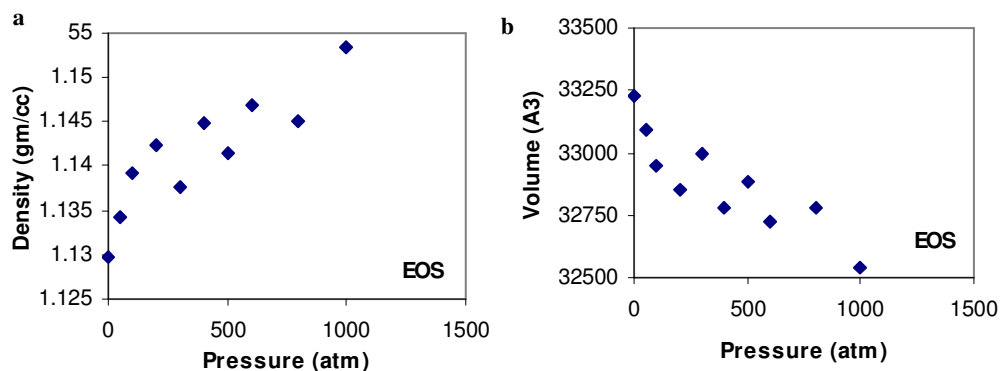
Fig. 6.9 a) Density vs pressure relation, b) volume vs. pressure relation

Using equation 2.21 and these data, the compressibility for the [BMIM][BF4] system was calculated as 318.42 $x10^{-12}$ Pa^{-1}. This is comparable with the experimentally observed value of 336.23 $x10^{-12}$ Pa^{-1}.[226]

6.2.2 Structural properties

6.2.2.1 Radial distribution function

Radial distribution function (RDF) g(r) gives an indication about the packing of the ions. Radial distribution function of the cation and anion was calculated and these are presented in Fig. 6.10. The profile matches with the reported value in the literature.[166]

Fig. 6.10   Radial distribution function of ions

The cation-cation (BMIM-BMIM) coordination number can be obtained from $g_{cc}(r)$, anion–anion (BF4-BF4) coordination from $g_{aa}(r)$ and th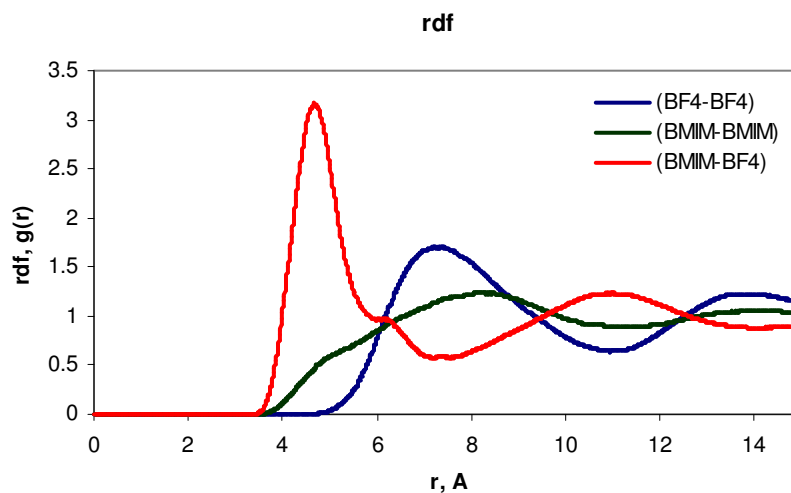e cation-anion coordination from $g_{ac}(r)$. Integration of the curve for $g_{cc}(r)$, $g_{aa}(r)$ and $g_{ac}(r)$ upto r value where the first minimum occurs gives the coordination number. For $g_{cc}(r)$ and $g_{aa}(r)$ integration was done till 11 Å, and for $g_{ac}(r)$ integration was done till 7.5 Å. The coordination number for A-C was 5.25 and C-C and A-A was 6.58 and 6.93 respectively.

The coordination number for C-C and A-A match with values observed by others.[166,171] But the A-C coordination number of 5.25 is lower compared to that of [BMIM][PF6] which was reported as 6.8.[166] Radial distribution functions at different temperatures were calculated and this is presented in Fig. 6.11. The coordination numbers do not change much with temperature. For example $g_{ac}(r)$ changes from 5.25 for temperature 300K to 5.70 at 473 K.
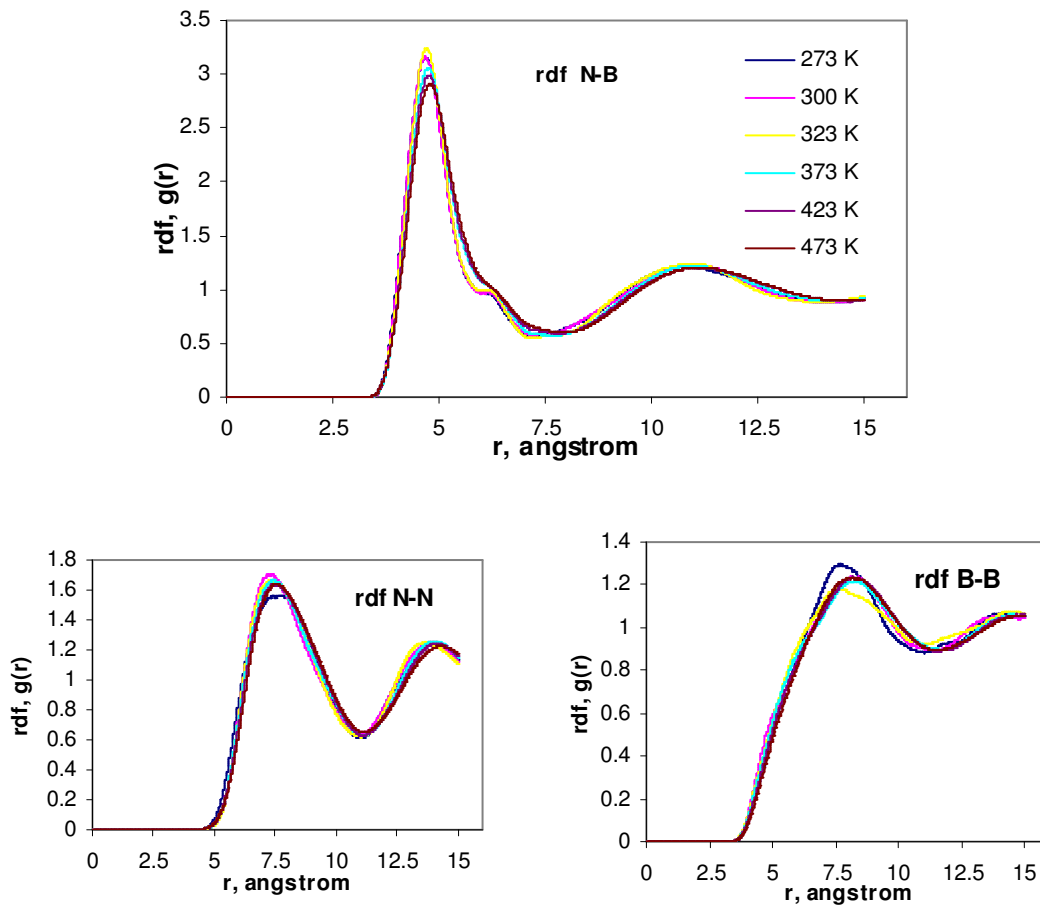
Fig. 6.11 Radial distribution function variation with temperature

6.2.2.2 Charge distribution function

The charge distribution functions $Q_c(r)$ and $Q_a(r)$ gives indication on how the charges are distributed around a central ion and this can be calculated from radial distribution function using equation 2.23 to 2.25. This is shown in Fig. 6.12. From this it is evident that the cation and anion distribution functions are out of phase. This means that they are arranged in layers of alternate shells. The positive ions surrounded by negative ions and again by a layer of positive ions and so on. This arrangement is called as solvation shells. In this arrangement charge neutrality happens in local scale. The effect of the central ion in coulombic interaction decays

much faster giving rise to 'charge screening effect'. The distance upto which the interaction remains and beyond which charge screening occurs is given by the Debye screening length. Debye Huckel screening length λ_D may be obtained from total charge distribution function using equation 2.26. The value of λ_D was also obtained from the slope of the tangent through the maximum points of the periodic function of $\ln|rQ(r)|$ vs r plot (also presented in Fig. 6.12).
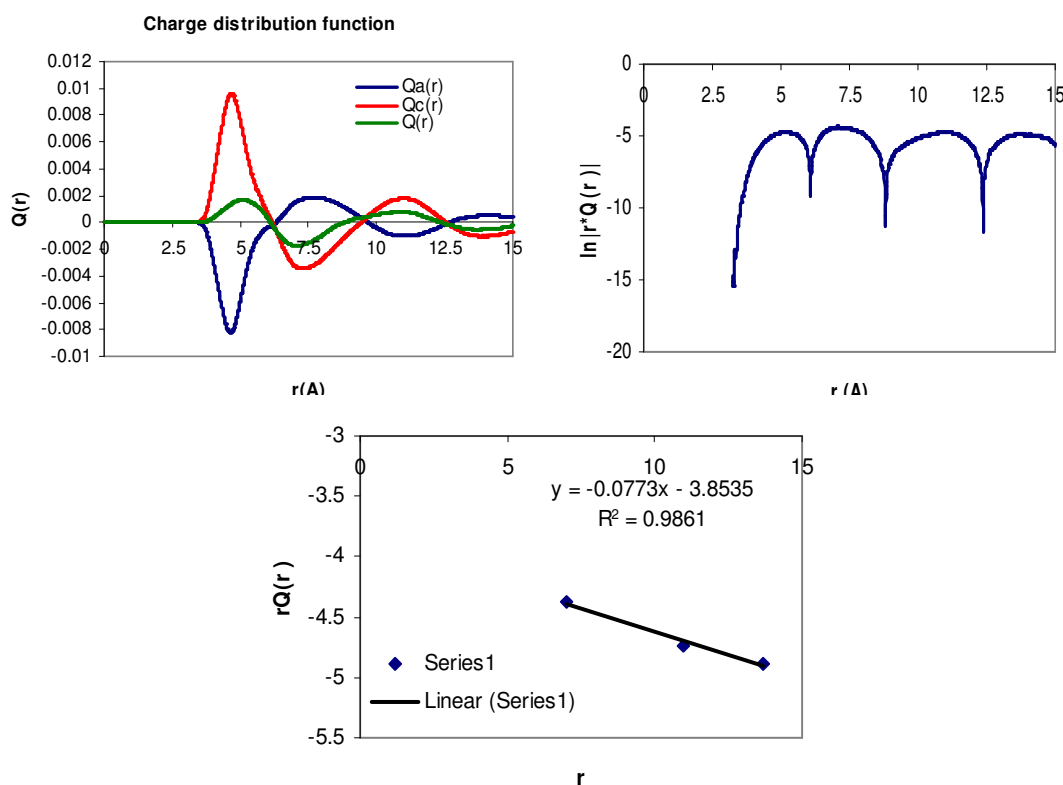
Fig. 6.12 Charge distribution function and derivation of Debye Huckel screening length

That means that λ_D = (1/slope) of the $\ln|rQ(r)|$ vs r plot. The value of λ_D thus obtained was 12.9 Å. This is similar to other reported values.[166] This indicates that the charged structure that is formed in ionic liquid is long ranged and has decay constant λ_D having the size of two to three solvation shells. This also indicates substantial coupling action between ions. Thus balance of

electrostatic interaction and strong coupling between large collections of ions is a characteristic feature in ionic liquids.[166]

6.2.3   Transport properties

6.2.3.1 Ion diffusion

Ion diffusion was obtained from mean square displacement (MSD) of the center of mass of the individual ions. The profile at 300 K is presented in Fig. 6.13.
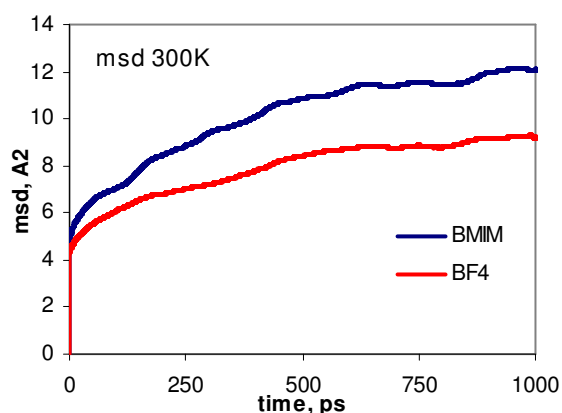
Fig. 6.13   Mean square displacement of cation and anion

As observed from this figure that the cation has higher diffusion than the anion. Mean square Displacement (MSD) at different temperature was plotted and the result is presented in Fig. 6.14. The MSD profile at 273 and 300 K shows that it has reached a plateau, but the MSD at 373 K to 473 K temperature range increases with time. The log log plot of MSD vs time provides us information about the mechanism of diffusion D, as mentioned in section 2.12.3. All the plots show initial ballistic region where D is proportional to t^2. At longer time range a diffusive zone appears where D is proportional to t. In between these two zones the profile shows a plateau region or subdiffusive region, where D is proportional to t^α with $\alpha < 1$. This indicates that the

ions are trapped in some cage network and are not free to move much. These regions are more pronounced in the MSD trend at high temperature. At low temperatures, between 273 K and 300K, probably due to low kinetic energy of the ions and also low available volume, the MSD profiles show subdiffusive zones till 1 ns, meaning they spend much longer time in caged network structure. These MSD behaviors with time agree with observations made by others.[166]
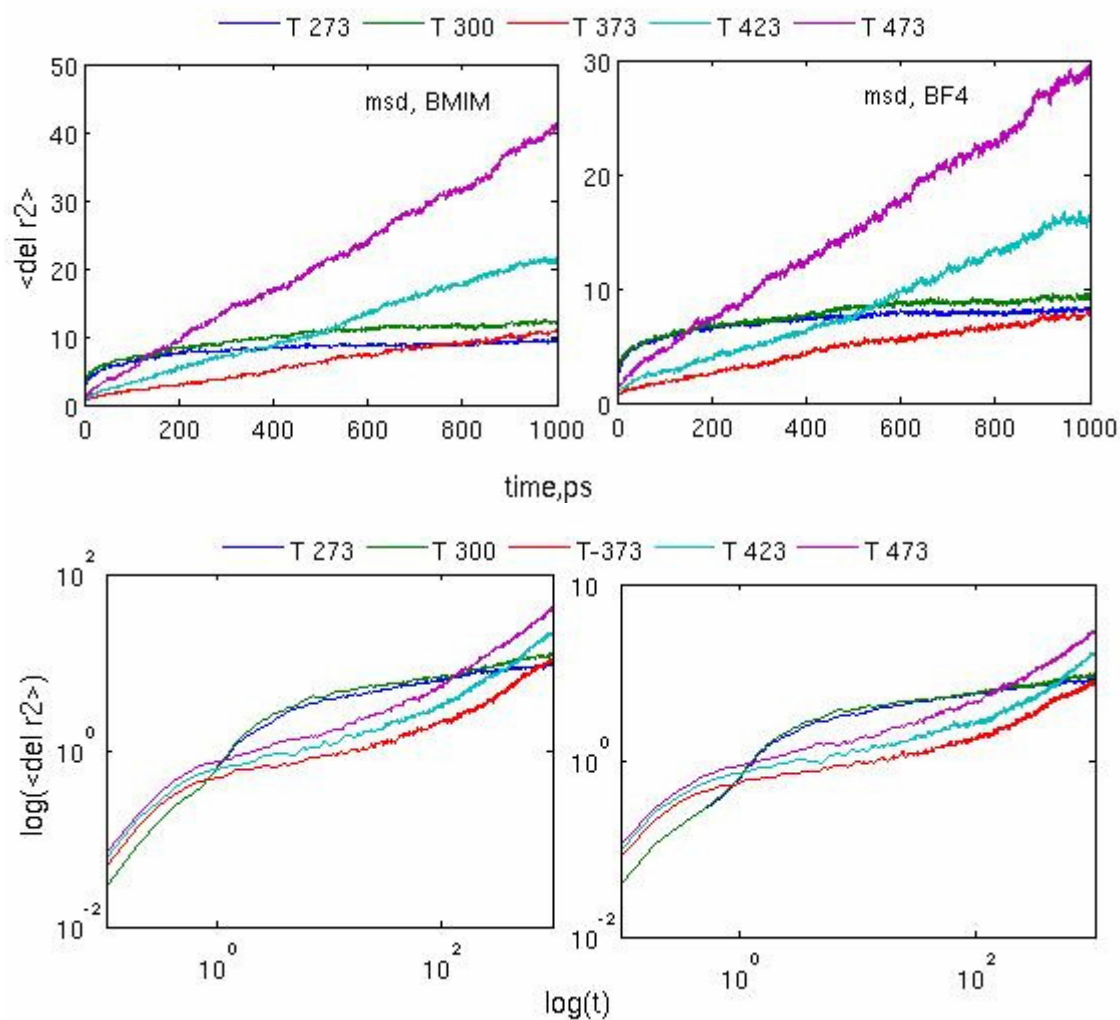

Fig. 6.14 Mean square displacement profile with temperature

Diffusion coefficient for BMIM was found to be around 9.5×10^{-12} m^2/s and for BF4 it is around 7×10^{-12} m^2/s. These values were obtained from the slope of the MSD vs time plot (Fig. 6.15), using Einstein relation as in equation 2.30. These values are similar to the ones reported in the literature.[203] Experimentally observed value is 15×10^{-12} m^2/s for BMIM and 13×10^{-12} m^2/s for BF4.[203] Reported values from theoretical calculation for BMIM and BF4 are 8.2×10^{-12} m^2/s and 3.0×10^{-12} m^2/s respectively,[203] 12×10^{-12} m^2/s, 10×10^{-12} m^2/s respectively.[216] We also find that the bigger cations (BMIM) have higher diffusion compared to anions (BF4). That is because the small anions tend to be trapped by the cage structure formed by the butyl chain of the cations and cannot move freely. This agrees with observations made by others.[203, 216]
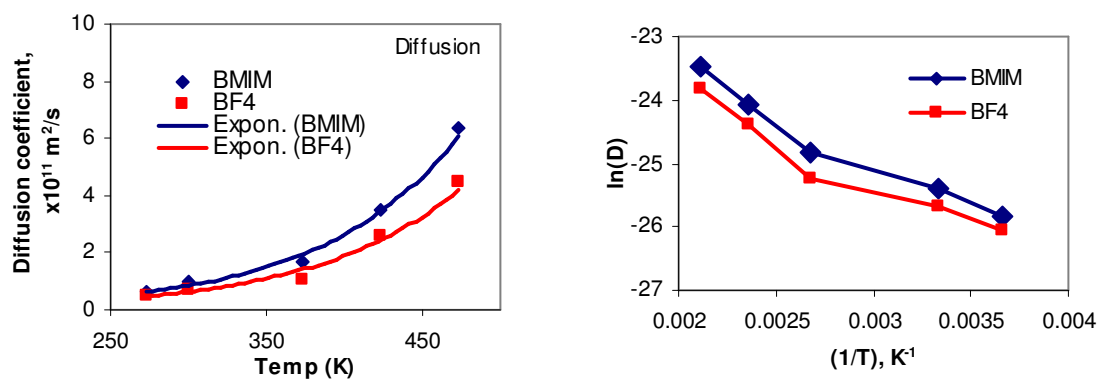
Fig. 6.15 Temperature dependence of diffusion coefficient

Ionic liquid has been observed to behave like supercooled liquid according to Vogel-Fulcher-Tamman (VFT) equation (equation 2.31) that describes its diffusion behavior with temperature rather than Arrhenius equation. The diffusion vs temperature profile was fitted to the Vogel-Fulcher-Tamman equation (Fig. 6.16) and the fitting parameters are given below in Table 6.3.
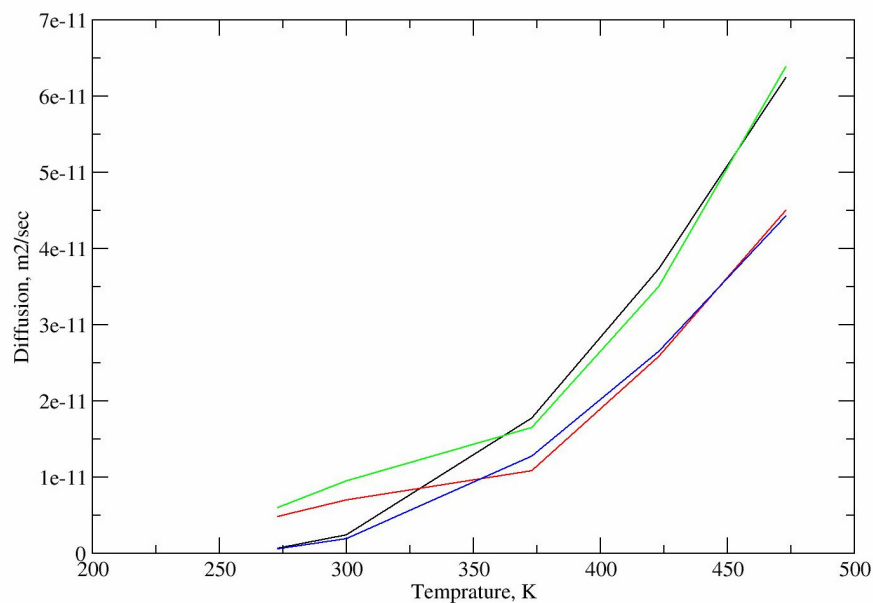
Fig. 6.16 Diffusion vs temperature profile fitted to Vogel-Fulcher-Tamman equation

The plot, in Fig. 6.16, shows the typical exponential behavior of a supercooled liquid. Cations have higher activation energy than anions. Since cations have larger size, they need more energy to move around. The main difference is observed in D_0 value which is less than reported in literature.[228] Other values (B and T_0) match with the reported values.[228]

Table 6.3 VFT parameter

		$D_0 \, (m^2/s)$	B (K)	T_0 (K)
Calculated value	BMIM	1.03113×10^{-9}	905.32	150.227
	BF4	8.005×10^{-10}	963.501	140.235
Experimental Value[228]	BMIM	1.4×10^{-8}	935	162
	BF4	2.8×10^{-8}	1108	153

6.2.3.2 Conductivity

Ionic conductivity was measured using Nernst-Einstein relation, according to equation 2.34, where F is the Faraday constant, z is the charge. The result is shown in Fig. 6.17.
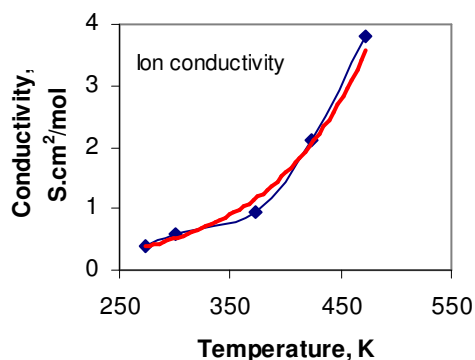
Fig. 6.17 Temperature dependence of molar ion conductivity

The calculated value was 5.74×10^{-5} S m^2/mol (0.574 S cm^2/mol) compared to conductivity value of 9.45×10^{-5} S m^2/mol for [BMIM] [PF6] system calculated by another theoretical calculation.[229] Experimental value for [BMIM] [BF4] is 0.65 S cm^2/mol.[175]

6.2.3.3 Velocity autocorrelation function

The velocity autocorrelation for the ions for different times is shown in Fig. 6.18 and the power spectra is given in Fig. 6.19. In all temperatures the velocity gets decorrelated from the initial values within 1 ps. The Fourier transform of the velocity autocorrelation gives the IR spectra. It may be observed that the Fourier transform does not reveal any strong peak and the trend is similar in all temperatures.
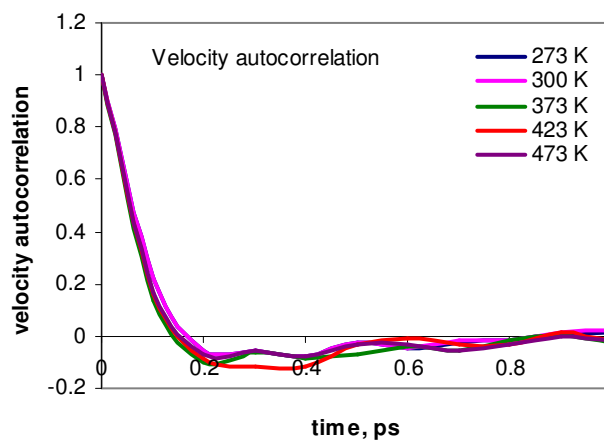
Fig. 6.18 Ionic velocity autocorrelation function
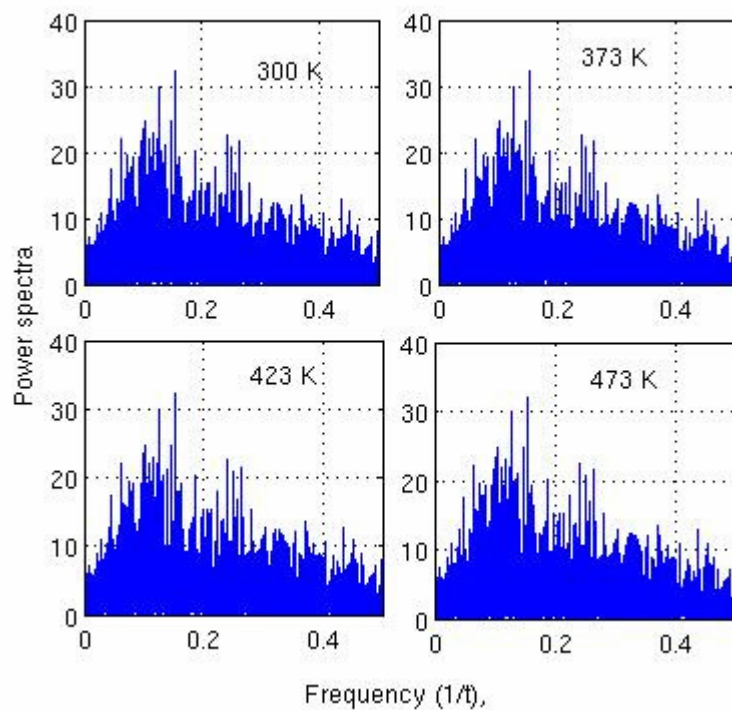
Fig. 6.19 Power spectrum of velocity autocorrelation function

6.2.4   Calculations of parameters using dipole moment

6.2.4.1 Dipole moment autocorrelation and relaxation time

As observed in the QM calculation, [BMIM][BF4] has some dipole which is mainly due to the cation. For the IL system, dipole moment was calculated from the charges (q_i) and the position (r_i) according to equation 2.39 & 2.40 and presented in Fig. 6.20. Fig. 6.20a presents the autocorrelation trajectory for the entire duration till 1000 psec., whereas Fig. 6.20b the same for the first 2 ps duration. It is also evident that the time trajectory of the dipole autocorrelation at lower temperature (273 and 300 K) is flat compared to that at higher temperature (373 -473 K).
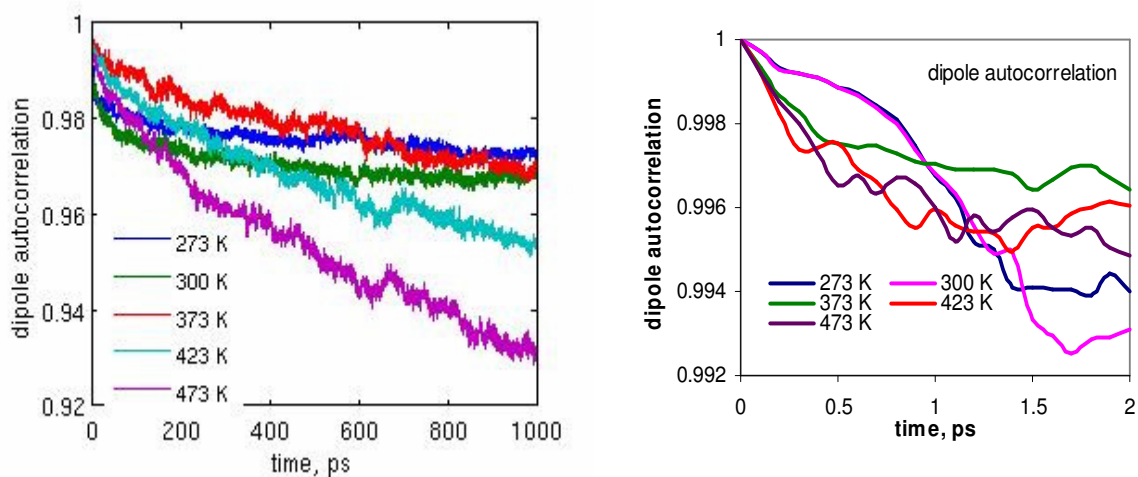
Fig. 6.20 Dipole auto correlation function at different temperature

The dipole autocorrelation function for lower temperatures 273 and 300 K shows the characteristic two stage/phase relaxation of supercooled liquid. In the initial stage/phase the decay of the autocorrelation is faster and it is followed by a slowly decaying tail in the second phase. The autocorrelation function was fitted to double exponential function of the form:

$$\phi(t) = A_1 e^{(-\frac{t}{\tau 1})} + A_2 e^{(-\frac{t}{\tau 2})} \tag{6.1}$$

where A_1 and A_2 are constants and $\tau 1$ and $\tau 2$ are the relaxation times corresponding to the first and second relaxation phase.

The relaxation time constants are obtained by fitting with the above mentioned equation. These temperature variation of these time constant are presented in Fig. 6.21. As observed from the above figure, at lower temperature, the first relaxation time is in the order of 50 ps and the second relaxation time is around 147 ns. At higher temperature (473 K), the first relaxation time is ~140 ps and the second relaxation is ~2.3 ns. This indicates that the dipole relaxation is faster at higher temperature.
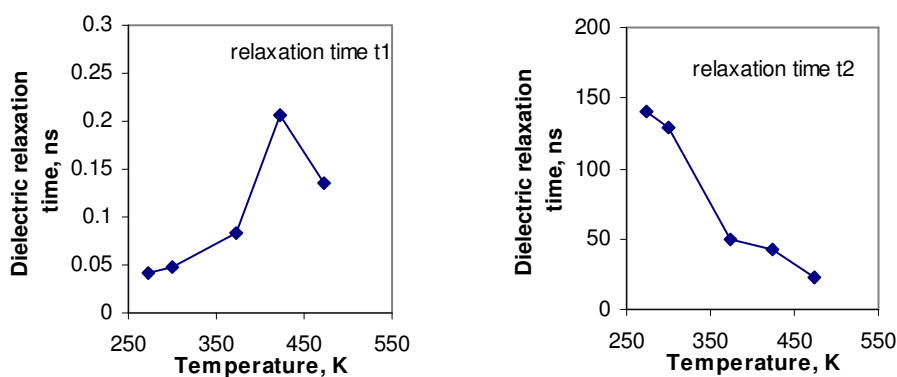
Fig. 6.21 Dipole relaxation time at different temperature

Relaxation time (τ) is also calculated using equation 2.42. It is the time integral of the orientation correlation function. Usually τ decrease with increase in temperature. By integrating the dipole time correlation function we obtained τ in the order of ~1 ns. Reported values are 4.5 ns for [BMIM][PF6] and 7.7 ns for [BMIM][BF4].[230] This indicates that the reorientation of cation is much slower and for anion it is much faster with almost friction less reorientation.[231] Others reported relaxation time of ~1.1 ns for [EMI+][PF6-] ionic liquid.[200] These relaxation times will influence the battery response times.

The relaxation time is indicative of how much time a dipole needs to reorient itself. Thus this time indicates the allowable operational frequency range of the battery. When the battery is either charged or discharged at a low frequency where the operation periods (1/frequency) is longer than the relaxation time, then the dipoles will remain fully oriented and allow proper battery operation, which means at higher frequencies greater than the relaxation time, the battery will not operate properly.

The dielectric continuum model that describe the frequency dependent dielectric response of polar molecules, miss a considerable part of fast solvation dynamics of ionic liquids.[232] It has been predicted that there exist an unrevealed dielectric response process in ionic liquid in terahertz region.[233] This may give insight in the ultra fast process in ionic liquid. From the molecular simulation the fastest relaxation time that we could capture here is in the range of ~40 ps giving rise to a frequency response in terahertz range. During MD simulation, data collection was done in every 0.1 ps. By collecting simulation data at even smaller time step may reveal even faster relaxation process which may not be available by experimental methods.

6.2.4.2 Dielectric constant

Dipole autocorrelation may be used to calculate dielectric constant (ε) of the medium at different temperatures using Clausius- Mossotti Equation (equation 2.41). This is shown in Fig. 6.22.
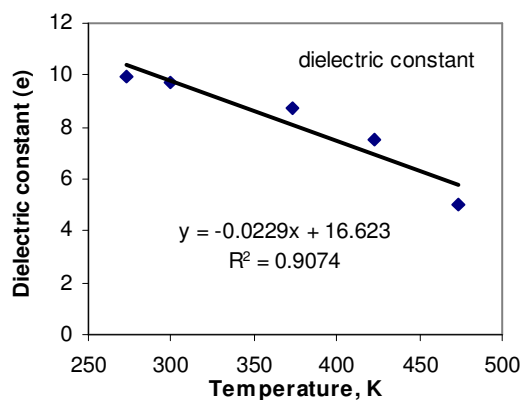
Fig. 6.22 Dielectric constant at different temperature

The value at room temperature is 9.71, which match well with other reported value.[231] Usually all molecular liquids have negative $(d\varepsilon/dT)$ value.[232] This is because density of the dipoles decreases as temperature increases.

6.2.5 Viscosity

Viscosity was calculated using the equilibrium fluctuation of the off-diagonal components of the stress tensor using equation 2.35. This carried out in a three step computation process. First, pressure to pressure autocorrelation of off-diagonal components across different times were computed considering different time origin points. Then, the autocorrelation figures of the off diagonal terms were averaged to encompass greater number of samples and obtain higher quality auto-correlation figures. Finally, block averaging of the autocorrelation function was done for different time segments. Fig. 6.23 shows the variation of the calculated shear viscosity with temperature. The shear viscosity for 300 K was 236.05 mPa.s whereas the experimental value is 219 mPa.s.[172] The trend shows decrease in viscosity with increase in temperature.
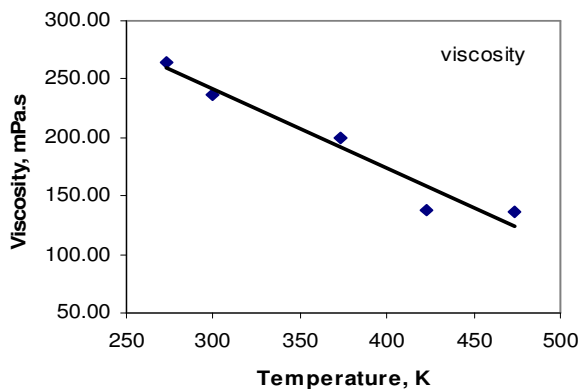
Fig. 6.23   Viscosity profile with temperature

6.3   Behavior on surface and under confinement

In Li ion battery, the ionic liquid will come in contact with the positive and negative electrodes. Graphite is primarily used as a negative electrode in Li ion battery. Therefore we tried to understand the IL behavior on graphite surface and also in nano confinement where the IL ions are interposed between two electrode surfaces having separation in order of 6.5 nm in the Z direction. Ionic liquid consisting of 800 ion pairs were placed on graphite surface in one system (which hence forth we would denote as the 'surface system') and in the other system, called the 'confinement system', we placed the liquid ions between two surfaces. Both these systems were subjected to MD simulation using various ensembles. Fig. 6.24 presents snapshots of both these systems, which shows the position of the ions and surface atoms. The left panel of Fig. 6.24 shows the surface system and the right one shows the confinement system. In Fig. 6.24, the blue spheres represent the non polar regions (alkyl chain of the cation) and the yellow spheres represents polar regions (anion and the imidazole ring). As observed from this figure, there is clustering in the polar and non polar domains in the liquid.
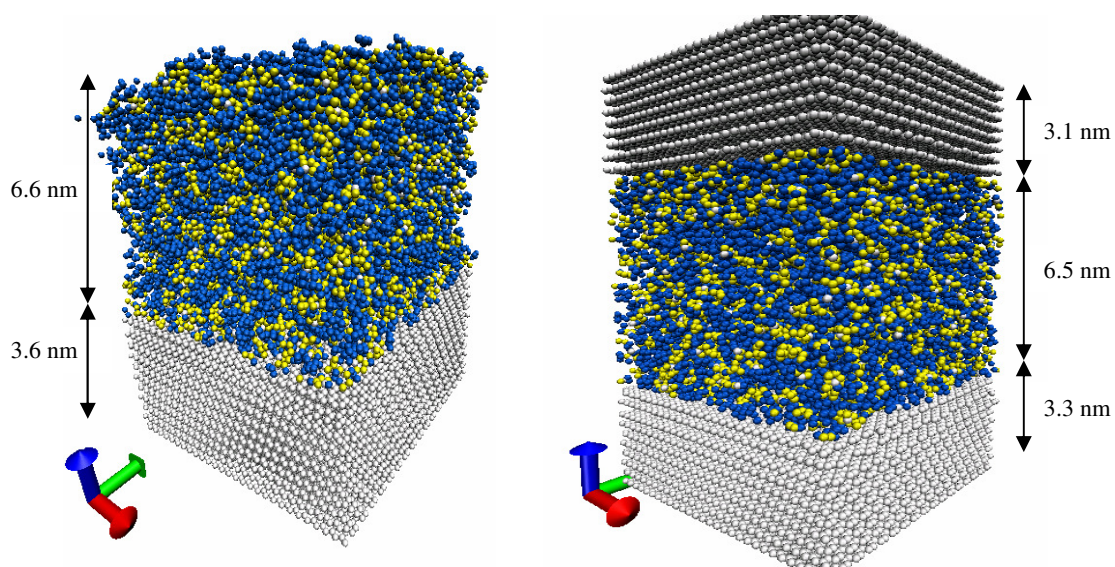
Fig. 6.24 Structure of ionic liquid on graphite surface and in confinement

6.3.1 Density profile

In the system where the IL is on the graphite surface, the ion density profile is calculated at different distance along Z direction (the direction orthogonal to the electrode surface) and the results are shown in Fig. 6.25 (the figure at the left). The ion density in the immediate vicinity of the graphite surface is high. Within the IL layer, the density profile of all ions considered together shows an oscillatory nature. This is similar to the observations by others.[167,182] At the free liquid surface the density is also slightly higher compared to the locations within the IL layer. The density profile of cations and anions considered separately also shows oscillatory nature (the figure at right in Fig. 6.25).
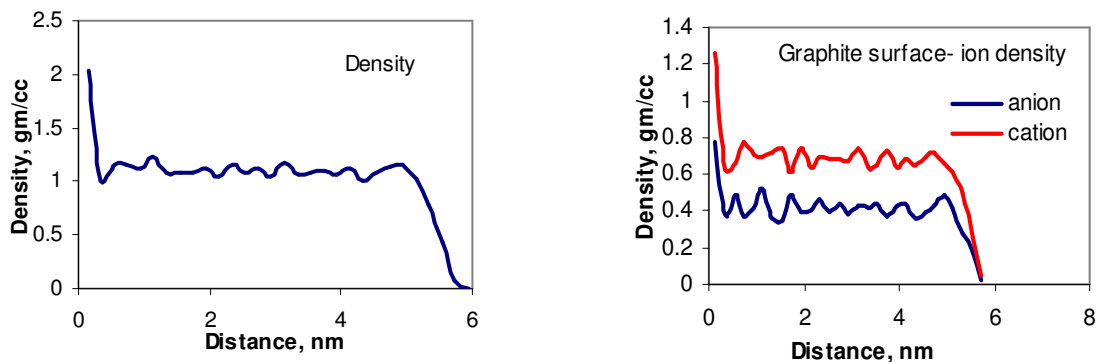
Fig. 6.25 Density profile of ionic liquid on graphite in the surface system

The variation of the ion density on Z direction for all ions considered together and cations and anion considered separately are presented in Fig. 6.26. The ion density shows similar oscillatory nature (the figure at the right of Fig. 6.26). Individual cation and anion density are also similar and shows high peaked oscillatory profile at the vicinity of the graphite interface (at left of Fig. 6.26).
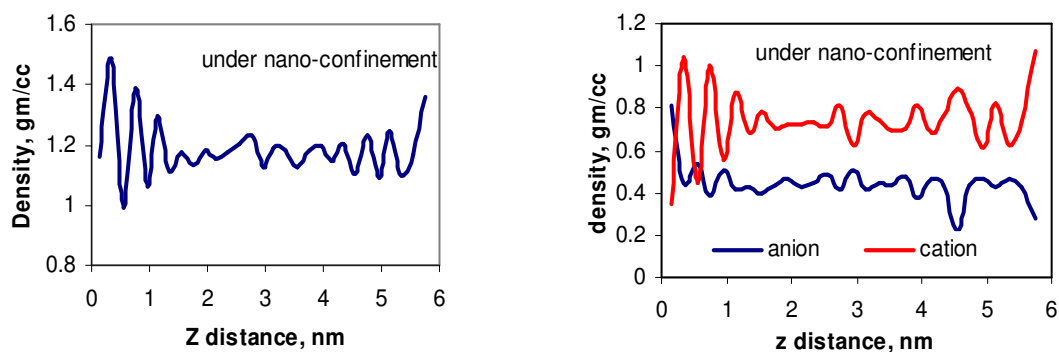
Fig. 6.26 Density profile of ionic liquid in nano confinement

From this figure, we also observe another phenomenon. The density profile show an alternating behavior, meaning the areas where cation density is high, those have lower anion density and vice versa.

The radial distribution function also shows that the density of both ion species are very high near the graphite surfaces (Fig. 6.27). This is because of high coordination number for the ions and closely packed structure on the surface.
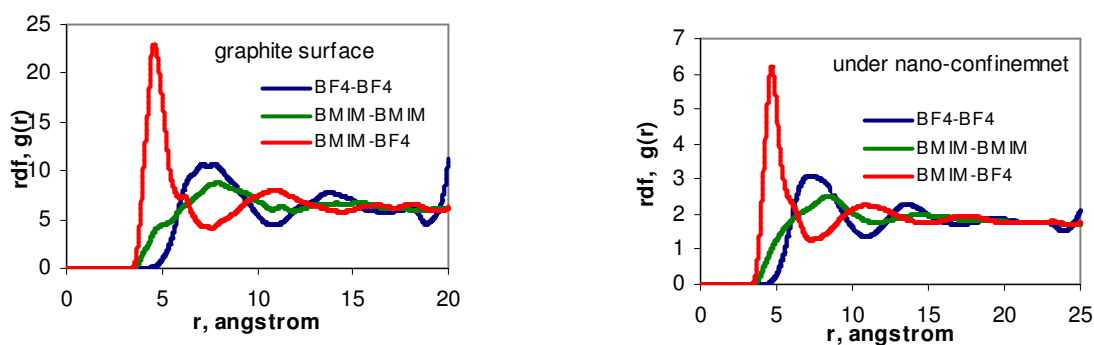
Fig. 6.27 Radial distribution function of ionic liquid on surface and in confinement

6.3.2 Orientation on surface

The orientation of ionic liquid molecules on both kinds of surfaces (IL to vapor interface, IL to solid interface) as obtained from the snapshot from the simulation are presented in Fig. 6.28. At the free surface (top panel of Fig. 6.28) the alkyl tail of the cations protrude outwards as observed by other researchers.[178] Due to π-π interaction the imidazole ring of the cation lie flat on the graphite surface (middle and bottom panel). This behavior has also been observed by others.[180]

Free surface (vacuum)

Butyl chains
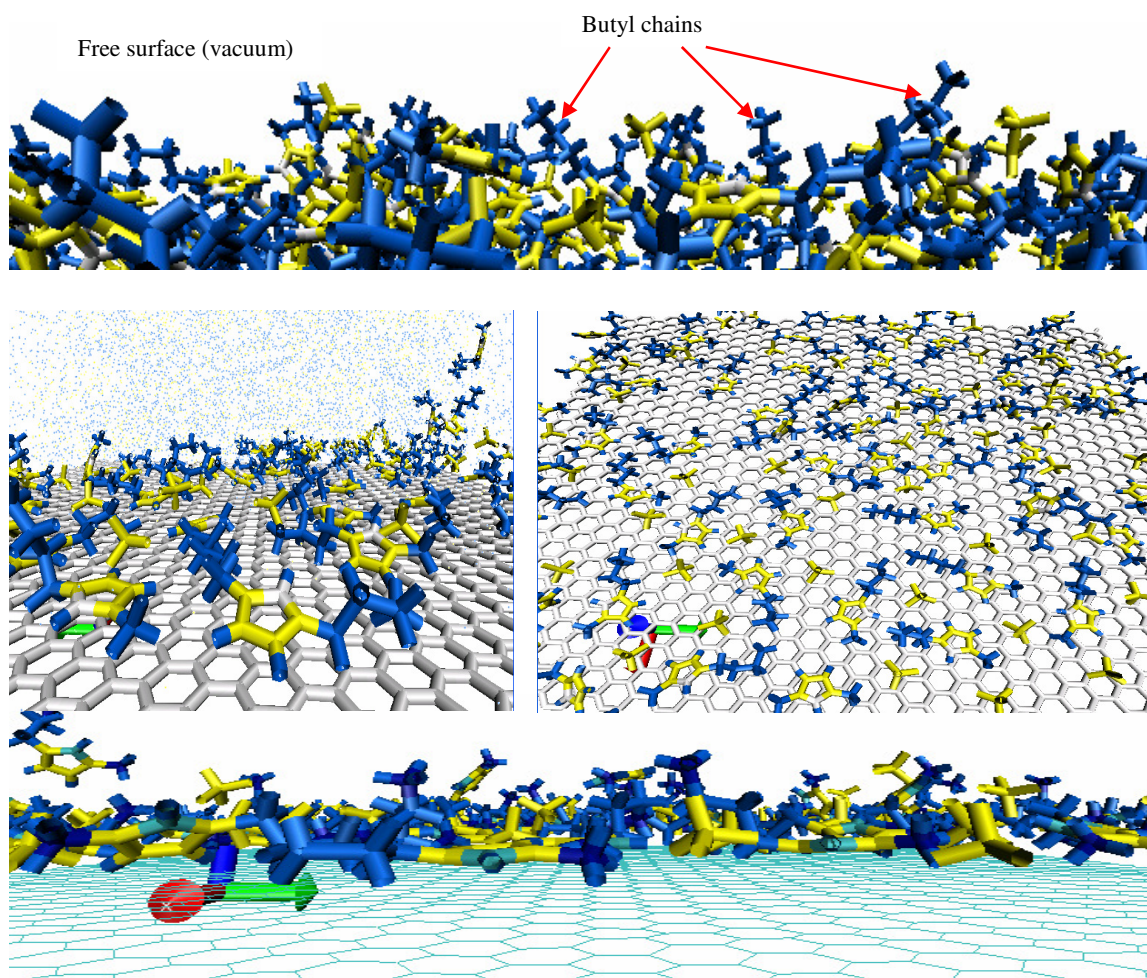
Fig. 6.28   Ion orientation on IL/graphite surface and IL/vacuum interface

6.3.3   Diffusion coefficient on the surface and interface

The mean square displacements of cations and anions on the XY and Z directions at different times, in the surface system are presented in Fig. 6.29. The same for the nano confinement system are presented in Fig. 6.30. For the surface system, for both *XY* and *Z* directions, first, there is a ballistic zone followed by a brief diffusive zone (the flat region). This flat region indicates that the ions are trapped in that zone.
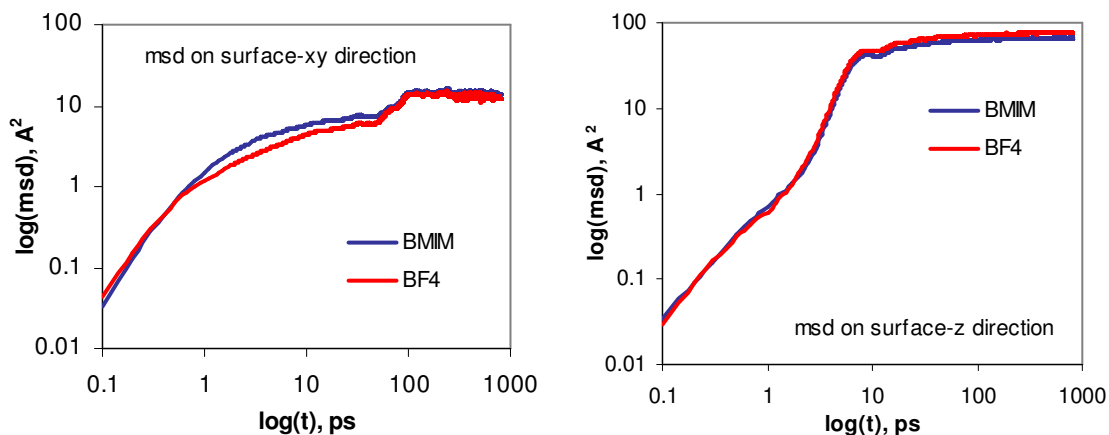
Fig. 6.29 Mean square displacement in the surface system
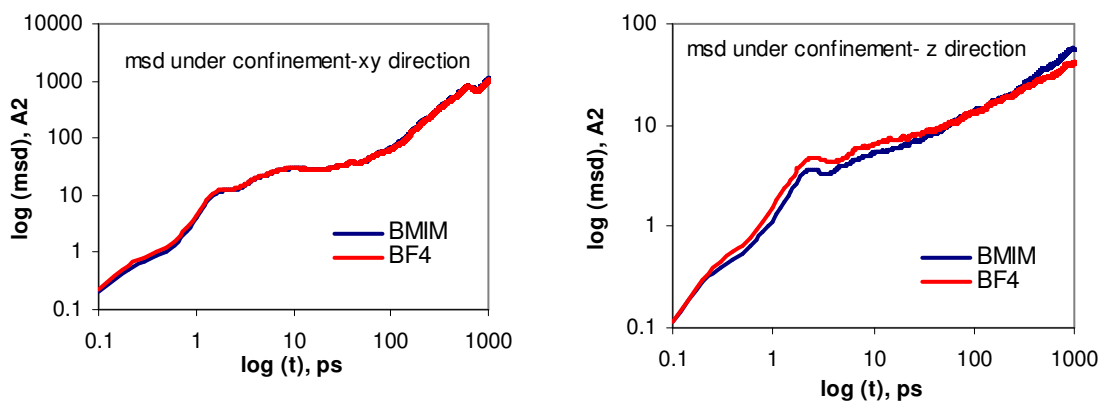
Fig. 6.30 Mean square displacement in the nano confinement system

For both, surface and confinement systems (Fig. 6.29 and Fig. 6.30), the diffusion is high compared to the diffusion in the bulk liquid system. In the surface system, the diffusion on *Z* direction is higher compared to that in the *XY* direction near the IL-vapor interface.

In the confinement system, near the graphite surface the diffusion in *XY* direction is higher than that in the *Z* direction. This is because the graphite surface is smooth and thus provides friction

less movement on the surface. But in Z direction due to presence of inter-ionic interactions (salvation shells) the diffusion is less.

The diffusion coefficients of all the ions in all three cases: bulk liquid system, surface system and the confinement system are presented in Table 6.4. It is evident that the diffusion in the surface system is lower compared to the diffusion in the confinement system. It may be due to the fact that in the confinement system, the potential fields from both surfaces influence the diffusion of the ions confined within the surfaces. Cation has higher diffusion in the confinement system and in the bulk system for both XY and Z directions. But in the surface system, in the Z direction, the cation has less diffusion. Others have also found higher diffusion on surface and confinement system compared to the bulk system for other ionic liquids.[189,191]

Table 6.4 Comparison of diffusion coefficient in bulk, on surface and under confinement

Ion type	Bulk liquid	Surface system		Confinement system	
	$D\ (m^2/sec)$	$D\ (m^2/sec)$		$D\ (m^2/sec)$	
		XY direction	Z direction	XY direction	Z direction
BMIM	9.5×10^{-12}	1.43×10^{-10}	5.64×10^{-10}	2.55×10^{-9}	2.58×10^{-10}
BF4	7.0×10^{-12}	1.44×10^{-10}	6.57×10^{-10}	2.42×10^{-9}	1.64×10^{-10}

6.3.4   Dipole autocorrelation on the surface and in nano confinement

Dipole autocorrelation was calculated for the IL ions at the surface and under confinement. The autocorrelation function decay faster compared to that for the bulk liquid. The autocorrelation function was fitted to triple exponential function (equation 2.43). The relaxation times are provided in Table 6.5 below.

Table 6.5 Comparison of dipole relaxation time

Systems	$\tau1$(ps)	$\tau2$ (ps)	$\tau3$ (ps)
Bulk	47.89272	129466.6	
Surface	60.82725	597728.6	
Under nano confinement (fitted to double exponential equation)	235.2941	6253.909	
Under nano confinement (fitted to triple exponential equation)	213.4927	4.353505	6439.15

The relaxation time constants for ions at surface and under nano confinement are faster than that of the bulk ionic liquid. The relaxation time for ions on the surface is even longer than that of those in the bulk liquid. This may be compared with the behavior of water. In case of water confined between narrow channels, the relaxation time varies depending on the channel distance, with wider channel giving higher relaxation time than bulk.[234] This is probably due to increased interaction and constrained movement in the confinement. The similar phenomena may have happened here.

6.4   Properties of IL-LiBF$_4$ mixture

6.4.1   Ion coordination

Ionic Liquid Li salt mixture can give us information about nano structure formation and the state of lithium in it.[235] We conducted this study with three concentrations of LiBF4 salt: with 0.33 mol/kg, 1 mol/kg and for 2 mol/kg. Density of the mixture in these three cases are: 1.15 gm/cc, 1.22 gm/cc and 1.33 gm/cc respectively. From radial distribution function, we found that the Li ion coordination number is very high compared to other ions. The results are shown in Fig. 6.31. Similar observation has been made by others for other ionic liquids.[236] Li transport occurs by

ligand exchange and by 'hopping mechanism'. In this mechanism Li disrupts one coordination shell and hops to the next one.[236]
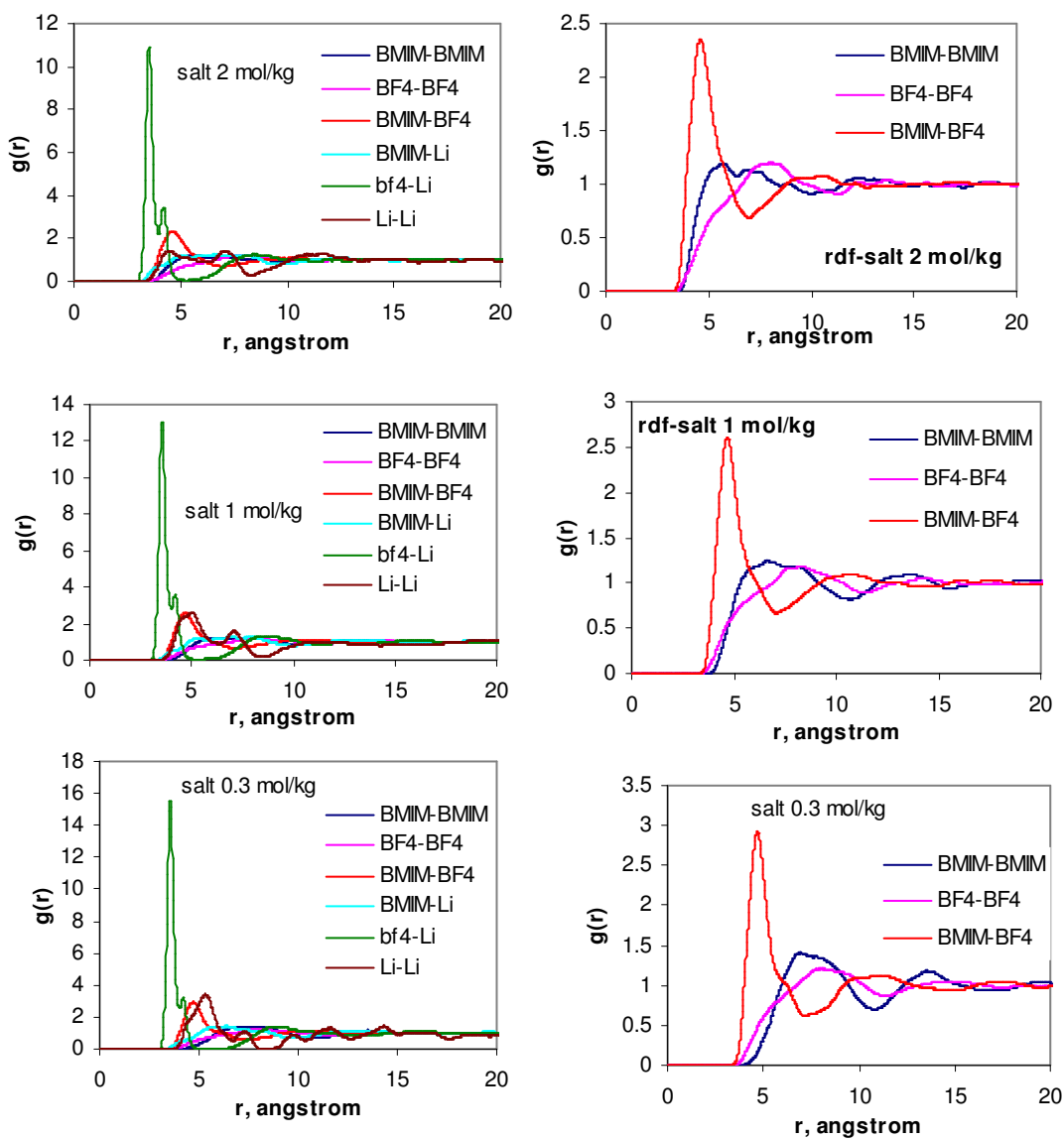
Fig. 6.31 Effect of salt on ion coordination

6.4.2   Diffusion

We studied the Li diffusion in the ionic liquid ad Li salt mixture. Diffusion coefficients for 1 mol/kh mixture for different ions are as follows (Table 6.6). For BMIM it is ~24.7x10^{-12} m^2/s, for BF4 it is ~24.3x10^{-12} m^2/s and for Li$^+$ it is 23.3 x10^{-12} m^2/s. These values were obtained from the slope of the MSD vs time plot (Fig. 6.32) and using Einstein relation. The values for 2 mol/kg mixture are: for BMIM ~15.7x10^{-12} m^2/s, for BF4 ~15.5x10^{-12} m^2/s and for Li it is 15.6 x10^{-12} m^2/s. The diffusion coefficients at different Li salt mixtures having different concentrations are higher than that of pure liquid (Table 6.6) but lower than the values for ions in the bulk liquid and in confinement.

Table 6.6   Comparison of diffusion coefficient in different salt mixture

Systems	D1 (BMIM) m^2/sec	D2 (BF4) m^2/sec	Li$^+$ m^2/sec
Bulk Liquid	9.50 x10^{-12}	7.00 x10^{-12}	
Mixture with salt at 0.33 mol/kg	5.33 x10^{-12}	4.33 x10^{-12}	3.33 x10^{-12}
Mixture with salt at 1 mol/kg	2.47 x10^{-11}	2.43 x10^{-11}	2.33 x10^{-11}
Mixture with salt at 2 mol/kg	1.57 x10^{-11}	1.55 x10^{-11}	1.57 x10^{-11}

The MSD trend shows the characteristic ballistic zone at the beginning followed by a sub diffusive zone and a diffusive zone similar to that of the pure ionic liquid. Unlike in case of pure liquid, where cation has higher diffusion, in case of the IL-Li salt mixture, all three ions have similar values for diffusion. This may be due to the fact that the anions tend to coordinate with Li$^+$ ion thus they are not trapped in the alkyl chains and are free to move similar to the cation. The mixture with 1 mol/kg salt has higher diffusion coefficient than the mixture with 2 mol/kg salt. This is probably because higher salt concentration has higher viscosity and thus reduced diffusion. Although a general trend in observations by other researchers is that there is a decrease in diffusion with increase Li concentration.[236] However there are reports[237] which indicate there

is an increase in Li transference number (ratio of total Li^+ diffusion and the total ion diffusion) with increase in Li ion concentration. Increase in Li number density and Li diffusion compared to other ions may increase Li transference number. This is more pronounced for non crystal forming IL.[237] [BMIM][BF4] IL does not form crystal and we have used a higher Li+ concentration compared to other study. This may be the reason of observing higher diffusion in our study.
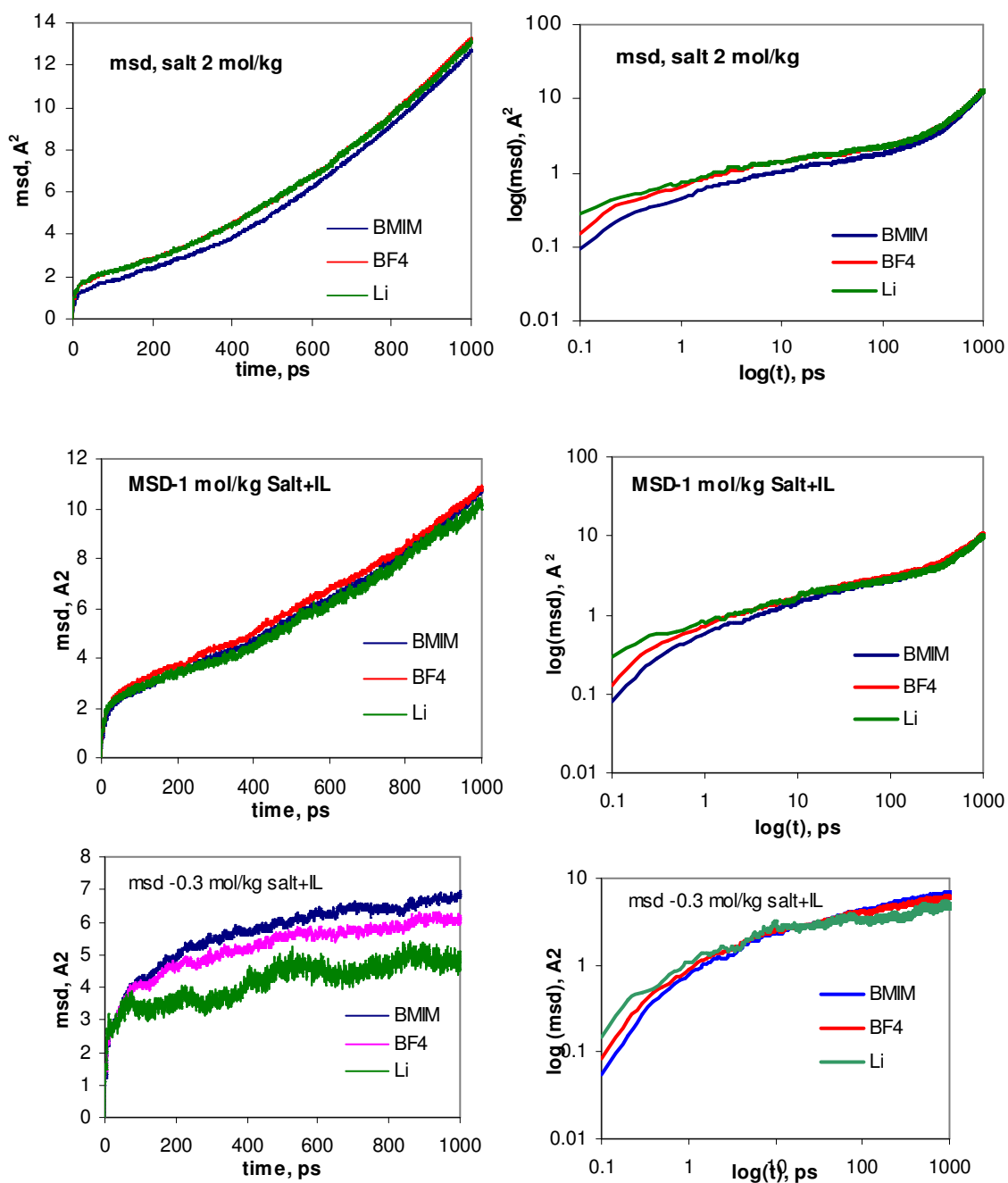
Fig. 6.32 Diffusion of salt containing ionic liquid

6.5   Summary

Ionic liquids are being considered as alternative electrolytes in lithium batteries to improve battery performance and safety. Our theoretical studies identify properties of a model ionic liquid ([BMIM][BF4]) to help facilitate this application. In this studies we have used a parameterized CVFF forcefield to study the bulk behavior, property on surface and under confinement and when mixed with Li salt. We have calculated equilibrium thermodynamic and transport properties of this IL and found that the computed values match well with the reported values. The temperature dependence of diffusion coefficient, dielectric coefficient, viscosity and conductivity were also similar to the values as reported in the literature. The temperature dependence of diffusion constant indicates a behavior that is similar to supercooled liquids. We observed the characteristic oscillatory density profile of liquid and ions on surface and under confinement. There is an order of magnitude increase in diffusion coefficient and in the dipole relaxation times of the ions on surface and under confinement. The result with Li salt mixture shows higher coordination for Li^+ with the anion, BF4. The Diffusion constant at low Li^+ concentration was less that the bulk liquid ion diffusion, but as the Li^+ concentration is increased, diffusion tend to decrease probably due to increase in viscosity. These also indicate that, using a parameterized CVFF forcefield it is possible to suitably model the [BMIM][BF4] ionic liquid behavior under different physicochemical conditions and satisfactory observations can be obtained.

CHAPTER VII

CONCLUSION

7.1   Contribution of this dissertation

In this dissertation theoretical calculations have been employed to characterize various nanoporous materials for application in hydrogen storage and an imidazole based ionic liquid for application in Li ion battery. In the following paragraphs we explain the contribution of these studies.

Carbon nanotubes are potential hydrogen storage materials because of large surface area and high sorbate-surface interaction energy due to curvature effect. However, single wall carbon nanotubes bundle up tightly, so most of their surface areas become inaccessible for adsorption. As a solution, spacer molecules can be used to hold the tubes at distance from each other in a scaffolded structure. Here, using grand canonical Monte Carlo simulation, we show that scaffolds can achieve high sorption capacity. We studied the effects of spacer/linker distance and tube diameter on the sorption capacity in (6,6), (9,9), (12,12), (15,15), (18,18) and (21,21) tube scaffolds having linker distances along c-axis ranging from 8.14 Å to 24.4 Å. Surface functionalization and Li^{+1} ion incorporation in nanotube scaffolds can further increase adsorption capacity. Therefore, we studied the effect of surface functionalization and Li^{+1} ion incorporation in nanotube scaffolds. In all these cases we also reported the thermodynamics of sorption based on isosteric heat. This is the first study on different carbon nanotube scaffolds architecture that combines sorption thermodynamics with structural variations.

Metal organic frameworks are highly porous crystalline structures that are also considered as potential hydrogen storage materials. MOFs may encounter high pressures in gas storage and separation applications. Hence we studied MOFs' behavior under high pressure to understand their behavior in such situations. Under high pressure, MOFs are susceptible to flexible structural transformations under the influence of external stimuli and there may be change in MOFs' mechanical stability and structural behavior. Although guest dependent flexible transformations has been observed for several MOFs, but studies on pressure induced transformation is limited. In this study, we presented high pressure induced reversible structural transformation of 6 isoreticular MOFs: IRMOF-1. IRMOF-3, IRMOF-6, IRMOF-8, IRMOF-10 and IRMOF-14. Using molecular simulations we showed that at high pressure these MOFs deformed to ~50% of their original volume. This deformation is due to reorganization of the linkers and ZnO_4 tetrahedra. There is a large torsion along the dihedral angle O-C-C-C. Structural transformations for MOFs with smaller organic linkers such as benzene or substituted benzene and naphthalene are reversible in pressure range of 150-250 MPa as opposed to the MOFs with larger or longer linkers. This is the first study that illustrates the high pressure deformation process in isoreticular series of MOFs.

Ionic liquids have a potential to increase energy storage capacity, environmental friendliness and safety of Li ion batteries when used as an alternative electrolyte. To help such application, we studied [BMIM][BF4] Ionic liquid properties in bulk, on graphite surface, in nano confinement and when mixed with Li salt. These studies used molecular dynamic simulations using a parameterized CVFF forcefield. The temperature dependence of diffusion coeffecient indicated a behavior that is similar to supercooled liquids. The behavior on surface and under confinement showed higher diffusion compared to the diffusion in bulk. We also observed the characteristic

oscillatory density profile of liquid and ions on surface and under confinement. There is an order of magnitude increase in diffusion coefficient and in the dipole relaxation times of the ions. The result with Li salt mixture shows higher coordination for Li^+ with the anion, BF4. The Diffusion constant at low Li^+ concentration was less that the bulk liquid ion diffusion, but as the Li^+ concentration is increased, diffusion decreased probably due to increase in viscosity. This is the first study on the behavior of this ionic liquid on surface and in confinement.

7.2   Suggested future research directions

Similar to the covalently linked carbon nanotube scaffold, other new architectures such as cross linked graphene, fullerene decorated graphene may be explored for gas storage purpose. Transition metals decorated carbon nanotube scaffold may be studied to see the effectiveness for gas storage. These investigations will need development of new theories and forcefields for carbon and grapheme based materials.

MOF structures have a rich variety in chemistry and architecture and are expected to show different phase behavior, stability, mechanical property. Thus other MOF structures may be explored in a similar way. Development of a forcefield that can accurately predict general behavior of this class of porous materials is also important in these studies. Similar to zeolite materials, application of specific forcefield for MOF structure will be beneficial to screen a large amount of these crystal structures for gas storage, and other applications.

Ionic liquid behavior on charged surfaces such as mica may be studied. This will require suitable potentials that can effectively capture the IL-mica interaction. The behavior on graphite intercalated compounds may also be studied. Solid electrolyte interface (SEI) formation using reactive forcefield may be another area to explore.

REFERENCES

1.   Simon, P.; Gogotsi, Y. *Nat. Mater.* **2008**, *7*, 845.

2.   White B.E.Jr. *Nature Nanotech.* **2008**, *3*, 71.

3.   Arico, A.S.; Bruce, P.; Scrosati, B.; Tarascon, J-M.; Schalkwijk, W.V. *Nat. Mater.* **2005**, *4*, 366.

4.   Schlapbach , L.; Züttel A. *Nature*, **2001**, *414*, 353.

5.   Satyapal, S.; Petrovic, J.; Read, C.; Thomas, G.; Ordaz, G. *Catalysis Today*, **2007**, *120*, 246.

6.   Bessel, U., *Proce. of the IEEE*, **2006**, *94*, 1826.

7.   Dillon, A. C.; Jones, K. M.; Bekkedahl, T. A.; Kiang, C. H.; Bethune, D. S.; Heben, M. J. , *Nature* **1997**, *386*, 377.

8.   Ströbel, R.; Garche, J.; Moseley, P.T.; Jörissen, L.; Wolf, G. *J. Power Sources* **2006**, *159*, 781.

9.   Liu, C.; Fan, Y. Y.; Liu, M.; Cong, H. T.; Cheng, H. M.; Dresselhaus, M. S., *Science* **1999** *286*, 1127.

10.   Chen, P.; Wu, X.; Lin, J.; Tan, K. L. *Science* **1999**, *285*, 91.

11.   Darkrim, F.; Levesque, D., *J. Chem. Phys.* **1998**,*109*, 4981.

12.   Murata, K.; Kaneko, K.; Kanoh, H.; Kasuya, D.; Takahashi, K.; Kokai, F.; Yudasaka, M.; Iijima, S. *J. Phys. Chem. B* **2002**, *106*, 11132.

13.   Kuc, A.; Zhechkov, L.; Patchkovskii, S.; Seifert, G., Heine, T. *Nano Lett.* **2007**, *7*, 1.

14.   Dimitrakakis, G.; Tylianakis, E.; Froudakis, G. *Nano Lett.* **2008**, *8*, 3166.

15.   Kostov, M.K.; Cheng, H.; Cooper, A.C.; Pez, G.P. *Phys. Rev. Lett.* **2002**, *89*, 146105.

16.   Pradhan, B. K.; Sumanasekera, G. U.; Adu, K. W.; Romero, H. E.;   Williams, K. A.; Eklund, P. C. *Physica B: Cond. Matter* **2002**, *323*, 115.

17.   Leonard, A.D.; Hudson, J.L.; Fan, H.; Booker, R.; Simpson, L. J.; O'Neill, K. J.; Parilla, P. A.; Heben, M. J.; Pasquali, M.; Kittrell, C.; Tour, J. M. *J. Am. Chem. Soc*. **2009**, *131*, 723.

18.   Wang, Q.; Johnson, K. *J. Phys. Chem. B* **1999**, *103*, 4809.

19. Wang, Q.; Johnson, K. *J. Chem Phys*. **1999**, *110*, 577.

20. Darkrim, F.; Levesque, D. *J. Phys. Chem. B* **2000,** *104*, 6773.

21. Weck, P. F.; Kim, E.; Balakrishnan, N.; Cheng, H.; Yakobson, B. I. *Chem. Phys. Lett.* **2007**, *439*, 354.

22. Bahr, J.L.; Tour, J.M. *J. Mater. Chem.* **2002**, *12*, 1952.

23. Shiraishi, M.; Takenobu, T.; Ata, M. *Chem. Phys. Lett*. **2003**, *367*, 633.

24. Liu, W.; Zhao, Y. H.; Li, Y.; Jiang Q.; Lavernia, E. J. *J. Phys. Chem. C* **2009**, *113*, 2028.

25. Deng, W-Q; Xu, X; Goddard, W.A. *Phys. Rev. Lett.* **2004**, *92*, 166103.

26. Yildirim, T.; Ciraci, S. *Phys. Rev. Lett.* **2005**, *94*, 175501.

27. Li, H.; Eddaoudi, M.; O.Keeffe, M.; Yaghi, O. M. *Nature*, **1999**, *402*, 276.

28. Eddaoudi, M.; Kim, J.; Rosi, N.; Vodak, D.; Wachter, J.; O'Keeffe, M.; Yaghi, O. M. *Science* **2002**, *295*, 469.

29. Rosi, N.; Eckert J., Eddaoudi M.; Vodak D.T.; Kim J.; O'Keeffe, M.; Yaghi, O. M *Science* **2003**, *300*, 1127.

30. Rowsell, J. L.C.; Yaghi, O. M. *Angew. Chem. Int. Ed*. **2005**, *44*, 4670.

31. Ferey, G. *Chem. Soc. Rev*. **2007**, *37*, 191.

32. Wu, C-D.; Lin, W. *Angew. Chem. Int. Ed.* **2005**, *44*, 1958.

33. Chandler, B.D.; Enright, G. D.; Udachin, K. A.; Pawsey, S.; Ripmeester, J.A.; Cramb, D. T.; Shimizu, G. K. H.   *Nat. Mater.* **2008**, *7*, 229.

34. Llewellyn, P. L.; Maurin, G.; Devic, T.; Loera-Serna, S.; Rosenbach, N.; Serre, C.; Bourrelly, S.; Horcajada, P.; Filinchuk Y.; Ferey G. *J. Am. Chem. Soc.* **2008**, *130*, 12808.

35. Chapman, K. W.; Halder, G. J.; Chupas P. J. *J. Am. Chem. Soc.* **2008**, *130*, 10524.

36. Spencer, E. C.; Angel, R. J.; Ross, N. L.; Hanson, B. E. and Howard, J. A. K. *J. Am. Chem. Soc.* **2009**, *131*, 4022.

37. Han, S. S.; Goddard III, W. A. *J. Phys. Chem. C* **2007**, *111*, 15185.

38. Mattesini, M.; Soler, J. M.; Yndurain, F. *Phys. Rev. B* **2006**, *73*, 094111.

39. Samanta, A.; Furuta, T.; Li, J. *J. Chem. Phys*. **2006**, *125*, 084714.

40. Zhou, W.; Yildirim, T. *Phys. Rev. B* **2006**, *74*, 180301.

41. Bahr, F.D.; Reid, J. A.; Mook, W. M.; Bauer, C. A.; Stumpf, R.; Skulan, A. J.; Moody, N. R.; Simmons, B. A.; Shindel, M. M.; Allendorf, M. D. *Phys. Rev. B* **2007**, *76*, 184106.

42. Gatta, G. D. *Z. Kristallogr*. **2008**, *223*, 160.

43. Armand, M.; Endres, F.; MacFarlane, D.R.; Ohno, H.; Scrosati, B., *Nat. Mater.* **2009**, *8*, 621.

44. Morris, R. E.; Wheatley, P. S. *Angew. Chem. Int. Ed.*, **2008**, *47*, 4966 .

45. Kroto, H. W.; Heath, J. R.; O'Brien, S. C.; Curl, R. F.; Smalley, R. E. *Nature*, **1985**, *318*, 162.

46. Iijima, S. *Nature*, **1991**, *354*, 56.

47. Saito, R.; Fujita, M.; Dresselhaus, G.; Dresselhaus, M. S. *Phys. Rev. B* **1992**, *46*, 804.

48. Patchkovskii, S.; Tse, J. S.; Yurchenko, S. N.; Zhechkov, L.; Heine, T. and Seifert, G. *Proc. Natl. Acad. Sc. U S A* **2005**,*102*, 10439.

49. Rowsell, J.L.C.; Millward, A.R.; Park, K.S.; Yaghi, O.M. *J. Am. Chem. Soc.* **2004**, *126* 5666.

50. Park, K. S. Zheng, N. Côté, A. P. Choi, J. Y. Huang, R. Uribe-Romo, F. J. Chae, H. K. O'Keeffe, M. Yaghi, O. M. *Proc. Natl. Acad. Sci. U S A*. **2006**, *103*, 10186.

51. Hill, C. G. Jr. *An Introduction to Chemical Engineering Kinetics and Reactor Design*, John Wiley & Sons: New York, NY, 1977.

52. Bhatia, S.K.; Myers, A.L. *Langmuir*, **2006**, *22*, 1688.

53. Hoang, T. K. A.; Antonelli, D. M. *Adv. Ma.* **2009**, *21*, 1787.

54. Zhao, D.; Yuan D.; Zhou, H. C. *Energy Environ. Sci*., **2008**, *1*, 222.

55. Ansón, A.; Benham, M.; Jagiello, J.; Callejas, M. A.; Benito, A. M .; Maser, W. K.; Züttel, A.; Sudan, P.; Martínez, M. T. *Nanotechnology* , **2004**, *15*, 1503.

56. Han, S.S.; Mendoza-Cortes, J.L. Goddard-III, W.A., *Chem. Soc. Rev.* **2009**, *38*, 1460.

57. Wong-Foy, A. G.; Matzger, A. J.; Yaghi, O. M. *J. Am. Chem. Soc*. **2006**, *128*, 3494.

58. Xu, W. C.; Takahashi, K.; Matsuo, Y.; Hattori, Y.; Kumagai, M.; Ishiyama, S.; Kaneko, K.; Iijima S. *Int. J. Hydrogen Energy*, **2007**, *32*, 2504.

59. Frost, H.; Duren, T.; Snurr, R.D. *J. Phys. Chem. B* **2006**, *110*, 9565.

60. Thomas, K. M. *Dalton Trans*. **2009**, *9*, 1487.

61.   Rowsell, J.L.C.; Yaghi, O.M. *Angew. Chem. Int. Ed*. **2005**, *44*, 4670.

62.   Ma, S.; Eckert, J.; Forster, P.M.; Yoon, J. W.; Hwang, Y.K.; Chang, J.S.; Collier, C.D.; Parise, J.B.; Zhou, H.C. *J. Am. Chem. Soc.* **2008**, *130*, 15896.

63.   Rowsell, J.L.C.; Yaghi, O.M. *J. Am. Chem. Soc*. **2006**, *128*, 1304.

64.   Okamoto, Y.; Miyamoto, Y. *J. Phys. Chem. B* **2001**, *105*, 3470.

65.   Nguyen, T. X.; Cohaut, N.; Bae, J.S.; Bhatia , S. K. *Langmuir* **2008,** *24*, 7912.

66.   Rowsell, J. L. C.; Spencer, E. C.; Eckert, J.; Howard, J. A. K.; Yaghi O. M. *Science* **2005**, *309*, 1350.

67.   Pradhan, B. K.; Sumanasekera, G. U.; Adu, K. W.; Romero, H. E.; Williams, K. A.; Eklund, P. C. *Physica B: Condens. Matter* 2002, *323*, 115.

68.   Hubner, O.; Gloss, A.; Fichtner, M. and W. Klopper, *J. Phys. Chem. A* **2004**,*108*, 3019.

69.   Mueller T.; Ceder , G. *J. Phys. Chem. B* **2005**, *109*, 17974.

70.   Klontzas, E.; Mavrandonakis, A.; Tylianakis, E.; Froudakis, G.E., *Nano Lett*. **2008**, *8*, 1572.

71.   Lochan, R.; Head-Gordon, M. *Phys. Chem. Chem. Phys*. **2006**, *8*, 1357.

72.   Mavrandonakis, A.; Klontzas, E.; Tylianakis, E.; Froudakis, G. E. *J. Am. Chem. Soc*. **2009**, *131*,13410.

73.   Chui, S S.-Y.; Lo, S. M.-F.; Charmant, J. P. H.; Orpen, A. G.; Williams, I. D. *Science* **1999**, *283*, 1148.

74.   Ma, S.; Zhou, H.C. *J. Am. Chem. Soc.* **2006**, *128*, 11734.

75.   Dinca, M.; Dailly, A.; Liu, Y.; Brown, C.M.; Neumann, D. A. and Long, J. R. *J. Am. Chem. Soc.* **2006**,*128*, 16876.

76.   Liu, Y.; Kabbour, H.; Brown, C. M.; Neumann, D. A.; Ahn, C. C. *Langmuir* **2008**, *24*, 4772.

77.   Nijem, N.; Veyan, J-F.; Kong, L.; Li, K.; Pramanik, S.; Zhao, Y.; Li, J.; Langreth, D.; Chabal, Y. J. *J. Am. Chem. Soc.* **2010**, *132*, 1654.

78.   Zhou, W.; Yildirim, T., *J. Phys. Chem. C* **2008**, *112*, 8132.

79.   Blomqvist A.; Moysés Araújo, C.; Srepusharawoot, P.; Ahuja, R. *Proc. Natl. Acad. Sc. U S A* **2007**, *104*, 20173.

80.   Han, S. S.; Goddard III, W.A., *J. Phys. Chem. C* **2008**, *112*, 13431.

81.   Liu, W.; Zhao, Y. H.; Li, Y.; Jiang Q.; Lavernia, E. J. *J. Phys. Chem. C*, **2009**, *113*, 2028.

82.   Wang, Q.; Sun, Q.;   Jena, P.; Kawazoe, Y. *J. Chem. Theory Comput.* **2009**, *5*, 374.

83.   Reddy, A. L. M.; Ramaprabhu, S. *Int. J. Hydrogen Energy*, **2007**, *32*, 3998.

84.   Kim, G.; Jhi, S-H.; Lim, S.; Park, N. *Phys. Rev. B*. **2009**, *79*, 155437.

85.   Li, Y. ; Yang, R. *J, Am., Chem. Soc*. **2006**, *128*, 8136.

86.   Li, Y.; Yang, R. *Langmuir*, **2007**, *23*, 12937.

87.   Lueking, A.; Yang R. T. *J. Catalysis* **2002**, *206*, 165.

88.   Volpe, M.; Cleri, F., *Chem. Phys. Lett*. **2003**, *371*, 476.

89.   Skoulidas, A.I.; Ackerman, D.M.; Johnson, J.K.; Sholl, D.S., *Phys. Rev. Lett*. **2002**, *89*, 185901.

90.   Cheng, H.; Cooper, A.C.; Pez, G.P.; Kostov, M.K.; Piotrowski, P.; Stwart, S.J. *J. Phys. Chem. B* **2005**, *109*, 3780.

91.   Müller, U.; Schubert, M.; Teich, F.; Puetter, H.; Schierle-Arndt, K. ; Pastré, J. *J. Mater. Chem.* **2006**, *16*, 626.

92.   Smith, M. R. Jr.; Bittner, E. W.; Shi, W.; Karl Johnson, J.; Bockrath, B. C. *J. Phys. Chem. B* **2003**,*107*, 3752.

93.   Banerjee, S.; Murad, S.; Puri, I. K. *Proc. of the IEEE*, **2006**, *94*, 1806.

94.   Yang, L-M.; Vajeeston, P.; Ravindran, P.; Fjellvag, H.; Tilset, M. *Inorg. Chem.* **2010**, *49,* 10283.

95.   Civalleri, B.; Napoli, F.; Noel, Y.; Roetti, C.; Dodesi, R. *Cryst. Eng. Comm.*, **2006**, *8*, 364.

96.   Zhou, W.; Wu, H.; Yildirim, T.; Simpson, J. R.; Hight Walker, A. R. *Phys. Rev. B* **2008**, *78*, 054114.

97.   Lock, N.; Wu, Y.; Christensen, M.; Cameron, L. J.; Peterson, V. K.; Bridgeman, A. J. ; Kepert, C. J.; Iversen, B. B. *J. Phys. Chem. C* **2010**, *114*, 16181.

98.   Han, S. S.; Goddard III, W. A. *J. Phys. Chem. C,* **2007**, *111*, 15185.

99.   Dubbeldam, D.; Walton, K.S.; Ellis, D.E.; Snurr, R.Q. *Angew. Chem. Int.Ed.* **2007**, *46*, 4496.

100. Mulder, F. M.; Assfour, B.; Huot, J.; Dingemans, T. J.; Wagemakerand, M.; Ramirez-Cuesta, A. J. *J. Phys. Chem. C* **2010**, *114*, 10648.

101. Walker, A.M.; Civalleri, B.; Slater, B.; Mellot-Draznieks, C.; Cor, F.; Zicovich-Wilson, C. M.; Roman-Perez, G.; Soler, J. M.; Gale, J. D. *Angew. Chem. Int. Ed.* **2010**, *49*, 7501.

102. Coombes, D. S.; Cora`, F.; Mellot-Draznieks, C.; Bell, R. G. *J. Phys. Chem. C* **2009**, *113*, 544.

103. Liu, J.; Lee, J. Y.; Pan, L.; Obermyer, R. T.; Simizu, S.; Zande, B.; Li, J.; Sankar, S. G.; Johnson, J. K. *J. Phys. Chem. C* **2008**, *112*, 2911.

104. Ferey, G.; Serre, C. *Chem. Soc. Rev.* **2009**, *38*, 1380.

105. Gascon, J.; Kaptejin, F. *Angew. Chem. Int.Ed.* **2010**, *49*, 1530.

106. Salles, F.; Kolokolov, D. I.; Jobic, H.; Maurin, G.; Llewellyn, P. L.; Devic, T.; Serre, C.; Ferey. G. *J. Phys. Chem. C.* **2009**, *113*, 7802.

107. Brown, C. M.; Liu, Y.; Yildirim, T.; Peterson, V. K.; Kepert, C. J. *Nanotechnology* **2009**, *20*, 04025.

108. Mani Biswas, M.; Cagin, T., *Mat. Chem. Phys.* **2011**, Article in Press.

109. Tan, J. C.; Bennett, T. D.; Cheetham, A. K. *Proc. Natl. Acad. Sci. U S A.* **2010**, *107*, 9938.

110. Hu Y. H.; Zhang, L. *Phys. Rev. B*, **2010**, *81*, 174103.

111. Kaye, S.S.; Dailly, A.; Yaghi, O.M.; Long, J.R. *J. Am. Chem. Soc*. **2007**, *129*, 14176.

112. Huang, B.L.; McGaughey, A.J.H.; Kavinay, M.*Int. J. Heat and Mass Transfer* **2007**, *50*, 393.

113. Cagin, T.; Che, J.; Qi, Y.; Zhou, Y.; Demiralp, E.; Gao, G.; Goddard III, W. A. *J. Nanopartlcle Res.* **1999**, *1*, 51.

114. Cramer, C. J. *Essentials of Computational Chemistry: Theories and Models*, 2nd ed. Wiley: Hoboken, NJ, 2004.

115. Siller, K.; Hofman, A.; Sauer, J. *J. Am. Chem. Soc*. **2009**, *131*, 4143.

116. Hubner, O.; Gloss, A.; Fichtner, M.; Klopper, W. *J. Phys. Chem. A* **2004**, *108*, 3019.

117. Sagara, T.; Ortony, J.; Ganz, E.J. *Chem. Phys.* **2005**,*123*, 214707.

118. Sagara, T.; Klassen, J.; Ortony, J.; Ganz E. *J. Chem. Phys.* **2005**,*123*, 014701.

119. Lochan , R.; Head-Gordon, M.*Phys. Chem. Chem. Phys*. **2006**, *8*, 1357.

120. Sagara . T.; Klassen, J.; Ganz, E. *J. Chem. Phys*. **2004**,*121*, 12543.

121. Hamel, S.; Côté, M. *J. Chem. Phys.* **2004**, *121*, 12618.

122. Han, S. S.; Deng, W-Q.; Goddard III, W. A. *Angew. Chem. Int. Ed*. **2007**, *46*, 6289.

123. Kosa, M.; Krack, M.; Cheetham, A. K.; Parrinello, M. *J. Phys. Chem. C* **2008**, *112*, 16171.

124. Sun, Y. Y.; Kim, Y-H.; Zhang, S. B. *J. Am. Chem. Soc.* **2007**, *129*, 12606.

125. Lochan, R. C.; Khaliullin, R. Z.; Head-Gordon, M. *Inorg. Chem*. **2008**, *47*, 4032.

126. Liu, J.; Rankin, R.B.; Johnson, J.K. *Mol. Simu*. 2009, *35*, 60.

127. Cha, M-H.; Nguyen, M. C.; Lee, Y-L.; Im, J.; Ihm, J. *J. Phys. Chem. C*, **2010**, *114*, 14276.

128. Fischer, M.; Kuchta, B.; Firlej, L.; Hoffmann, F.; Fro¨ba, M. *J. Phys. Chem. C* 2010, *114*, 19116.

129. Srepusharawoot, P.; Moysés C. A.; Blomqvist, A.; Scheicher, R. H.; Ahuja, R. *J. Chem. Phys.* **2008,** *129*, 164104.

130. Lee, T. B.; Kim, D.; Jung, D. H.; Choi, S. B.; Yoon, J. H.; Kim, J.; Choi, K.; Choi, S-H.*Catalysis Today* **2007**,*120*, 330.

131. Fuentes-Cabrera, M.; Nicholson, D. M.; Sumpter, B. G.; Widom, M. *J. Chem. Phys.* **2005**, *123*, 124713.

132. Hafner, J. *J. Comp. Chem.* **2008**, *29*, 2044.

133. Xu, Q.; Zhong, C. *J. Phys. Chem. C* **2010**, *114*, 5035.

134. Finsy, V.; Calero, S.; García-Pérez, E.; Merkling, P. J.; Vedts, G.; De Vos, D. E.; Baron, G. V.; Denayer, J.F. M. *Phys. Chem. Chem. Phys.* **2009**, *11*, 3515.

135. Tafipolsky, M.; Amirjalayer, S.; Schmid, R. *J. Comput Chem*. **2007**, *28*, 1169.

136. Tafipolsky, M.; Amirjalayer, S.; Schmid, R. *J. Phys. Chem. C* **2010**,*114*, 14402.

137. Tafipolsky, M.; Schmid R. *J. Phys. Chem. B* **2009**, *113*, 1341.

138. Züttel, A. *Naturwissenschaften*, **2004**, *91*, 157.

139. Diep, P.; Johnson, J. K. *J. Chem Phys.* **2000**, *112*, 4465.

140. Buch, V. *J.Chem. Phys*. **1994**, *100*, 7610.

141. Garberoglio, G.; Skoulidas, A.; I. Johnson, J.K. *J. Phys. Chem. B* **2005**, *109*, 13094.

142. Silvera, I.F. *Rev.Mod.Phys.* **1980**, *52*, 393.

143. Darkrim, F.; Levesque, D. *J. Chem. Phys.* **1998**,*109*, 4981.

144. Belof, J. L.; Stern, A. C.; Space, B. *J. Chem. Theory Comput*. **2008**, *4*, 1332.

145. Liu, J.; Culp, J. T.; Natesakhawat, S.; Bockrath, B.C.; Zande, B.; Sankar, S. G.; Garberoglio, G.; Johnson, J. K. *J. Phys. Chem. C*, **2007**, *111*, 9305.

146. Landau, D.P.; Binder, K. *A Guide to Monte Carlo Simulations in Statistical Physics*; 3rd ed. Cambridge University Press: Cambridge, UK, 2009.

147. Frenkel, D.; Smit, B.; *Understanding Molecular Simulation, from Algorithm to Applications*, Academic Press: New York, NY, 2002.

148. Allen M.P.; Tildisley, D. J. *Computer Simulation of Liquids*; Oxford University Press: New York, NY, 1989.

149. Belof, J. L.; Stern, A. C.; Eddaoudi, M.; Space, B. *J. Am. Chem. Soc*. **2007**, *129*, 15202.

150. Yang, Q.; Zhong, C.*J. Phys. Chem. B*, **2005**, *109*, 11862.

151. Han, S. S.; Goddard III, W.A. *J. Phys. Chem. C*. **2008**, *112*, 13431.

152. Wenzel, S. E.; Fischer, M.; Hoffmann, F.; Froba, M. *Inorg. Chem.* **2009**, *48*, 6559.

153. Schrock, K.; Schroder, F.; Heyden, M.; Fischer, R.A.; Havenith, M.*Phys. Chem. Chem. Phys.* **2008**, *10*, 4732.

154. Tarascan, J.M.; Armand, M. *Nature* **2001**, *414*, 359.

155. Armand, M.; Tarascan, J.M. *Nature* **2008**, 451, 652.

156. Cairns, E.J.; Albertus, P. *Annu. Rev. Chem. Biomol. Eng.* **2010**, *1*, 299.

157. Goodenough, J.; Abruna, H.D.; Buchanan, M.V. (Eds), *Basic Research Needs for Electrical Energy Storage*. DOE: Washington DC, US, 2007.

158. Mezger, M.; Schroder, H.; Reichert, H.; Schramm, S.; Ohasinski, J.S.; Schoder, S.; Honkimaki, V.; Deutsch, M.; Ocko, B.M.; Ralston, J.; Rokwerder, M.; Stratmann, M.; Dosch, H. *Science*, **2008**, *322*, 424.

159. Lewandowski, A.; Swiderska-Mocek, A. *J. Power Source*, **2009**,*194*, 601.

160. Tsuda, T; Hussey, C.L. *Electrochem. Soc. Interface*, Spring **2007**, 42.

161. Macfarlane, D.R.; Pringle, J.M.; Howlett, P.C.; Forsyth, M. *Phys.Chem.Chem.Phys.* **2010**, *12*, 1659.

162. Smith, G.D.; Borodin, O.; Russo, S.P.; Rees, R.J.; Hollenkamp, A. F. *Phys. Chem.Chem. Phys.* **2009**, *11*, 9884.

163. Guerfi, A.; Duchesne, S.; Kobayashi, Y.; Vijh, A.; Zaghib, K. *J.Power Source*, **2008**,*175*, 866.

164. Sakaebe, H.; Matsumoto, H.; Kuniaki, T. *Electrochimica Acta.*, **2007**, *53*, 1048.

165. Hansen, J.P.; MaDonald, I.R. *Theory of Simple Liquid*; 3rd ed. Academic Press: London, 2006.

166. Roy, D.; Patel, N.; Conte, S.; Maroncelli, M. *J.Phys.Chem.B* **2010**, *114*, 8410.

167. Hayes, R..; El Abedin, A.Z.; Atkin, R. *J. Phys. Chem B*. **2009**, *113*, 7049.

168. Holbrey, J.D.; Rogers, R.D. in *Ionic Liquids in Synthesis*; 2nd Ed. Wasserscheid, P., Welton, T., (Eds.) Ch 3, 57, Wiley-VCH, Weinheim, Germany, 2008.

169. Fredlake, C. P.; Crosthwaite, J. M.; Hert, D.G.; Aki, S.N. V. K.; Brennecke, J. F., *J. Chem. Eng. Data* **2004**, *49*, 954.

170. Maginn, E.J. *J.Phys.: Condens. Matters* **2009**, *21*, 373101.

171. del Popolo, M.; Voth , G.A. *J.Phys. Chem. B*, **2004**, *108*, 1744.

172. Mantz, R.A.; Trulove, P.C., in *Ionic Liquids in Synthesis;* 2nd Ed. Wasserscheid, P., Welton, T., (Eds.) Ch 3, 72, Wiley-VCH, Weinheim, Germany, 2008.

173. Cocalia, V.A.; Visser, A.E.; Rogers, R.D.; Holbrey, J.D. in *Ionic Liquids in Synthesis*; 2nd Ed. Wasserscheid, P., Welton, T., (Eds.) Ch 3, 89, Wiley-VCH, Weinheim, Germany, 2008.

174. Welton, T., in Ionic Liquids in Synthesis, 2nd Ed. Wasserscheid, P., Welton, T., (Eds.) Ch 3, 129, Wiley-VCH, Weinheim, Germany, 2008.

175. Trulove, P.C.; Mantaz, R.A., in *Ionic Liquids in Synthesis*, Second Ed. 2nd Ed. Wasserscheid, P., Welton, T., (Eds.) Ch 3, 141, Wiley-VCH, Weinheim, 2008.

176. Habasaki J.; Nagi, K.L. *J. Chem. Phys.* **2008**, *129*, 194501.

177. Sha, M.; Zhang, F.; Wu, G.; Fang, H.; Wang, C.; Chen, S.; Zhang, Y., Hu, J. *J. Chem. Phys.* **2008**, *128*, 134504.

178. Iwahashi, T.; Nishi, T.; Yamane, H.; Miyamae, T.; Kanai, K.; Seki, K.; Kim, D.; Ouchi, Y. *J.Phys. Chem. C*, **2009**, *113*, 19237.

179. Atkin, R; Warr, G.G. *J.Phys.Chem C* **2007**, *111*, 5162.

180. Kislenko, S.A.; Samoylov, I.S.; Amirov, R.H. *Phys. Chem. Chem. Phys*. **2009**, *11*, 5584.

181. Wang .S.; Li, S.; Cao, Z.; Yan, T. *J.Phys.Chem C* **2010**, *114*, 990.

182. Sha M.; Wu, G.; Fang, H.; Zhu, G.; Liu, Y. *J. Phys. Chem C* **2008**, *112*, 18584.

183. Heggen, B.; Zhao, W.; Leroy, F.; Dammers, A.; Muller-Plathe, F.; *J.Phys. Chem. B*, **2010**, *114*, 6954.

184. Valencia H.; Kohyama, M.; Tanaka, S.; Matsumoto, H. *J. Chem. Phys*. **2009**, *131*, 244705.

185. Mezger J.; Schramm, S.; Schroder, H.; Reichert, H.; Deutsch, M.; De Souza, E.J.; Okasinski, J.S.; Ocko, B.J.; Honkimaki, V.; Dosch, H. *Chem. Phys*., **2009**, *131*, 094701.

186. Ueno, K.; Kasuys, M.; Watarabe, M.; Mizukumi, M.; Kurihara, K. *Phys. Chem. Chem. Phys*. **2010**, *12*, 4066.

187. Santos, C.S.; Baldelli, S. *Chem. Soc. Rev.* **2010**, *39*, 2136.

188. Martinez, I.S.; Baldelli, S. *J.Phys.Chem. C* **2010**, *114*, 11564.

189. Pinilla, C.; del Popolo, M.G.; Lynden-Bell, R.M.; Kohanoff, J. *J.Phys.Chem. B* **2005**, *109*, 17922.

190. Perkin, S.; Albrecht, T.; Klein, J.; *Phys. Chem. Chem. Phys*. **2010**, *12*, 1243.

191. Dou, Q.; Sha, M.; Fu, H.; Wu, G. *ChemPhysChem* **2010**, *113*, 7049.

192. Hayes, R.,; El Abedin, A.Z.; Atkin, R. *J. Phys. Chem B* **2009**, *113*, 7049.

193. Steinruck, H.P. *Surf. Sc.* **2010**, *604*, 481.

194. Liu, Y.; Zhang, Y.I.; Wu, G.; Hu, J. *J. Am. Chem.Soc.* **2006**, *128*, 7456.

195. Chen, S.; Wu, G.; Sha, M.; Huang, S. *J. Am. Chem.Soc*. **2007**, *129*, 2416.

196. Le, M.L.P.; Alloin, F.; Strobel, P.; Lepretre, J-C.; Valle, C.P.D.; Judeinstein, P. *J. Phys.Chem.B* **2010**, *114*, 894.

197. Shah J.; Maginn, E.J. *Fluid Phase Equilbria*, **2004**, *222-223*, 195.

198. Keblinski, P.; Eggebrecht, J.; Wolf, D.; Phillpot, S.R. *J.Chem. Phys*. **2000**, *113*, 282.

199. Chen, T.; Berend, S.; Bell, A.T. *J.Chem. Phys*. **2009**, *131*, 246101.

200. Shim, Y.; Kim, H.J. *J.Phys.Chem.B* **2008**, *112*, 11028.

201. Hunt, P.A.; Maginn, E.J.; Jynden-Bell, R.M.; del Popolo, M.G. in *Ionic Liquids in Synthesis*; 2nd Ed. Wasserscheid, P., Welton, T., (Eds.) Ch 4, 206, Wiley-VCH, Weinheim, Germany, 2008.

202. Li, H.; Kobrak, M.N. *J. Chem. Phys.* **2009**, *131*, 194507.

203. Prado, C.E.R.; Freitas, L.C.G. *J. Mol. Str.-THEOCHEM*, **2007**, *847*, 93.

204. Lopes, J.N.C.; Deschamps, J.; Pa´dua, A. A. H., *J. Phys. Chem. B* **2004**, *108*, 2038.

205. Koddermann, T.; Paschek, T.; Ludwig, R. *ChemPhysChem*, **2007**, *8*, 2464.

206. Yan, T.; Wang, Y.; Knox, C. J.*Phys. Chem. B*, **2010**, *114*, 6905.

207. Materials Studio software, Accelrys, San Diego, http://accelrys.com/products/materials-studio/, May 2011.

208. Cerius2 software, Accelrys, San Diego, http://lms.chem.tamu.edu/cerius2.html, May 2011.

209. Andzelm, J.; Piela, L. J. *Phys.C: Solid State Phys*. **1977**, *10*, 2269.

210. Gao, G.; Cagin, T.; Goddard III, W.A. *Phys. Rev. Lett*. **1998**, *80*, 5556.

211. National Institute of Statndards and Technology, Thermophysical Properties of Fluid Systems, http://webbook.nist.gov/chemistry/fluid/, May 2011.

212. Garberoglio, G. *Langmuir*, **2007**, *23*, 12154.

213. Han, S. S.; Mendoza-Cortes, J. L.; Goddard III, W.A. *Chem. Soc. Rev.* **2009**, *3*, 1460.

214. Gaussian09 software, Gaussian Inc., http:*//*www.gaussian.com, May 2011.

215. LAMMPS software, SANDIA National lab., http:*//*lammps.sandia.gov, May 2011.

216. Andrade, J.D.; Bo1es, E.S.; Stassen, H., *J. Phys. Chem. B* **2002**, *106*, 13344.

217. Matlab software, Simulink, http://www.mathworks.com/products/matlab/, May 2011.

218. Yang, R.T. *Carbon*, **2000**, *38*, 623.

219. Sircar, S.; Cao, D.V. *Chem. Eng. Technol.* 2002, *25*, 945.

220. Zhang, X.; Cao, D.; Chen, J. *J. Phys. Chem. B* **2003**,*107*, 4942.

221. Benard, P.; Cahine, R. *Int. J. Hydrogen Energy* **2001**, *26*, 849.

222. Simonyan, V.V.; Diep, P.; Johnson, J.K. *J. Chem. Phys.* **1999**, *111*, 9778.

223. Zhao, Y.; Kim, Y-H.; Simpson L. J.; Dillon A.C.; Wei, S-H.; Heben M.J. *Phys. Rev. B.* **2008**, *78*, 144102.

224. Sun, Q.; Jena, P.; Wang, Q.; Marquez, M. *J. Am. Chem.Soc.*, **2006**, *128*, 9741.

225. Ohzuku, T.; Iwakoshi, Y.; Sawai, K. *J. Electrochem. Soc.* **1993**, *140*, 2490.

226. Kumar, A. *J. Soln. Chem.* **2008**, *37*, 203.

227. Gu, Z.; Brennecke, J.F. *J. Chem. Eng. Data*, **2002**, *47*, 339.

228. Tokuda, H.; Hayamizu, K.; Ishii, K.; Susan, M.A.B.H.; Watanabe, M. *J.Phys.Chem.B* **2004**, *108*, 16593.

229. Margulis, C.J.; Stern, H.A.; Berne, B.J. *J. Phys.Chem. B* **2002**, *106*, 12017.

230. Schroder, C.; Wakai, C.; Weingartner, H.; Steinhauser, O. *J.Chem Phys.* **2007**, *126*, 084511.

231. Schröder, C.; Rudas, T.; Steinhauser, O. *J. Chem. Phys*. **2006**, *125*, 244506.

232. Hunger, J.; Stoppa, A.; Buchner, R.; Hafter, G. *J.Phys.Chem.B*, **2009**, *113*, 9527.

233. Yamamoto, K.; Tani, M.; Hangyo, M. *J.Phys.Chem.B*, **2007**, *111*, 4854.

234. Marti, J.; Nagy, G.; Guardia, E.; Gordillo, M.C.; *J. Phys.Chem.B*. **2006**, *110*, 23987.

235. Castiglione, F.; Ragg, E.; Mele, A.; Appetecchi, G.B.; Montanino, M.; Passerini, S. *J.Phys.Chem. Lett.* **2011**, *2*, 153.

236. Borodin, O.; Smith, G.D.; Henderson, W.; *J. Phys. Chem, B* **2006**, *110*, 16879.

237. Fromling, T.; Kunze, M.; Schonhoff, M.; Sundermeyer, J.; Roling, B. *J. Phys. Chem, B* **2006**, *112*, 12985.

VITA

Name:	Mousumi Mani Biswas
Address:	412 ENPO Building, TAMU 3003, Texas A&M University, College Station, TX 77843-3112
Email Address:	mousumi.mani@gmail.com
Education:	B.Tech.(Hons.), Indian Institute of Technology, Kharagpur, 1995. M.S., University of Windsor, Windsor, Canada, 2004. Ph.D., Texas A&M University, 2011.